Touch at a Distance: Underwater Object Identification Using Pressure Sensors

by

Audrey Maertens

Ingénieure de l'Ecole Polytechnique (2009)

Submitted to the Department of Mechanical Engineering in partial fulfillment of the requirements for the degree of

Master of Science in Mechanical Engineering

at the

MASSACHUSETTS INSTITUTE OF TECHNOLOGY

June 2011

Author .....
Department of Mechanical Engineering
May 6, 2011

Certified by .....
Michael S Triantafyllou
Professor of Mechanical and Ocean Engineering
Thesis Supervisor

Accepted by .....
David Hardt, Professor of Mechanical Engineering
Chairman, Department Committee on Graduate Theses

Touch at a Distance: Underwater Object Identification Using Pressure Sensors

by

Audrey Maertens

Submitted to the Department of Mechanical Engineering
on May 6, 2011, in partial fulfillment of the
requirements for the degree of
Master of Science in Mechanical Engineering

Abstract

While the vast majority of underwater vehicles rely exclusively on sonar and vision to detect obstacles and maneuver, live fish also use their lateral line organ. The role played by the canal lateral line system is particularly important for hypogean fish, such as blind Mexican cave fish, who use it to avoid obstacles and navigate dexterously in complex environments. Similarly, pressure sensors could be used on underwater vehicles to expand their range of operability by filling the gap left by sonar and vision systems in turbid cluttered environments.

To understand how much information can be extracted from the artificial lateral line of an underwater vehicle exploring an unknown environment, the case of a foil passing a static object in still water is analyzed. A two-dimensional potential flow approach based on a source panels method is used to characterize the spatio-temporal pressure signature of the object as sensed by the vehicle. Simulations are used to estimate the sensing range of an artificial lateral line and the appropriate density of pressure sensors.

To emulate the object-detection and shape-recognition capabilities of the lateral line, an adapted unscented Kalman filter is combined with the hydrodynamic model. The method developed is experimentally tested in a water tank, using a hydrofoil instrumented with pressure sensors passing a static cylinder. The results show that location and shape informations of an elliptical cylinder can be successfully inferred from experimental pressure measurements. Performance of the proposed method for object identification using pressure sensors are discussed and ways to improve it are suggested.

Thesis Supervisor: Michael S Triantafyllou
Title: Professor of Mechanical and Ocean Engineering

Acknowledgments

First of all, I would like to acknowledge my boyfriend and life partner, Fabien, for his support and for dutifully proofreading this thesis.

I would like to acknowledge my advisor Prof. Michael Triantafyllou, as well as Jason Dahl for their support and insight on this project.

In addition, I wish to thank Jeff Dusek for letting me use his experimental setup and Vicente Fernandez who initiated this project. I would also like to acknowledge the Singapore-MIT Alliance for Research and Technology for funding this research.

Finally, I would like to acknowledge my colleagues and friends for their occasional help and everyday support: Heather Beem, Dave Rival, James Schulmeister, Stephanie Steele, Gabriel Weymouth.

Contents

List of Figures

List of Tables

Chapter 1

Introduction

1.1 Research motivation

The aim of this project is to allow underwater vehicles to use spatially distributed pressure sensors for mapping and navigation. Most underwater vehicles today rely exclusively on sonar and vision to detect obstacles and maneuver. However, both systems have limited capabilities and serious disadvantages, so the development of a new sensing capability might expand the range of operability of underwater vehicles.

The main limitation of vision is that light does not propagate well in water. Natural light does not penetrate further than 100 to 200 meters below the surface, and using vision at greater depths necessitates the use of powerful spotlights. However, if the water is murky, even a powerful spotlight will be helpless at lighting up the environment.

Sound usually propagates well in water, even though it can also suffer from scattering. However, sonars are very noisy: they strongly disturb the marine life ([30]) and are incompatible with any discretion requirement. Finally, sonars are not very effective in cluttered or confined environments due to excessive sound reflection.

Evolution endowed fish with a lateral line, a simple passive system that allows them to navigate dexterously, even in dark complex environments. Recent advancements in the area of microengineering will soon make it possible to build sensors that match the size and mimic the functions and organization of the lateral line. While

underwater spotlights and sonars consume a lot of energy and are typically expansive and cumbersome, artificial lateral lines could be a cheap alternative for a passive navigation system. However, the hydrodynamics involved needs to be better understood in order to provide an efficient navigation system. It is the goal of this research to gain insight into what the pressure distribution along a moving body can tell us about the environment.

How far away can an object be detected? How much information on its shape can be inferred from the measurements of an artificial lateral line? How should pressure sensors be distributed? Here are a few questions that are addressed in this thesis.

1.2 Biological inspiration: the lateral line

1.2.1 Morphology and physiology of the lateral line

The mechanosensory lateral line is a hydrodynamic receptor system that allows all fish and most amphibians to detect water motions around them. It is composed of a collection of small mechanoreceptive units called neuromasts. Each neuromast consists of a conglomeration of sensory hair cells associated with support cells that secrete a gelatinous mass, the cupula. When water flows past the cupula, friction causes it to move, which in turn deflects the cilia of the hair cells (Figure 1-1C). The deflection of the cilia is then transduced into trains of action potentials which are transmitted to the central nervous system for post-processing.

Fish possess hundreds to thousands of these neuromasts, located in various—but stereotypical—positions on the head and trunk ([34]), as illustrated in Figure 1-1A for a blind Mexican cave fish (*Astyanax mexicanus*). There is evidence that the lateral line is implicated in many behaviors such as schooling, courtship and spawning, prey detection, predator avoidance, rheotaxis, and spacial orientation ([8], [5]).

In most fish, there are two lateral line submodalities: superficial neuromasts, isolated on the surface of the skin and scales, and canal neuromasts embedded in subdermal water-filled canals (Figure 1-1). Experiments that selectively disable either

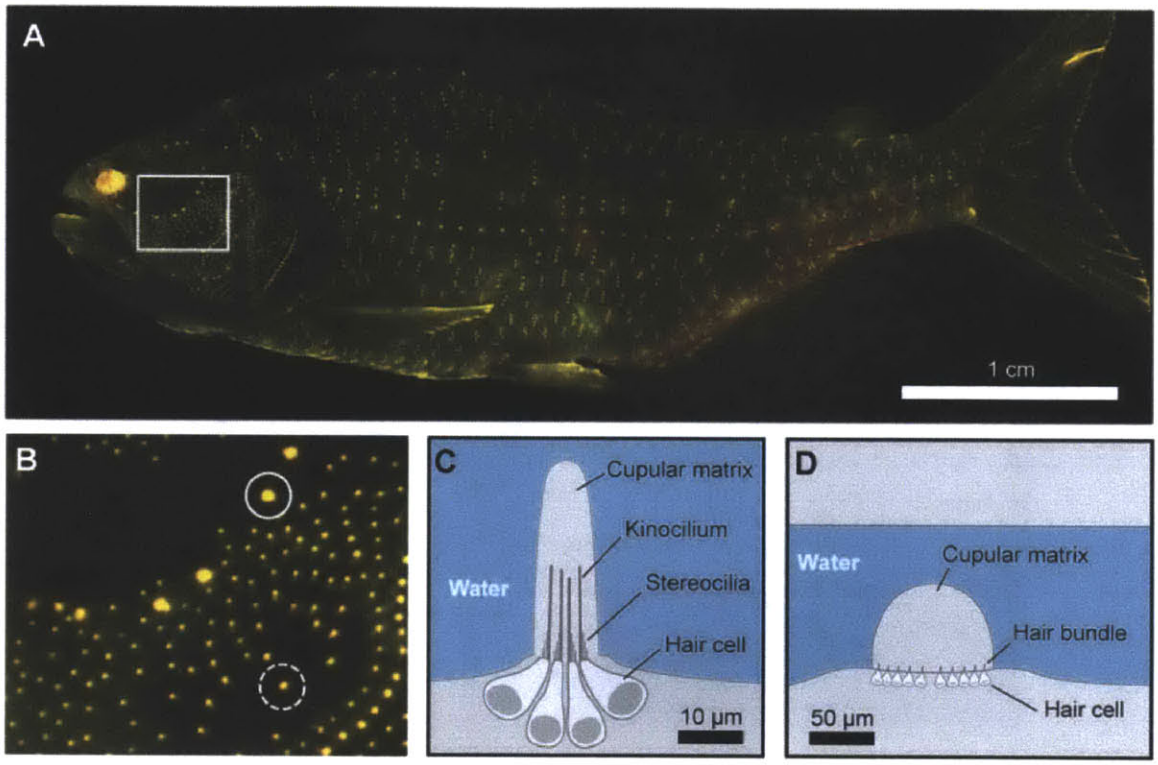

Figure 1-1: The structure of superficial and canal neuromasts. (A) Individual neuromasts appear as yellow points due to fluorescent staining [2-(4-(dimethylamino)styryl)-*N*-ethylpyridinium iodide] of the hair cells in the blind Mexican cave fish (*Astyanax mexicanus*). (B) A magnified view of a portion of the head highlights the different sizes of canal (solid circle) and superficial (dashed circle) neuromasts. (C) A schematic of a superficial neuromast illustrates its main anatomical features. (D) A schematic drawing of a canal neuromast. Adapted from [35].

superficial or canal neuromasts suggest that the two subsystems respond to different stimuli and play distinct roles in fish behavior ([27], [6], [21]). Superficial neuromasts respond to the flow of water along the skin of the fish; they provide an important source of information on currents in the environment of the fish and play a central role in behaviors like rheotaxis ([27]). However, superficial neuromasts do not respond to flow perturbations if the fish is exposed to running water ([11]).

The canals open to the environment at periodic intervals through pores, such that there is usually one neuromast between two pores (Figure 1-2A). As a result, the response of each canal neuromast to fluid motions inside the canal is proportional to the pressure difference between the two surrounding canal pores as illustrated in Figure 1-2B ([10], [7]). Unlike surface neuromasts, posterior canal neuromasts are

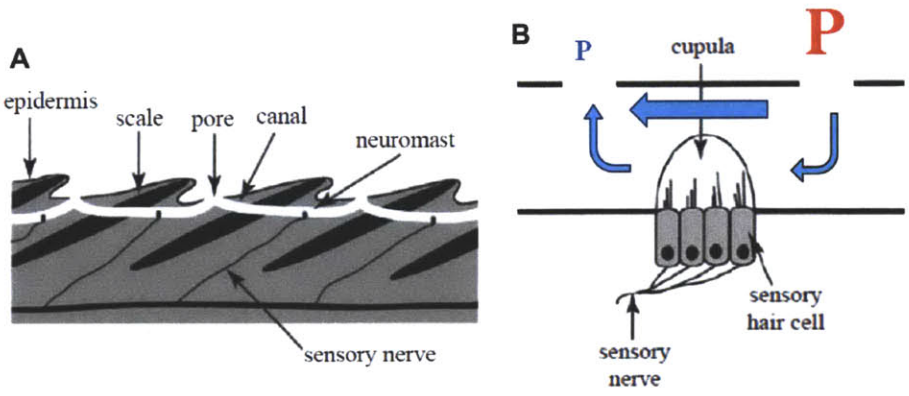

Figure 1-2: Schematics of a typical canal (A) and of the motion-sensing neuromast between a pair of pores inside a canal (B). Adapted from [1].

not stimulated by running water, which allows them to detect flow perturbations in any current condition ([11]). Experiments by Jansen [21] and Coombs [6] also showed that canal neuromasts respond to faster and smaller scale stimuli. Therefore, canal neuromasts are important to behaviors that require information about fine spatial details like prey localization and obstacle avoidance ([5]).

1.2.2 Importance of the lateral line for hypogean fish

The role played by the canal lateral line system is particularly important for hypogean fish (that spend their life in deep caves), such as blind Mexican cave fish ([28]). In the absence of light, hypogean fish cannot rely on vision to build up a 'picture' of their environment: they use hydrodynamic imaging instead. Most hypogean fish have a reduced visual system that they barely use, but an enhanced lateral line system. Canal neuromasts seem to play an essential role in replacing vision as the major sense by which blind cave fish perceive their surroundings. The flow-field that exists around a gliding fish is perturbed by objects in its immediate vicinity and these perturbations are detected by the lateral line system. In this way fish can build up a 'picture' of their environment, a process that has been called active 'hydrodynamic imaging' ([17]).

Behavioral experiments ([33], [9]) showed that blind Mexican cave fish are not only able to detect the presence of obstacles placed in their environment, but they are also capable of encoding both their shape and size. Von Campenhausen [33] also showed that fish trained to choose between doors of different shapes (horizontal and vertical rectangles) would glide in front of the doors before making their choice. These experiments confirm the hypothesis that the lateral line, and more specifically the canal subsystem, not only allows fish to navigate safely in unknown environments, but also to build up a three-dimensional 'image' of their surroundings.

Pressure sensing is a primary sense for hypogean fish and a promising complementary sensory capability for underwater vehicles. Using micro-electromechanical (MEMS) pressure sensors that would act like an artificial lateral line system has the potential to enable underwater vehicles to navigate even when vision and sonars cannot be used.

1.3 Previous work

1.3.1 Hydrodynamics of lateral line stimuli

The development of artificial lateral lines for underwater vehicles would enable imaging and navigation in environments where vision and acoustic sensing fail (such as murky cluttered environments) with much less energy and more discretion than sonar, since it is a passive system (as discussed in Section 1.1.1). But despite numerous articles published on the theme of fish lateral line system (see previous section), very few studies have aimed at reproducing the ability of imaging of blind Mexican cave fish into an artificial lateral line. So far, most of the work has been restricted to localizing a prey modeled by a dipole ([15], [29], [5]), which is of limited usefulness for underwater vehicles trying to navigate.

There are two essential aspects in object detection: the detection of objects themselves (mostly the effect on the flow of the no flux condition imposed at the object surface), and the detection of their wake (if they are moving relative to the flow).

Since vortices are characterized by a very distinctive low pressure, pressure sensors are very efficient at tracking vortices. Experiments by Chagnaud [3] showed that gold fish can detect a Karman vortex street and encode the vortex shedding frequency. Franosch [13] developed a mathematical model to determine how vortex rings in a Karman vortex street stimulate the canal lateral line of an axially symmetric body.

But objects in water do not only produce a wake, they also have their own hydrodynamic signature: they alter the flow surrounding them in way that depends on their size and shape. As stated earlier, the vast majority of studies on the question of object detection focused on the case of a vibrating or translating sphere ([29], [15]). Despite our knowing that fish can encode shape ([33], [9]), very little has been done to understand the hydrodynamics involved in shape encoding. The first study aiming at understanding the hydrodynamics of object identification was recently carried out by Sichert [32]. Sichert laid the foundations of hydrodynamics mapping using velocity sensing. In his model, the shape of a moving body of revolution is described by means of a multipole expansion and reconstructed—based on velocity readings by a

detecting body—using a maximum likelihood estimator. An important conclusion of this work is that at a distance smaller than the moving object size, the velocity field carries more information than its dipole simplification.

However, it has been shown experimentally that fish rely mainly on their canal subsystem ([6]) to detect and identify obstacles. Based on this observation, Bouffanais [2] investigated the forward and inverse problem of object detection and identification in outside flow using pressure sensing. He developed a parameterization that separately encodes size, location and shape of a plane object and concluded that the behavior of blind Mexican cave fish ([33])—'accelerate and glide past'—is probably the most efficient one. Fish first get an estimate of the size and location of the obstacle, and then gather finer information on its shape.

Both studies ([32] and [2]) simplified the problem enough to make it possible to use analytical models that help understanding the hydrodynamics involved. However, neither of them took into account the disturbances caused by the sensing object itself. In general, the pressure and velocity measured by the lateral line of a fish result from interactions between the outside flow, the fish and the unknown object. In the most extreme case—in the absence of outside flow—the only way for a fish to detect and identify stationary obstacles is to generated flow itself. In this case, the lateral line can be considered as an active sensing organ, and this is the behavior observed in fish that glide past objects in still water tanks ([33]). However, in the case of a cruising underwater vehicle trying to avoid obstacles, this active sensing does not require additional power input than what is necessary for cruising.

One of the only contributions to the understanding of the hydrodynamics involved in active object detection is a 25 year-old study from Hassan ([16]). He modeled the current around fish with a certain configuration of sources and sinks and used an iterative method to ensure that no water fluxes through the body. He observed that, when gliding past a circular cylinder, the spatio-temporal pressure signature along the fish is unique for each combination of radius and distance. In the case of a frontal approach, the results showed that the current velocity along the fish head increases noticeably, but not until the fish is at a relatively short distance from the obstacle.

Slightly more recently, he used a method developed by Geer ([14]) to describe the flow created by a slender body of revolution gliding toward or along a plane surface ([18], [19]). This method models the alteration of the flow due to the presence of a slender sensing body of revolution as a superposition of hydrodynamic poles continuously distributed along the axis of the body.

No study has yet aimed at studying the hydrodynamics involved in active object identification using the lateral line, and it is the goal of this thesis to lay the first foundations for such studies.

1.3.2 Bio-mimetic lateral lines

In parallel to the recent development of hydrodynamic methods aimed at understanding stimuli of the lateral line, there has been a growing interest in trying to manufacture artificial lateral lines. The development of both hydrodynamic tools and sensing devices is crucial to be able to mimic the capabilities of blind Mexican cave fish.

The main challenge in the design of artificial lateral lines is to fabricate sensors that are small enough not to interfere with the flow while being sensitive enough to detect flow structures. Fan [12] reported the first fabrication of an artificial lateral line. He designed hair cell sensors (with a 820 μm tall cilium) that respond to flow velocity in one direction. A few years later, Yang and Chen ([38], [4]) reported for the first time the use of an artificial lateral line (consisting of 500 μm high hot wire anemometers) to detect both a dipole and the wake of a cylinder. Inspired by the canal lateral line, they also proposed to package it as a canal to act like a high-pass filter and avoid the signal to be overcome by strong DC components. This first example of use of an artificial lateral line to detect flow structures is very promising and makes it more urgent to develop algorithms that will make it possible to use this emerging sensing technology for underwater vehicle applications. More recently, McConney [26] and Yang [39] reported designs of artificial lateral lines more closely inspired from the fish lateral line with bio-mimetic neuromasts. Yang [39] also developed a beamforming algorithm (inspired from traditional sonar techniques) to localize

dipoles in three-dimensional space and successfully used it with his bio-mimetic lateral line to localize both a vibrating sphere and a tail-flicking crayfish. However, as mentioned earlier, localizing vibrating spheres is of limited practical usefulness for underwater vehicles.

No successful implementation of micromechanical pressure sensors to mimic the the canal subsystem has yet been reported, but advancements in the area of micro-engineering that made the microfabrication of MEMS anemometers arrays possible are likely to make the fabrication of MEMS pressure sensors possible in the next few years.

1.4 Chapter preview

Chapter two introduces the problem studied in this thesis: a moving foil passing a static object in stationary two-dimensional inviscid flow. It also presents the numerical approach used to solve it.

Chapter three describes the pressure distribution along the foil when passing an object. Quantitative characterizations and guidelines for the use of pressure sensors to identify object shapes are given.

Chapter four details experiments performed to test the proposed method. The results of experimental object identification are also presented.

Chapter five discusses the performance of the object identification method proposed and several ways to improve it. The limits of the inviscid model are also discussed.

Chapter six draws conclusions on the research while recommendations for future work on the project are proposed in Chapter seven.

Chapter 2

Object identification: theory

2.1 Discussion of existing methods

The simplest way to characterize the hydrodynamic signal measured by a natural or artificial lateral line consists in modeling the problem in the context of two-dimensional potential flow models. Comparisons between viscous and inviscid simulations of a dipole near a fish [29] showed similar pressure gradients in both cases. They also showed important differences between the magnitude of the pressure gradient measured by a two-dimensional fish and a rotationally symmetrical one. However, a two-dimensional study is always a good source of information as a preliminary study before going for much more intensive three-dimensional simulations. We just need to keep in mind that the results from two-dimensional studies cannot directly be generalized to three-dimensional cases.

Algorithms have recently been proposed to identify the shape of objects underwater using velocity ([31]) or pressure ([2]) measurements. Both consider the case of a moving object detected by the lateral line of a body that does not affect the flow. The fact that the sensing body is considered as a 'ghost' might be a severe limitation, especially when the two objects are close (and they have to be close enough for the lateral line to sense information about the object shape). Interactions between the two bodies are precisely what makes active sensing possible. Since the goal here is to develop a model for active sensing, the possibility to extend either of these two

models to the case of several objects hydrodynamically interacting with each other will now be briefly discussed.

Conformal mapping ([2]) is a very efficient and elegant way to map the potential pressure field created by a moving object. It is also attractive because it gives a simple analytical expression of shapes. The conformal mapping study therefore provides a good way to characterize the shape of an object and understand the role of each parameter, especially the decreasing importance of shape parameters of increasing complexity. However, it requires situation of interest to be the conformal map of a configuration for which we know the analytical solution: there are very few of them. A two-dimensional object in free space can be transformed into a circle through a conformal map, and there is a known analytical solution for the pressure field around a circle. But no conformal map could allow us to transform a configuration with two objects into one for which a closed form solution is known. In conclusion, conformal mapping is great to give understanding on simple configurations, but it is not flexible enough to be adapted to more general cases.

The multipole expansion method ([31]) seems more flexible than the conformal mapping while still giving a good insight into the decreasing importance of the multipole of increasing order. However, the spherical expansion used in [31] requires a rotational symmetry that will usually be broken in the presence of two bodies. A multipole expansion could still be used for a two-dimensional approach, which would release the symmetry requirement. In this case, the velocity potential due to a stationary object in steady flow (of velocity $\vec{U}$) can be written as ([25])

$$\Phi(\vec{x}) = \vec{U} \cdot \vec{x} + \sum_{n \geq 1} (\vec{C_n} \cdot \vec{x})^{-n}. \tag{2.1}$$

This method has been tested in the simple case of a single object in a steady flow. The pressure is measured along a circle around the object and the multipole expansion is estimated using a standard least squares estimator. The shape is then estimated by following the streamline corresponding to the stagnation point. Typical results are shown in Figure 2-1. As can be seen from the top figures, the shape estimate can be

fairly accurate when the shape is not too different from that of a circle. However, the bottom figures show that when the aspect ratio becomes significant (on the order of 2:1) the multipole approximation of the shape is very poor. The conclusion of these tests is that the multiple expansion is good at approximating the far-field potential, but not at estimating the shape of the object that created it.

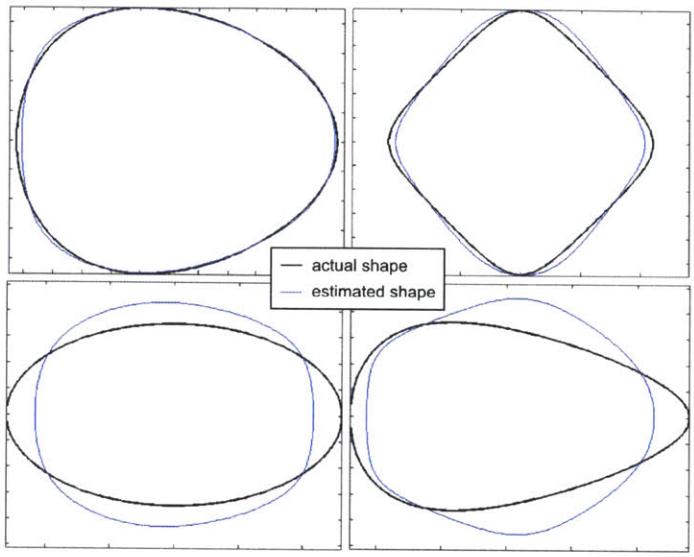

Figure 2-1: Examples of shape estimation using a multipole expansion

As a conclusion, both analytical methods lack the flexibility needed to be extended to more general problems like two objects hydrodynamically interacting. A flexible 'object based' (as opposed to 'far-field potential based') is needed. Since in potential flow theory objects affect the flow through the no-flux condition imposed along their surface, an intuitive way to represent them is a distributed flow source over their surface ([25]). Nonetheless, the conformal mapping method provides a convenient shape characterization that can be used in this new framework.

2.2 Shape characterization

It is believed that blind cave fish can separately encode the distance, size and shape of objects ([9]). Therefore, a convenient—and potentially biologically relevant—way to parameterize the problem is to characterize an object by two parameters accounting

for its position, one size parameter and several shape parameters. Another desirable feature of the parameterization is that the number of shape parameters needed to account for the pressure decreases with the distance to the object. Bouffanais [2] proposed such a characterization. Taking inspiration from his work, we can characterize objects by a parameterized curve:

$$\begin{aligned} S(\theta) &= a + R\left(e^{i\theta} + \sum_{k=1}^{\infty} \mu_k e^{-ik\theta}\right), \quad \theta \in [0, 2\pi], \\ &= x + iy + R\left(e^{i\theta} + \sum_{k=1}^{\infty} |\mu_k| e^{ik(\alpha_k - \theta)}\right), \quad \theta \in [0, 2\pi], \\ &= x + iy + R\left(e^{i\theta} + \sum_{k=1}^{\infty} (\mu_{kx} + i\mu_{ky}) e^{-ik\theta}\right), \quad \theta \in [0, 2\pi], \end{aligned} \tag{2.2}$$

where a ($a = x + iy$) refers to the location of the object 'center', R to its size and each μ_k ($\mu_k = |\mu_k| e^{ik\alpha_k} = \mu_{kx} + i\mu_{ky}$) term is associated with a $(k+1)$-gonal type of perturbation of the shape from that of a circle. As k increases, the impact of the μ_k term on the pressure field decays very quickly with distance from the cylinder ([2]).

For an ellipse of eccentricity e, only the first shape parameter μ_1 is non-zero: $|\mu_1| = \frac{1-\sqrt{1-e^2}}{1+\sqrt{1-e^2}}$ is a monotonous function of the eccentricity; $\alpha_1 = \arg(\mu_1)$ is twice the angle between the major axis and the horizontal axis; and R is the arithmetic mean of the minor and major radii of the ellipse. Equivalently, the shape defined by the parameterized curve $S(\theta) = a + R|\mu|^{i(\alpha-\theta)}$ is an ellipse of major radius $R(1 + |\mu|)$, minor radius $R(1-|\mu|)$ and eccentricity $\frac{2\sqrt{|\mu|}}{1+|\mu|}$. It will also be useful later to notice that the vertical radius of this ellipse (defined as the radius of the orthogonal projection of the ellipse on the imaginary axis) is $r_v = R|1 - \mu|$.

2.3 The forward problem: hydrodynamic modeling

The problem considered is the following: a moving 'fish-like' body ($S^{(1)}$) gliding at constant speed ($\vec{V}$) past a stationary object ($S^{(0)}$) in uniform flow (of velocity $\vec{U}$). Given the moving object, its trajectory, and the location (a), size (R) and shape (μ)

of the stationary object, as well as the outside uniform stream, the velocity potential anywhere in the flow field can be expressed in terms of a singularity distribution over the surface of the objects ([20]). The boundary-value problem considered is sketched in Figure 2-2.

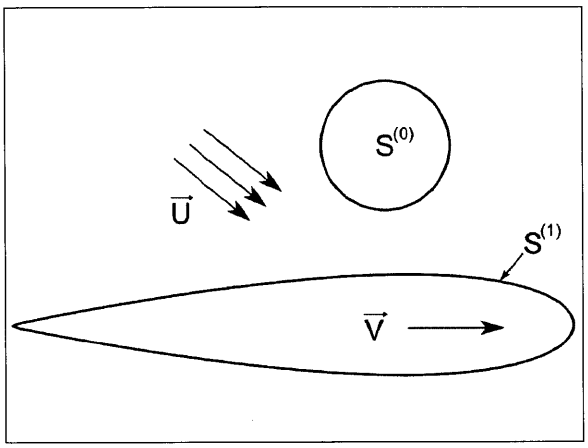

Figure 2-2: Boundary-value problem

The velocity potential Φ may be decomposed as follows:

$$\Phi(\vec{x}) = \vec{U} \cdot \vec{x} + \varphi(\vec{x}). \tag{2.3}$$

We are looking for the solutions of the following boundary-value problem:

$$\begin{array}{lrcrcl}
\text{In the fluid :} & \nabla^2\Phi & = & 0 & \longrightarrow & \nabla^2\varphi = 0, \\
\text{On } S^{(0)} : & \dfrac{\partial\Phi}{\partial n} & = & 0 & \longrightarrow & \dfrac{\partial\varphi}{\partial n} = -\vec{U}\cdot\vec{n}, \\
\text{On } S^{(1)} : & \dfrac{\partial\Phi}{\partial n} & = & \vec{V}\cdot\vec{n} & \longrightarrow & \dfrac{\partial\varphi}{\partial n} = (\vec{V}-\vec{U})\cdot\vec{n}, \\
\text{At infinity:} & \vec{\nabla}\Phi & = & \vec{U} & \longrightarrow & \varphi = 0.
\end{array} \tag{2.4}$$

The source formulation of the problem is:

$$\varphi(\vec{x}) = \int_S \delta(\vec{\xi}) G(\vec{x},\vec{\xi}) ds(\vec{\xi}), \tag{2.5}$$

where $S = S^{(0)} \cup^{(1)}$, δ is an unknown source distribution on the surface of the objects and $G(\vec{x},\vec{\xi}) = -\ln|\vec{x}-\vec{\xi}|$ is the two-dimensional Rankine source Green function.

From Eq. 2.5, we have:

$$\frac{\partial \varphi}{\partial n}(\vec{x}) = \int_S \delta(\vec{\xi}) \frac{\partial G}{\partial n}(\vec{x}, \vec{\xi}) ds(\vec{\xi}). \tag{2.6}$$

Substituting Eq. 2.4 into 2.6, we obtain:

$$\int_S \delta(\vec{\xi}) \frac{\partial G}{\partial n}(\vec{x}, \vec{\xi}) ds(\vec{\xi}) = \begin{cases} \vec{U} \cdot \vec{n} & \text{for } \vec{x} \in S^{(0)}, \\ (\vec{V} - \vec{U}) \cdot \vec{n} & \text{for } \vec{x} \in S^{(1)}. \end{cases} \tag{2.7}$$

The approach used to numerically solve Eq. 2.7 for $\delta(\vec{\xi})$ consists in:

1. breaking up the surface S into N straight line segments,

2. assuming the source strength is constant over each line segment (panel).

The relation in Eq. 2.7 can then be evaluated by breaking up the integral as the sum over all panels:

$$\sum_{j=1}^{N} \int_{S_j} \delta(\vec{\xi}) \frac{\partial G}{\partial n}(\vec{x}, \vec{\xi}) ds(\vec{\xi}) = \begin{cases} \vec{U} \cdot \vec{n} & \text{for } \vec{x} \in S^{(0)}, \\ (\vec{V} - \vec{U}) \cdot \vec{n} & \text{for } \vec{x} \in S^{(1)}. \end{cases} \tag{2.8}$$

For $\vec{x} = \vec{x_i}$ ($\vec{x_i}$ being the centroid position of the i–th panel) and δ_j the source strength of the j–th panel, Eq. 2.8 becomes:

$$\sum_{j=1}^{N} \delta_j \underbrace{\int_{S_j} \frac{\partial G}{\partial n}(\vec{x_i}, \vec{\xi}) ds(\vec{\xi})}_{A_{ij}} = \underbrace{\begin{cases} \vec{U} \cdot \vec{n_i} & \text{if } \vec{x_i} \in S^{(0)}, \\ (\vec{V} - \vec{U}) \cdot \vec{n_i} & \text{if } \vec{x_i} \in S^{(1)}. \end{cases}}_{b_i} \tag{2.9}$$

δ is obtained by solving the linear system $A\delta = b$. The velocity potential at any point $\vec{x}$ in the fluid can then be calculated by:

$$\varphi(\vec{x}) = \sum_{j=1}^{N} \delta_j \int_{S_j} G(\vec{x}, \vec{\xi}) ds(\vec{\xi}). \tag{2.10}$$

The velocity of the fluid can subsequently be computed using:

$$\vec{u} = \vec{\nabla}\Phi = \vec{U} + \sum_{j=1}^{N} \delta_j \int_{S_j} \vec{\nabla}_x G(\vec{x}, \vec{\xi}) ds(\vec{\xi}) \tag{2.11}$$

Finally, the unsteady Bernoulli equation gives us:

$$p(\vec{x}) = -\rho \left(\frac{\partial \Phi}{\partial t}(\vec{x}) + \frac{1}{2}|\vec{u}|^2 \right) + C. \tag{2.12}$$

When the pressure is calculated on the surface S_1, it is calculated as follows:

$$\begin{aligned} p(\vec{x}) &= -\rho \left(\frac{\mathrm{d}\Phi}{\mathrm{d}t}(\vec{x}) - \frac{\mathrm{d}\vec{x}}{\mathrm{d}t} \cdot \vec{\nabla}\Phi + \frac{1}{2}|\vec{u}|^2 \right) + C \\ &= -\rho \left(\frac{\mathrm{d}\Phi}{\mathrm{d}t}(\vec{x}) - \vec{V} \cdot \vec{u}(\vec{x}) + \frac{1}{2}|\vec{u}|^2 \right) + C. \end{aligned} \tag{2.13}$$

Since the pressure is calculated at the surface of the foil, it should always be estimated at the center of a panel. In order to get a sense of the number of panels needed to reasonably estimate the pressure measured along the foil, we consider the problem sketched in Figure 2-3A, where the red dot on the foil represents the point where the pressure is calculated. Each surface is broken up into segments of uniform size. Figure 2-3B, shows the calculated pressure at the red dot when breaking up the foil into 300 segments, and the circle into 10 to 200 segments. In Figure 2-3C, the circle is broken up into 50 segments and the foil into 50 to 500 segments. With only 20 segments for the circle and 100 for the foil, the error falls below 5%. We can therefore estimate that using 50 segments for the circle and 200 for the foil is a safe compromise

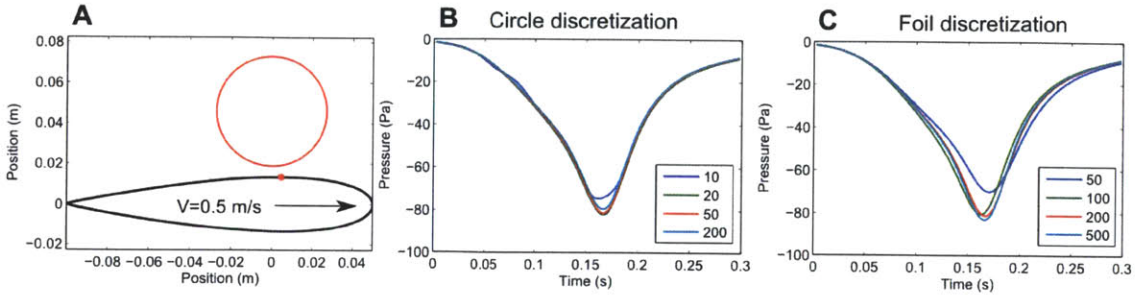

Figure 2-3: Surface discretization

between accuracy and calculation time.

The combination of the shape parameterization presented in Section 2.2 and the numerical potential flow model defines the forward methodology: relating pressure measurements to the variables of interest (location, size, and shape).

2.4 The inverse problem

2.4.1 Choice of the inversion algorithm

Combined with an inversion technique, the forward model can be used to solve the inverse problem: locating and identifying an object using pressure measurements. In experiments, the pressure measured is corrupted by noise. For proper inversion, the technique must be: 1) robust to noise, 2) capable of handling non-linearity, since the pressure does not depend linearly on the characterizing parameters of the stationary object and 3) dynamic, in order to be used in navigation of underwater vehicles.

A widely used class of algorithms to solve dynamical systems are Kalman filters. Parameters can be efficiently estimated on-line by writing a state-space representation:

$$\begin{cases} \mathbf{x}_{k+1} &= \mathbf{x}_k + \mathbf{r}_k \\ \mathbf{y}_k &= f\left(\mathbf{x}_k, \mathbf{u}_k\right) + \mathbf{e}_k \end{cases} \tag{2.14}$$

where $\mathbf{x}$ is the state vector (in our case, the shape we are trying to identify), $\mathbf{r}$ the process noise, $\mathbf{y}$ the observation (in our case, the pressure measured by the lateral line), $\mathbf{e}$ the measurement noise, $\mathbf{u}$ accounts for other parameters (location of the sensors, velocities) and f is the function that calculates the pressure at sensor locations given a set of objects.

When f is not linear (as in our case), the most common approach is to use an extended Kalman filter (EKF) which simply linearizes f so that the covariance and mean of the state can be recursively estimated using a traditional linear Kalman Filter. But the assumption that a linearized transformation of means and covariances is approximately equal to the true nonlinear transformation can be unsatisfactory for

highly nonlinear functions. And more important, the EKF requires the calculation of the Jacobian of f, for which no analytical expression is available here.

Therefore, the unscented Kalman filter (UKF) [23] is probably more suitable to solve this problem. Rather than approximating the function f, the UKF approximates the state probability density function by deterministic sampling. It is based on two fundamental principles. First, it is easier to perform a nonlinear transformation on individual samples than on a probability density function. Second, it is not too hard to find a set of individual points in state space whose sample probability density function (pdf) approximates the true pdf of a state vector. This set is found using the unscented transformation in which $2n+1$ sigma points (n is the state dimension, here the number of shape parameters) are chosen based on a square-root decomposition of the prior state covariance. These sigma points (here they are object shapes) are propagated through the true nonlinearity (the pressure function), without approximation, and a weighted mean and covariance is then calculated. This approach results in approximations that are accurate to the third order (Taylor series expansion) for Gaussian inputs for all nonlinearities. For non-Gaussian inputs, approximations are accurate to at least the second-order [23].

The UKF is therefore more accurate than the more traditional EKF for highly nonlinear problems. Moreover, it does not require the computation of derivatives for which no analytical expressions are available here. It also samples the state pdf with much less points than would be required by a Monte Carlo method, which makes it better suited for real time applications.

2.4.2 The unscented Kalman filter

The unscented transformation

As introduced above, the unscented transformation chooses a set of $2n+1$ (sigma) points so that their sample mean and covariance are $\bar{\mathbf{x}}$ and $\mathbf{P_{xx}}$. The nonlinear function is applied to each point in turn to yield a cloud of transformed points; $\bar{\mathbf{y}}$ and $\mathbf{P_{yy}}$ are the statistics of the transformed points. We form a matrix $\mathcal{X}$ of $2n+1$ sigma

vectors $\mathcal{X}_i$ according to the following:

$$\begin{aligned} \mathcal{X}_0 &= \bar{\mathbf{x}}, \\ \mathcal{X}_i &= \bar{\mathbf{x}} + \left(\sqrt{(n+\lambda)\,\mathbf{P_{xx}}}\right)_i, \quad i = 0, \ldots, n, \\ \mathcal{X}_{i+n} &= \bar{\mathbf{x}} - \left(\sqrt{(n+\lambda)\,\mathbf{P_{xx}}}\right)_i, \quad i = 0, \ldots, n, \end{aligned} \tag{2.15}$$

where $\lambda = \alpha^2 (n + \kappa) - n$ is a scaling parameter. The constant α determines the spread of the sigma points around $\bar{\mathbf{x}}$. It is usually set to a small positive value ($10^{-4} \leq \alpha \leq 1$) but the choice of the value will be discussed in the next section. The constant κ is a secondary scaling parameter, which is usually set to the heuristic value $3 - n$ ([24]). Finally, $\left(\sqrt{(n+\lambda)\,\mathbf{P_{xx}}}\right)_i$ is the i^{th} column of the lower-triangular Cholesky factorization of $(n + \lambda)\,\mathbf{P_{xx}}$.

The sigma vectors are propagated through the nonlinear pressure function:

$$\mathcal{Y}_i = f\left(\mathcal{X}_i, \mathbf{u}\right), \quad i = 0, \ldots, 2n. \tag{2.16}$$

The mean and covariance for $\mathbf{y}$ are approximated using a weighted sample mean and covariance of the transformed sigma points,

$$\bar{\mathbf{y}} \approx \sum_{i=0}^{2n} W_i^{(m)} \mathcal{Y}_i, \tag{2.17}$$

$$\mathbf{P_y} \approx \sum_{i=0}^{2n} W_i^{(c)} (\mathcal{Y}_i - \bar{\mathbf{y}})(\mathcal{Y}_i - \bar{\mathbf{y}})^T, \tag{2.18}$$

with weights given by

$$W_0^{(m)} = \frac{\lambda}{n+\lambda}, \quad W_0^{(c)} = \frac{\lambda}{n+\lambda} + 1 - \alpha^2 + \beta, \tag{2.19}$$

$$W_i^{(m)} = W_i^{(c)} = \frac{1}{2(n+\lambda)}, \quad i = 1, \ldots, 2n, \tag{2.20}$$

where β is a parameter used to incorporate prior knowledge of the distribution of $\mathbf{x}$ (for Gaussian distributions, $\beta = 2$ is optimal [23]).

Update equations

First, the shape and its covariance are initialized:

$$\hat{\mathbf{x}}_0 = E[\mathbf{x}], \tag{2.21}$$

$$\mathbf{P}_{\mathbf{x}_0} = E[(\mathbf{x} - \hat{\mathbf{x}}_0)(\mathbf{x} - \hat{\mathbf{x}}_0)^T]. \tag{2.22}$$

In the absence of prior information, we initialize the shape to a circle and the covariance to a diagonal matrix, as will be discussed in Section 4.3. Then, at each time step (each new pressure measurement), sigma vectors are calculated and the mean and covariance of the shape are updated.

For $k \geq 1$, the time update (a priori values) and sigma vectors are calculated as follows:

$$\hat{\mathbf{x}}_k^- = \hat{\mathbf{x}}_{k-1}, \tag{2.23}$$

$$\mathbf{P}_{\mathbf{x}_k}^- = \mathbf{P}_{\mathbf{x}_{k-1}} + \mathbf{R}_{k-1}^{\mathbf{r}}, \tag{2.24}$$

$$\mathcal{X}_{k|k-1} = [\ \hat{\mathbf{x}}_k^- \quad \hat{\mathbf{x}}_k^- + \sqrt{(n+\lambda)\mathbf{P}_{\mathbf{x}_k}^-} \quad \hat{\mathbf{x}}_k^- - \sqrt{(n+\lambda)\mathbf{P}_{\mathbf{x}_k}^-}\ ], \tag{2.25}$$

$$\mathcal{Y}_{k|k-1} = f(\mathcal{X}_{k|k-1}, \mathbf{u}_k), \tag{2.26}$$

$$\hat{\mathbf{y}}_k = \sum_{i=0}^{2n} W_i^{(m)} \mathcal{Y}_{i,k|k-1}. \tag{2.27}$$

And the measurement update equations (optimal gain and updated shape and covariance) are:

$$\mathbf{P}_{\mathbf{y}_k\mathbf{y}_k} = \sum_{i=0}^{2n} W_i^{(c)} (\mathcal{Y}_{i,k|k-1} - \bar{\mathbf{y}}_k)(\mathcal{Y}_{i,k|k-1} - \bar{\mathbf{y}}_k)^T + \mathbf{R}_k^{\mathbf{e}}, \tag{2.28}$$

$$\mathbf{P}_{\mathbf{x}_k\mathbf{y}_k} = \sum_{i=0}^{2n} W_i^{(c)} (\mathcal{X}_{i,k|k-1} - \bar{\mathbf{x}}_k)(\mathcal{Y}_{i,k|k-1} - \bar{\mathbf{y}}_k)^T, \tag{2.29}$$

$$\mathcal{G}_k = \mathbf{P}_{\mathbf{x}_k\mathbf{y}_k} \mathbf{P}_{\mathbf{y}_k\mathbf{y}_k}^{-1}, \tag{2.30}$$

$$\hat{\mathbf{x}}_k = \hat{\mathbf{x}}_k^- + \mathcal{G}_k(\mathbf{y}_k - \hat{\mathbf{y}}_k), \tag{2.31}$$

$$\mathbf{P}_{\mathbf{x}_k} = \mathbf{P}_{\mathbf{x}_k}^- - \mathcal{G}_k \mathbf{P}_{\mathbf{y}_k\mathbf{y}_k} \mathcal{G}_k^T, \tag{2.32}$$

where hats above letters stand for 'estimated value', $\mathbf{R^r}$ is the process-noise covariance and $\mathbf{R^e}$ is the measurement-noise covariance.

Adapted unscented Kalman filter

The UKF described above is usually used assuming all distributions are Gaussian. However, some configurations are not physical and cannot exist, this is the case of two rigid bodies intersecting each other. Using non-physical configurations as our sigma points can skew statistics and produce unusable results. One way to prevent this from happening, is to properly tune the value of the parameters of the UKF.

This problem is avoided in two steps. We first ensure that, at each time step, the a priori estimate of the object ($\hat{\mathbf{x}}_\mathbf{k}^-$) and the sensing body do not intersect. If needed, the Kalman gain of the previous time step is scaled down to ensure the non intersection.

Once the a priori configuration is valid, it is possible to find a radius r such that all the configurations in the ball of center $\hat{\mathbf{x}}_\mathbf{k}^-$ and radius r are valid. Therefore, the parameter α—that determines the spread of the samples around the mean in the unscented transform ([22])—can be chosen (for each time step) small enough that all the sigma points are valid. α is set to its default value ($\alpha = 0.9$) if it produces valid sigma points.

The UKF and the forward model can now be combined to solve the inverse problem: locating and identifying an object in the flow using pressure measurements.

Chapter 3

Theoretical pressure distribution on a foil passing an object

From now on, we will consider the case of a foil passing by an object. The foil considered in the rest of this thesis is a NACA 0018 foil (chord $c = 15$ cm, maximum thickness $T = 2.7$ cm). The position along the foil is measured as the arc length starting at the front, as shown in Figure 3-1. Only the pressure along the side of the foil that is closest to the object will be considered.

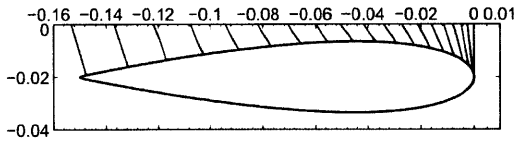

Figure 3-1: Position along the foil (m)

3.1 Comparison between different scenarios

The lateral line can be used both as a passive or active sensing modality. In the passive case, the fish relies on other bodies around it to interact with the flow and create measurable flow patterns. In the active case, the fish itself creates the flow that interacts with its environment. Flow perturbations due to the presence of objects are

measured by the lateral line and information about the environment is extracted. In general, both mechanisms are at play simultaneously. To understand the differences and interactions between the two mechanisms, three scenarios are considered: passive sensing, active sensing, and the combination of both. In all the simulations presented, the flow velocity (if non zero) is $U = 0.1$ m/s, the speed of the fish is $V = 0.5$ m/s. The object is a circular cylinder of radius $r = 0.5T = 1.35$ cm and the minimum distance between the foil and the object is $d = 0.25T = 6.75$ mm. The problem considered is sketched in Figure 3-2.

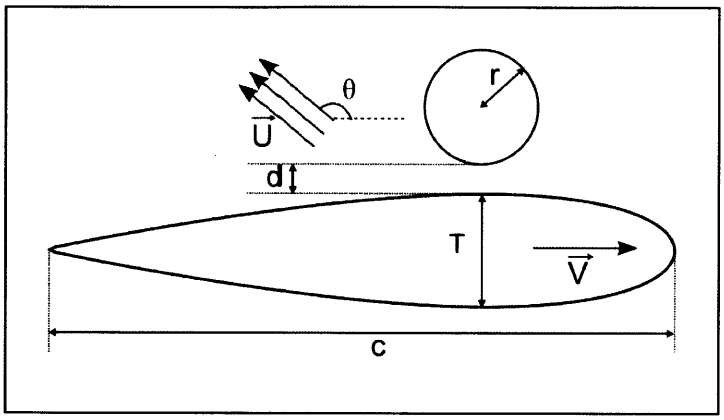

Figure 3-2: Sketch of the problem and variables

3.1.1 Passive sensing

This is the case that has mainly been investigated so far ([2], [32]). In this scenario, the foil measures pressure but is considered as a 'ghost' in that its effect on the flow is ignored. This case is considered as a benchmark for the other scenarios. The pressure along a 'ghost' foil as it passes the cylinder is plotted for three different angles of outside flow in Figure 3-3.

The vertical axis represents the position along the foil (as defined in Figure 3-1). The horizontal axis represents time as the foil passes the cylinder. The black dotted line shows the orthogonal projection of the cylinder center on the foil.

Here, the pressure field is the well known superposition of a free stream and a dipole. As the foil passes the cylinder, it simply measures this pressure field. In

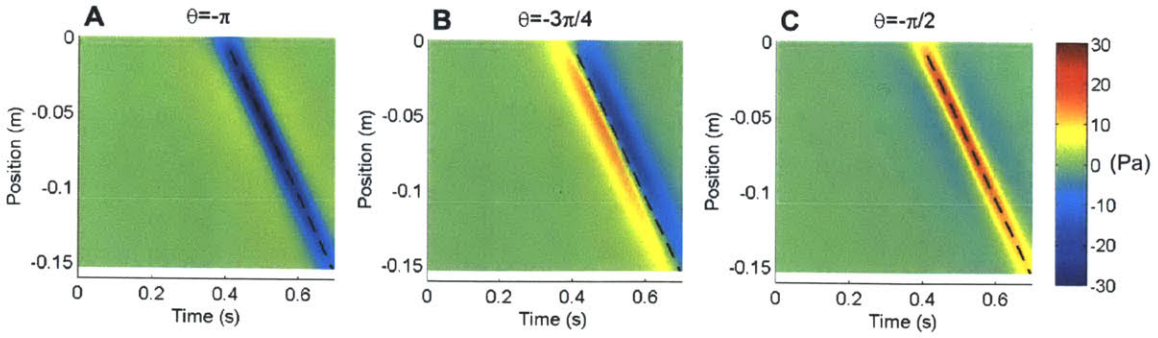

Figure 3-3: Passive pressure signature

the case considered, the foil measures a high or low pressure (depending on the flow angle) of magnitude 30 Pa. The pressure signal measured by the foil simply gets translated along the foil as it passes the cylinder. A horizontal or vertical slice of the plots in Figure 3-3 would be enough to summarize the information they contain. This means that measuring the pressure along the foil does not give significantly more information than measuring the pressure at one point in time or at one location on the foil.

3.1.2 Active sensing

In this case, the flow motion is generated by the foil. As can be seen in Figure 3-4A, the steady motion of the foil induces a high pressure at its front and a low pressure along its side, which makes it hard to distinguish the pressure pattern due to the presence of the object. Subtracting the steady state pressure reveals a pressure pattern (Figure 3-4B) very different from the passive case one. This pattern is much more complicated than in the passive case, so it potentially bears more information. Unless explicitly mentioned, the pressure will always be plotted after subtraction of the steady pressure.

The spatio-temporal pressure signature is characterized by a pressure peak at the front followed by a drop along the thickest part of the foil. The last third of the foil is only very weakly affected by the presence of the object. Contrary to the passive sensing case, time and space give different information, and disposing of a dense enough array of MEMS pressure sensors would experimentally make it possible

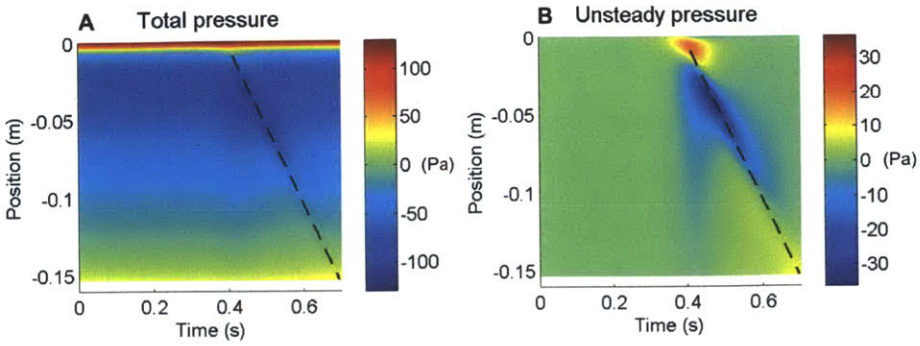

Figure 3-4: Active pressure signature

to take advantage of all the information. As the foil passes the object, the object experiences various flow velocities and directions, hence giving richer information than in the passive case. The spatio-temporal pressure characteristics will be investigated in the second part of this chapter. On the downside, the pressure signal amplitude is the same as in the passive case even though the speed of the foil is five times greater than what the flow speed was. This is due to the fact that the flow velocity at the the object decreases as the foil passes further away. For this reason, the pressure signal will also decrease faster with distance in this case than in the passive one.

3.1.3 Active sensing with external flow

Self-generated and outside flow can be combined in order to take advantage of the two scenarios described above. In this case, unlike in the passive case, the magnitude of the pressure signal strongly depends on the orientation of the outside flow compared to the motion of the foil. If the foil moves against the current (Figure 3-5A), the effective velocity of the foil is greater, and the effects of both flows add up to create a very strong pressure dip as the foil passes the object (of magnitude 200 Pa, as compared to 30 Pa with the outside flow or self-generated flow alone). In the case when the foil moves perpendicular to the outside current (Figure 3-5C), the pressure signal much weaker, except at the very front of the foil as it approaches the cylinder. An oblique current (Figure 3-5B) leads to an intermediate effect.

The simultaneous presence of outside and self-generated flows potentially allows to take advantage of both. Due to the presence of the outside current, the flow velocity

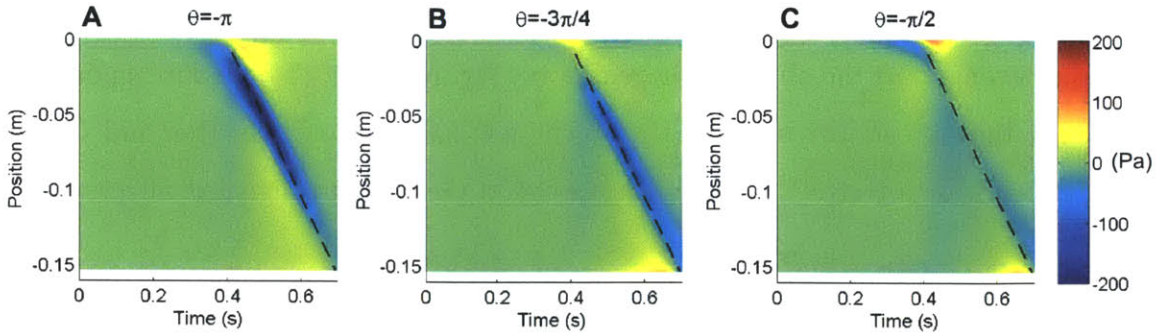

Figure 3-5: Combined pressure signature minus steady state

at the object does not drop as the foil gets further. Thanks to the self-generated flow, the pressure distribution changes with time if the foil passes close enough to it. Moreover, depending on the direction of the flow, both effects can add up to generate a very strong pressure signal. In this perspective, active sensing in the absence of external flow can be considered as a 'worst case scenario'. This is the case that we will investigate in the next section.

3.2 Characterization of the pressure distribution on a foil passing a cylinder

This section investigates the pressure distribution on a foil passing objects of various sizes without external flow. Hassan [16] has already discussed the spatio-temporal pressure distribution on a foil passing circular cylinders of various sizes and distances, but the question has remained unaddressed since then. Here, we will first discuss variations in size and distance for a circular cylinder, and extend the discussion to ellipses and more complex shapes (like triangles).

3.2.1 Variation in size and distance of a circular obstacle

Figure 3-6 shows the pressure signature of circular cylinders of radius $0.3T$ and $0.5T$ and at distance $0.2T$ and $0.3T$. The general pattern of the spatio-temporal pressure distribution is the same as described earlier, but for different cylinders, it differs in

peak (and drop) amplitude and spread. For a larger object (Figure 3-6B), the pressure signal is stronger; as the object is moved away (Figure 3-6C), the pressure signal gets weaker but its spread increases. As the object gets simultaneously further and smaller (Figure 3-6C, by a factor 1.6), only the spread of the pressure signal is affected.

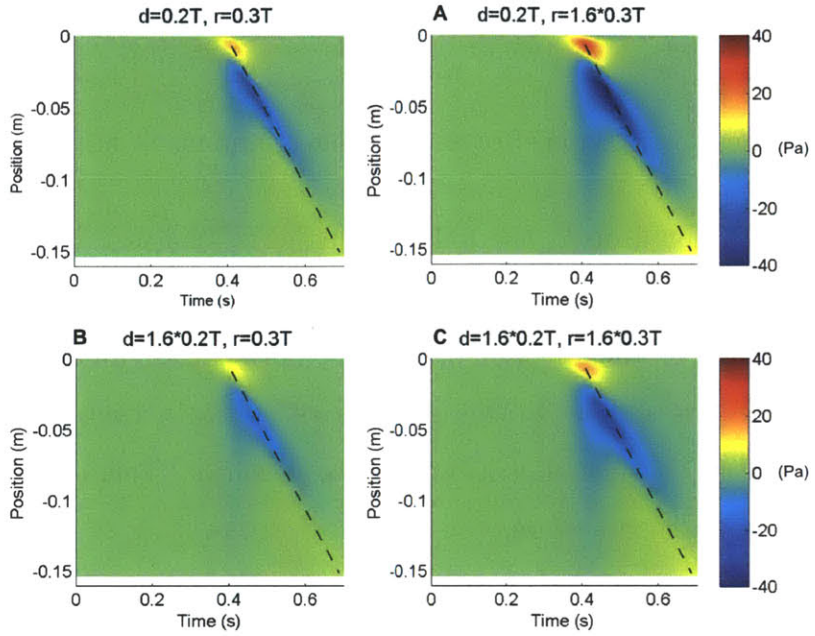

Figure 3-6: Pressure signature: variation in size and distance

These observations are confirmed by Figure 3-7 where the pressure signature of the reference cylinder ($r = 0.2T$, $d = 0.3T$) has been subtracted to the other pressure signatures for easier comparison.

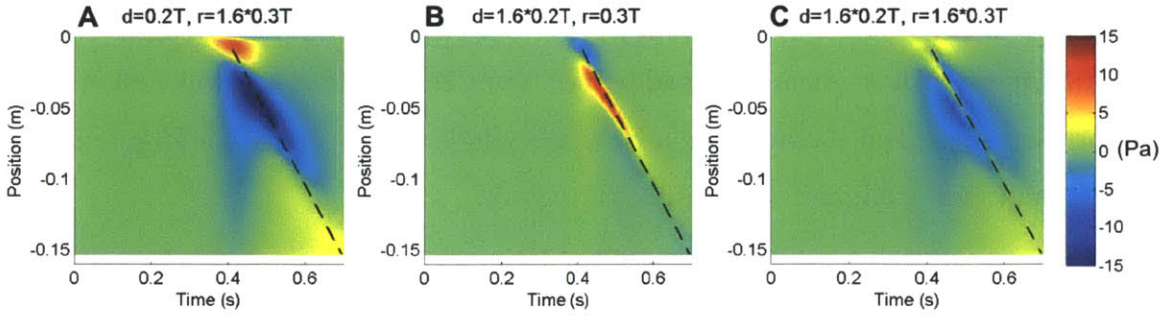

Figure 3-7: Pressure signature differences: variation in size and distance

Figure 3-8 shows pressure signals for more extreme cases: *A*) a very small and very close object; *B*) an object ten times bigger and further; and *C*) a very big object.

The figure shows that the general pattern of the spatio-temporal pressure distribution along the foil remains the same even in these more extreme configurations. The amplitude and spread of the pressure signal can vary by several orders of magnitude, but here again, the amplitude of the pressure drop seems to be conserved when r/d is constant.

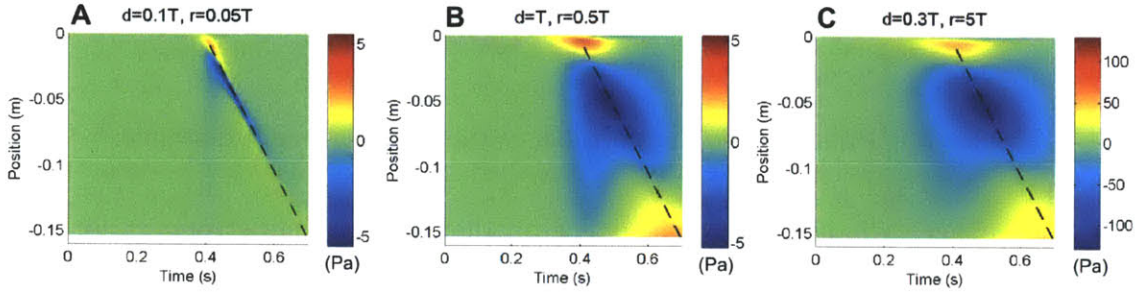

Figure 3-8: Active pressure signature in more extreme cases

The previous observations suggest that the amplitude and spread of the pressure signal are two relevant features to look at in order to determine the size and position of a circular cylinder based on its pressure signature. To generalize and quantify these observations, the amplitude of the pressure drop ($\max(-p)$) has been plotted in logarithmic scale (Figure 3-9A) as a function of distance (d) and radius (r) of the cylinder, for d ranging from $0.1T$ to $10T$ and r from $0.05T$ to $5T$. The pressure can locally be approximated by a linear regression in logarithmic space. To classify configurations in terms of distance and size of the object, Figure 3-9B shows linear regressions for the four quadrants delineated by $d = T$ and $r = 0.5T$. The equation of each plane is written in the corresponding quadrant.

It has been observed with Figures 3-6 and 3-7 that the pressure drop amplitude seems to be a function of the ratio r/d. The linear regression (Figure 3-9B) shows that for $0.1T < d < T$ and $0.05T < r < 0.5T$, it can indeed be approximated by a function of r/d: $\max(-p) \sim 10(r/d)^{1.5}$ Pa. However, this is not the case for all configurations:

- For bigger cylinders, the dependence on the size of the cylinder gets weaker: for $0.1T < d < T$ and $0.5T < r < 5T$, $\max(-p) \sim 10(r/T)^{0.2}(T/d)$ Pa.

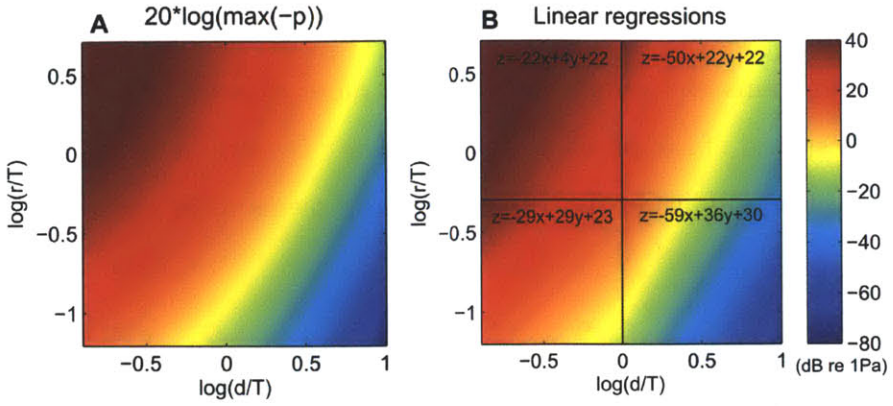

Figure 3-9: Pressure drop amplitude: variation in size and distance.

- For further cylinders, the dependence on the distance gets stronger: for $T < d < 10T$ and $0.05T < r < 0.5T$, $\max(-p) \sim 30(r/T)^2(T/d)^3$ Pa.

- For further and bigger cylinders, both effects are combined, such that for $T < d < 10T$ and $0.5T < r < 5T$, $\max(-p) \sim 10(r/T)(T/d)^{2.5}$ Pa.

It is interesting to notice that for small and close objects, the pressure amplitude only depends on the ratio r/d, while for larger and further objects, it is roughly proportional to the thickness of the foil. This is due to the fact that close to the object, the flow velocity is dictated by that of the foil, while further away it also depends on the amount of water displaced by the foil.

It has also been observed (Figure 3-6) that the pressure spread increases with the distance of the object, but only gets weakly affected by its size. The pressure spread is defined as the integral of the absolute value of the pressure over time and over the length of the foil, normalized by the amplitude of the pressure drop ($\tilde{S} = \int p/p_{min}\ \mathrm{d}l\ \mathrm{d}t$). Figure 3-10A shows how the pressure spread changes with object distance and size. Whereas the pressure drop amplitude decreases with distance and increases with size of the cylinder, the spread ($\tilde{S}$) increases with both distance and size. Figure 3-10B shows linear regressions for the same four quadrants as in Figure 3-9B.

- For small and far cylinders ($T < d < 10T$ and $0.05T < r < 0.5T$), the spread is almost independent on the distance: $\tilde{S} \sim 10^{-2}(r/T)^{0.6}$ m.s.

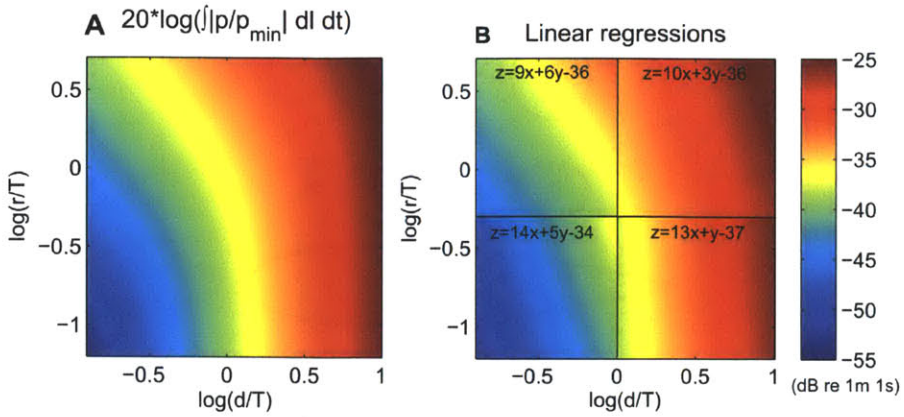

Figure 3-10: Pressure spread: variation in size and distance

- For bigger cylinders ($T < d < 10T$ and $0.5T < r < 5T$), the spread is slightly more sensitive to changes in distance: $\tilde{S} \sim 10^{-2}(r/T)^{0.5}(d/T)^{0.1}$ m.s.
- For closer cylinders ($0.1T < d < T$ and $0.05T < r < 0.5T$), the spread also is slightly more sensitive to changes in distance: $\tilde{S} \sim 10^{-2}(r/T)^{0.7}(d/T)^{0.2}$ m.s.
- For closer and bigger cylinders ($0.01T < d < 0.1T$ and $0.0T < r < 5T$), the spread is almost as sensitive to distance as to size: $\tilde{S} \sim 10^{-2}(r/T)^{0.5}(d/T)^{0.3}$ m.s.

3.2.2 Elliptical shapes

In this section we investigate (mainly qualitatively) how changes in aspect ratio and orientation of a cylinder affect the spatio-temporal pressure distribution on the foil. For a foil moving horizontally, we define the horizontal and vertical radii of an ellipse (respectively r_h and r_v) as shown in Figure 3-11. We define the radius (r) of an elliptical cylinder as its mean radius: $r = \frac{r_h + r_v}{2}$. To understand how changes in the three radii affect the pressure signature of the object, we compare in Figure 3-12 the pressure signature of a circular cylinder of radius $r = 0.5T$ to elliptical cylinders of eccentricity $e = 0.75$ with the same *A*) vertical radius; *B*) horizontal radius; and *C*) radius, as sketched in Figure 3-11.

In the four cases plotted here, the minimum distance between the cylinder (as defined in Figure 3-2) is $d = 0.32T$. The general pattern of the spatio-temporal pressure

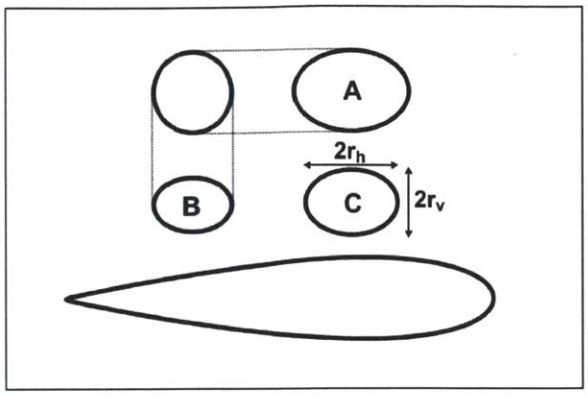

Figure 3-11: Cylinders used to investigate changes in horizontal and vertical radius

distribution is again the same for all cylinders, but slight differences in amplitude can be observed. The most noticeable trend is that a larger horizontal radius produces a much larger pressure signal.

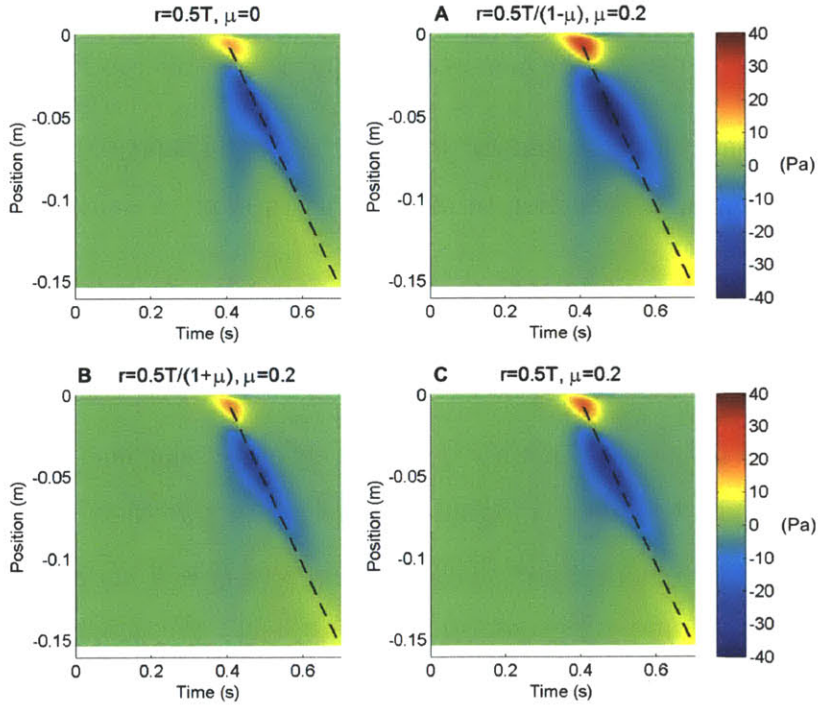

Figure 3-12: Pressure signature: variation in horizontal and vertical radii

More information can be extracted from the pressure difference between the elliptical cylinders and the circular cylinder (Figure 3-13). Figure 3-13A shows that the pressure peak and drop are both much stronger for a cylinder with a larger horizontal radius. However, unlike Figure 3-7A (where both horizontal and vertical radii are

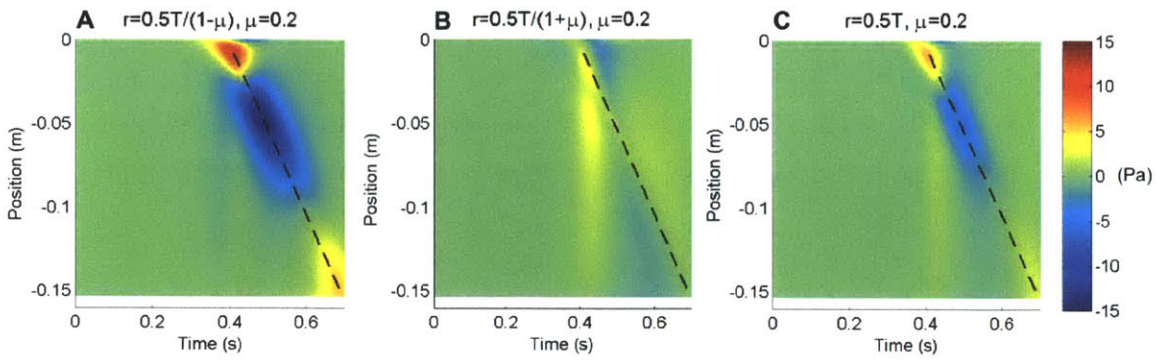

Figure 3-13: Pressure difference: variation in horizontal and vertical radii

larger), Figure 3-13A shows patterns slightly different from Figure 3-12: it is much more symmetric as regards to the dashed line. Figure 3-13B shows that changing the vertical radius has very little effect on the pressure signature of the cylinder. Figure 3-13C, that corresponds to an ellipse of intermediate size, exhibits an intermediate pattern.

To visualize the effect of cylinder orientation on the pressure, Figure 3-14 shows the pressure difference between a circular cylinder of radius $r = 0.5T$ at distance $d = 0.32T$ and ellipses of same radius (located at the same distance) oriented at different angles. It can be observed that the pressure signal is stronger for the horizontal ellipse (Figure 3-14A) and weaker for the vertical ellipse (Figure 3-14C), as explained in the previous paragraph. For an ellipse oriented at $\pi/4$ (Figure 3-14B), the pressure drops slightly earlier than for the cylinder due to the asymmetry of the configuration. It is also interesting to notice that the pressure differences (when compared to a same size circle) for ellipses of parameters μ and $-\mu$ are of opposite sign.

3.2.3 More general shape variations

Figure 3-15 shows the pressure difference between a circular cylinder of radius $r = 0.5T$ at distance $d = 0.32T$ and almost triangular (Figures 3-15A and 3-15B) and square shapes (Figures 3-15C and 3-15D). The corresponding shape is sketched in the bottom left corner of each plot. As shapes become more elaborate, the pressure signal also increases in complexity. However, the pressure difference (when compared

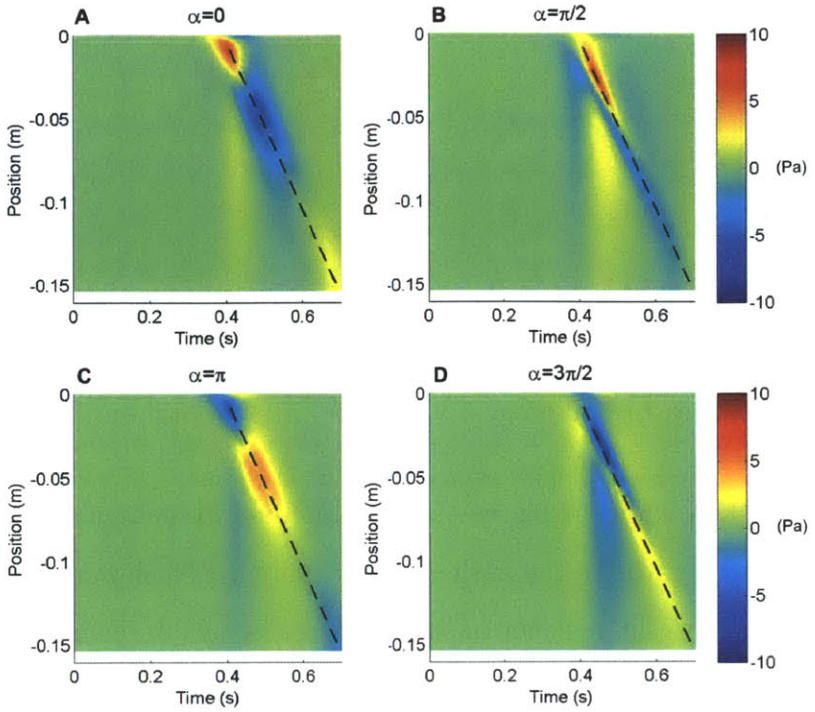

Figure 3-14: Pressure difference: variation in orientation, $r = 0.5T$ and $\mu = 0.2e^{i\alpha}$

to a same size circle) for shape parameters of opposite signs are still opposite.

It has been observed in Figure 3-13 that changing the horizontal diameter of an ellipse affects the pressure signature much more than changing its vertical diameter. This is intuitively due to the fact that changing the horizontal diameter strongly changes the shape of the ellipse close to the foil, whereas changing the vertical diameter mainly changes the shape of the ellipse further from the foil. Further from the foil, the effects of the no-flux condition are more diffuse, and the fluid velocity is smaller, so the pressure on the foil is primarily affected by the shape of the cylinder closest to it. To confirm this interpretation and somehow quantify it, we investigate the impact on the pressure signature of two transformations: cutting $1/4$ of an ellipse and changing its aspect ratio (Figure 3-16). Figure 3-16C shows three cylinder shapes. The reference cylinder (cylinder o) has parameters $r = 3.81$ cm $= 1.4T$ and $\mu = -0.2$. The foil passes at distance $d = 0.32T$ of all cylinders. Figure 3-16A is a plot of the spatio-temporal pressure difference between cylinders a and o, where a is the same cylinder as o, cut at $3/4$ of its height. There is only a 3 Pa difference, despite the fact that $1/4$ of the ellipse has been cut. Cylinder b shows how much (or how

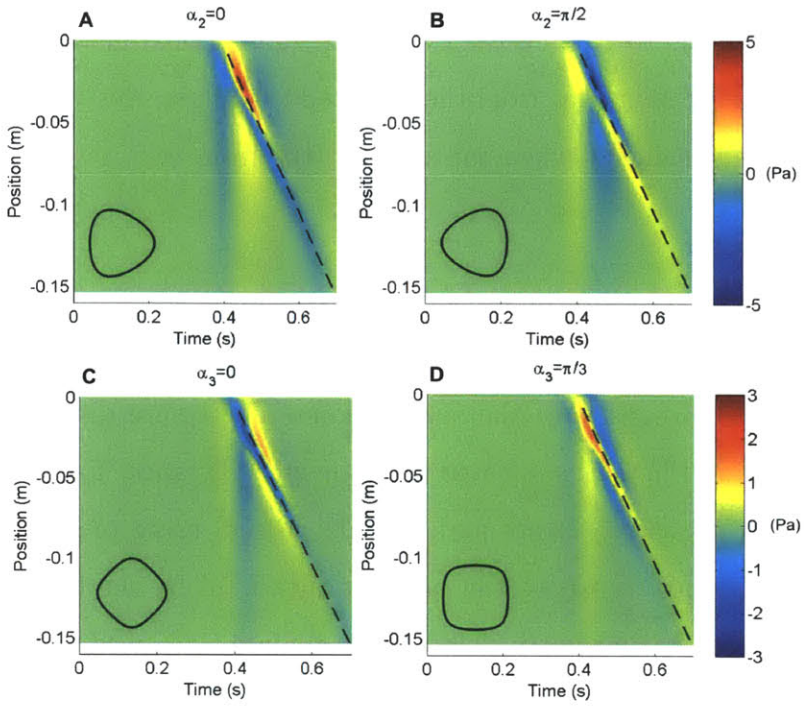

Figure 3-15: Pressure difference: triangle and square shapes. For A and B, $\mu_1 = 0$ and $\mu_2 = 0.1e^{2i\alpha_2}$. For C and D, $\mu_1 = \mu_2 = 0$ and $\mu_3 = 0.67e^{3i\alpha_3}$.

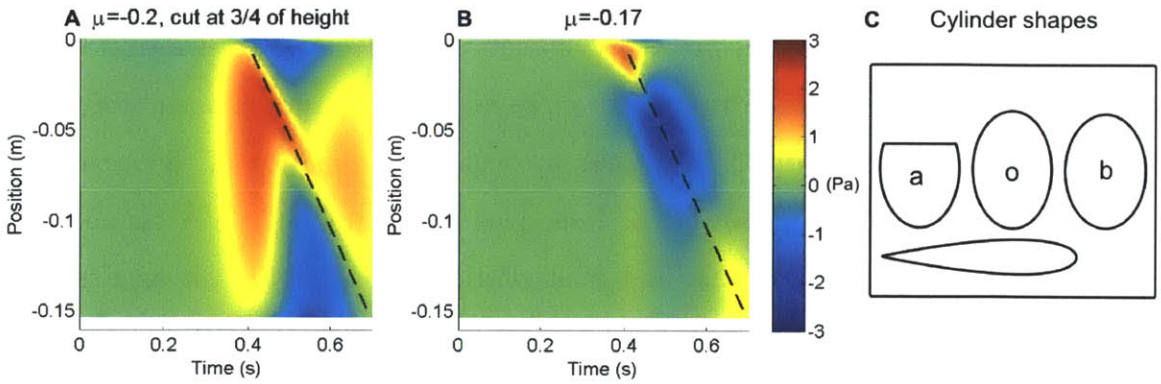

Figure 3-16: Pressure difference: comparison between cutting the top of an ellipse and changing its aspect ratio.

little) you need to alter the aspect ratio of ellipse o to get a pressure difference of the same magnitude (as plotted in Figure 3-16B): you do not need to alter it much. The pressure difference due to cutting the cylinder is more global because, as mentioned earlier, changes in the shape far from the foil produce diffuse pressure differences, but the amplitude is the same as when subtracting 0.03 from μ.

3.3 Sensitivity analysis

We now have a good picture of the spatio-temporal pressure distribution on a foil passing an object and how it is affected by changes in distance, size and shape of the object. Since our goal is to locate and identify objects using pressure sensors, it is of interest to know how sensitive the pressure measured by the foil is to variations of these parameters. A quantitative sensitivity analysis is carried out in this section. We define the pressure sensitivity in parameter x as $S_x = \max(|\mathrm{d}p/\mathrm{d}x|)$ because it is easy to relate to technical limitations. Plots of sensitivity defined as the integral over the length of the foil and over time of $|\mathrm{d}p/\mathrm{d}x|$ can also be found in Appendix A.

3.3.1 Variation in distance of a circular obstacle

Figure 3-17 shows the pressure sensitivity to distance ($\tilde{d} = d/T$) and how it depends on the distance and size of the cylinder. In accordance with intuition, the pressure is most sensitive to distance for close and big objects. A linear regression in logarithmic space (Figure 3-17B) gives a rough approximation of the sensitivity as $S_{\tilde{d}} \sim 10(r/T)(T/d)^3$. However, a closer look at Figure 3-17A reveals that the sensitivity decreases fastest for far and small objects. Sensitivity to distance is plotted as a function of distance in Figure 3-18 for $r = 0.05T$, $r = 0.5T$ and $r = 5T$. Linear regressions for $r = 0.5T$ are plotted for $d < T$ and $d > T$. It shows that a better approximation for the sensitivity is $S_{\tilde{d}} \sim 20(r/T)(T/d)^2$ for $d < T$ and $S_{\tilde{d}} \sim 40(r/T)(T/d)^4$ for $d > T$. This result indicates that sensitivity to distance decreases very quickly when objects get further than the foil thickness.

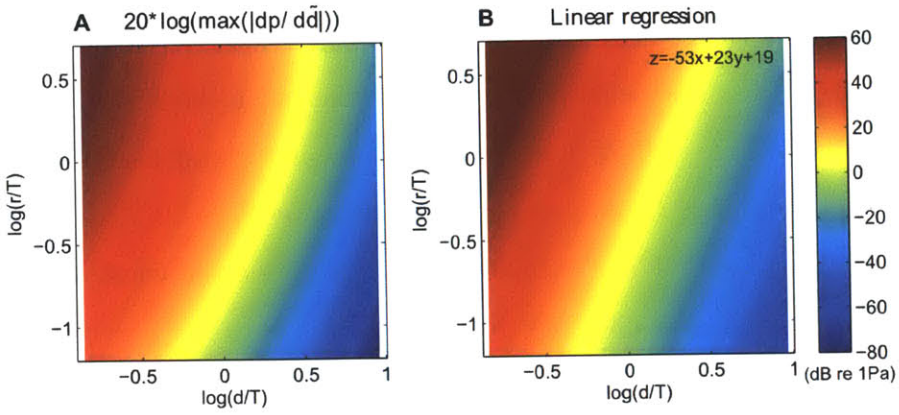

Figure 3-17: Sensitivity to distance

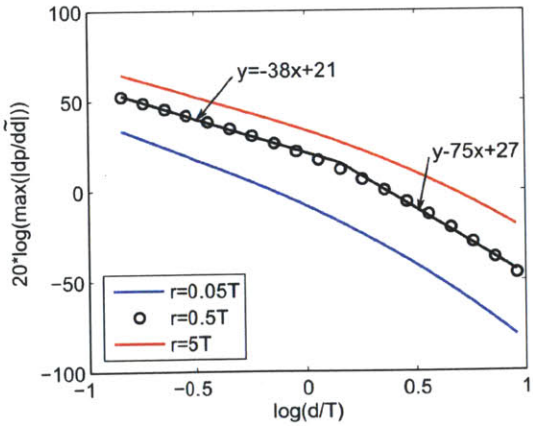

Figure 3-18: Sensitivity to distance for fixed sizes

3.3.2 Variation in size of a circular obstacle

Figure 3-19A shows the pressure sensitivity to size ($\tilde{r} = r/T$) and how it depends on the distance and size of the cylinder. The sensitivity decreases with distance but is not monotonic with size. For a given distance d, the sensitivity to size is maximum for $r/T = 0.6\sqrt{d/T}$. The sensitivity to size is plotted against distance in Figure 3-19B for $r = 0.05T$, $r = 0.5T$ and $r = 5T$. Linear regressions for $r = 0.5T$ are plotted for $d < T$ and $d > T$ and give the approximation $S_{\tilde{r}} \sim 20(T/d)$ for $d < T$ and $S_{\tilde{r}} \sim 30(T/d)^3$ for $d > T$. For $r = 0.05T$, $S_{\tilde{r}} \sim 2(T/d)$ on the whole distance range considered. For $r = 5T$, $S_{\tilde{r}} \sim 3(T/d)^3$ for $d > 0.3T$.

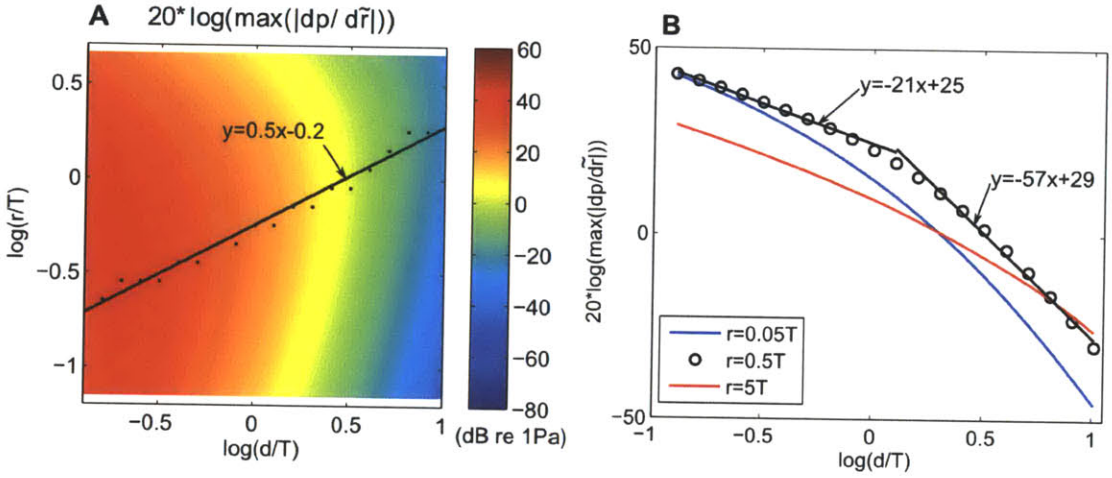

Figure 3-19: Sensitivity to size

3.3.3 Variation in eccentricity of an elliptical obstacle

Figure 3-20A shows the pressure sensitivity to eccentricity for a horizontal ellipse of radius $r = 0.5T$ and how it depends on the distance and eccentricity of the ellipse. The sensitivity in eccentricity is mostly independent of the eccentricity while it clearly decreases with distance. The sensitivity to eccentricity is plotted against distance in Figure 3-20B for $\mu = 0$ and $\mu = 0.5$. Linear regressions for $\mu = 0$ are plotted for $d < T$ and $d > T$. They give the approximation $S_\mu \sim 7(T/d)$ for $d < T$ and $S_\mu \sim 13(T/d)^3$ for $d > T$.

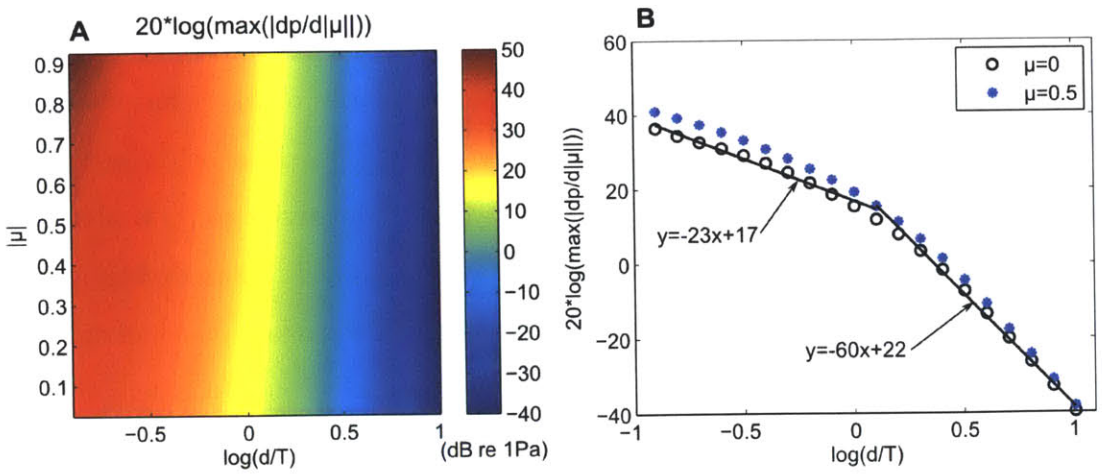

Figure 3-20: Sensitivity to eccentricity for a horizontal ellipse

3.3.4 Variation in orientation of an elliptical obstacle

Figure 3-21A shows the pressure sensitivity to orientation ($\tilde{\alpha} = \alpha/(2\pi)$) for an ellipse parameterized by $r = 0.5T$ and $|\mu| = 0.2$. For small distances, the sensitivity has a slight non monotonic dependence on α (it is highest for $\alpha = 1/3$ and $\alpha = 2/3$), while it clearly decreases with distance. The sensitivity to orientation is plotted as a function of distance in Figure 3-21B for $\alpha = 0.7\pi$ and $\alpha = \pi$. Linear regressions for $\alpha = \pi$ are plotted for $d < T$ and $d > T$. They give the approximation $S_\mu \sim 5(T/d)^{1.5}$ for $d < T$ and $S_\mu \sim 14(T/d)^3$ for $d > T$.

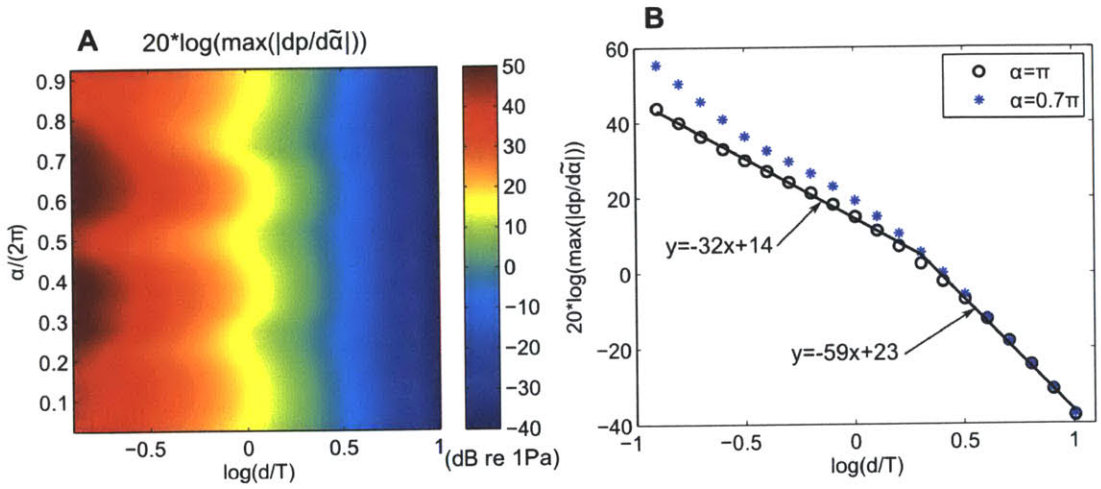

Figure 3-21: Sensitivity to orientation

3.3.5 More elaborate shape variations

Shapes, as defined in Eq. 2.2, are parameterized by a series of μ_k terms. Based on the pressure field generated by an object in steady flow ([2]), the sensitivity to μ_k is expected to decrease faster with distance for larger ks. Sensitivity to μ_k is plotted in Figure 3-22 for $k \in \{1,\ 2,\ 3\}$ for cylinders of radius $r = 0.5T$. Considering a circle as the reference shape, μ_1 corresponds to an elliptical deformation, μ_2 to a triangular deformation and μ_3 to a square deformation. Whereas for $d < T$ the sensitivity is almost the same for the three μ_ks, at $d = 10T$, $S_{\mu_1} \sim 6S_{\mu_2} \sim 30S_{\mu_3}$. For $d > T$, the sensitivity to highest order terms decreases fastest, which confirms our expectations.

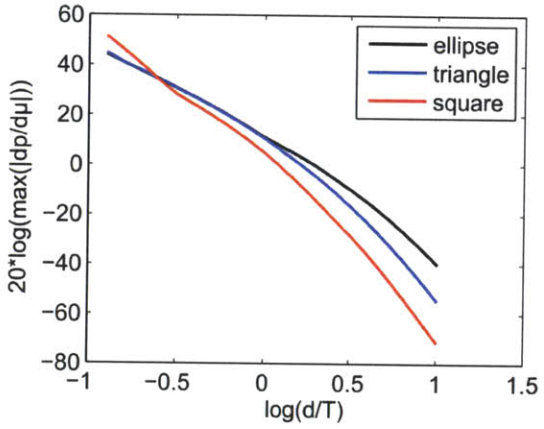

Figure 3-22: Sensitivity to shape

3.4 Guidelines for the use of pressure sensors for active object identification

3.4.1 Sensing range

In Section 3.3, we have characterized the maximum pressure measured by a foil passing an object as a function of the size and distance of the object. We have also identified the pressure sensitivity to changes with size, distance and shape of the object. We can now use these results to estimate the capabilities of a foil equipped with distributed

pressure sensors in terms of object detection and identification.

Depending on the pressure sensors characteristics and background noise, we can define Δp_0 as our pressure resolution. As defined earlier, $\tilde{r} = r/T$ and $\tilde{d} = d/T$ are the normalized radius and distance of the object.

We have observed in Section 3.2.1 that the pressure amplitude is about

$$\begin{cases} \max(-p) \sim 10 \left(\dfrac{\tilde{r}}{\tilde{d}}\right)^{3/2} \text{ Pa}, & \text{for } \tilde{d} < 1, \\ \max(-p) \sim 10 \dfrac{\tilde{r}}{\tilde{d}^{5/2}} \text{ Pa}, & \text{for } \tilde{d} > 1. \end{cases} \tag{3.1}$$

Using the fact that the pressure is proportional to the square of the foil velocity (V) (see Section 2.3), we see that the ability to detect an object by passing in front of it with a foil equipped with pressure sensors requires:

$$\begin{cases} \Delta p_0 < 40V^2 \left(\dfrac{\tilde{r}}{\tilde{d}}\right)^{3/2} \text{ Pa}, & \text{if } \tilde{d} < 1, \\ \Delta p_0 < 40V^2 \dfrac{\tilde{r}}{\tilde{d}^{5/2}} \text{ Pa}, & \text{if } \tilde{d} > 1. \end{cases} \tag{3.2}$$

Using our sensitivity analysis, the same reasoning can be applied to translate the pressure resolution into resolution in terms of size, position and shape of the cylinder. We know from Section 3.3.1 that a distance change $\Delta\tilde{d}$ causes pressure variations of order

$$\begin{cases} \Delta p \sim 80V^2 \Delta\tilde{d} \dfrac{\tilde{r}}{\tilde{d}^2} \text{ Pa}, & \text{if } \tilde{d} < 1, \\ \Delta p \sim 120V^2 \Delta\tilde{d} \dfrac{\tilde{r}}{\tilde{d}^4} \text{ Pa}, & \text{if } \tilde{d} > 1. \end{cases} \tag{3.3}$$

Therefore, the error in distance estimation $E_{\tilde{d}} = \Delta\tilde{d}/\tilde{d}$ based on pressure measurements will be on the order of

$$\begin{cases} E_{\tilde{d}} \sim \dfrac{\Delta p_0}{80V^2} \dfrac{\tilde{d}}{\tilde{r}} & \text{if } \tilde{d} < 1, \\ E_{\tilde{d}} \sim \dfrac{\Delta p_0}{120V^2} \dfrac{\tilde{d}^3}{\tilde{r}} & \text{if } \tilde{d} > 1. \end{cases} \tag{3.4}$$

We can similarly use the results from Section 3.3.2 to approximate the error in size estimation $E_{\tilde{r}} = \Delta\tilde{r}/\tilde{r}$ for an object of diameter comparable to the thickness of the foil. In general this will provide a lower bound of the error.

$$\begin{cases} E_{\tilde{r}} \sim \dfrac{\Delta p_0}{80V^2}\dfrac{\tilde{d}}{\tilde{r}} & \text{if } \tilde{d} < 1, \\ E_{\tilde{r}} \sim \dfrac{\Delta p_0}{120V^2}\dfrac{\tilde{d}^3}{\tilde{r}} & \text{if } \tilde{d} > 1. \end{cases} \tag{3.5}$$

Quantifying the shape estimate precision is more complicated as it depends on more parameters. For the sake of argument, we can use the result of Section 3.3.3 to estimate the conditions under which we will be able to distinguish a horizontal ellipse of shape parameter μ and radius $r = 0.5T$ from a circle:

$$\begin{cases} \Delta p_0 < 30V^2\dfrac{\mu}{\tilde{d}} \text{ Pa}, & \text{if } \tilde{d} < 1, \\ \Delta p_0 < 50V^2\dfrac{\mu}{\tilde{d}^3} \text{ Pa}, & \text{if } \tilde{d} > 1. \end{cases} \tag{3.6}$$

Let us now consider the canonical example that we have used so far: a foil moving at speed $V = 0.5$ m/s past a circular cylinder of radius $r = 0.5T$. We assume here that our pressure resolution is $\Delta p_0 = 5$ Pa. According to Eq. 3.2, we will be able to detect the presence of an object if its distance to the foil is less than $0.8T$. To have a 10% precision on our estimates of distance and size, we need to pass less than $0.2T$ away from it. Finally, if the object was an ellipse of parameters $r = 0.5T$ and $\mu = 0.1$, we would need to pass $0.1T$ away to tell that it is not a circle. It is also interesting to notice that, although when the object is far the pressure is more sensitive to elliptical shapes than to triangular or square shapes, at the distance at which you would be able to identify an ellipse, the pressure is as sensitive to triangular and square deformations as to elliptical deformations. However, in terms of shape estimation, trying to identify too many parameters might worsen the overall estimate.

3.4.2 Sensor density

The above discussion is purely based on variations in pressure due to the presence of objects in the flow. However, the quality of the estimate will also depend on the spatial density of sensors and sampling rate, as well as on the inference algorithm used.

It has been observed that in the active object identification scheme, the pressure signal is not simply translated in time, but each point along the foil measures a different pressure trace. Therefore, high sampling frequency and high spatial density are not equivalent. The signal is characterized by a pressure peak at the front followed by a pressure drop along the first two thirds of the body, whereas the pressure along the last third of the foil is only weakly affected by the presence of a nearby object. This observation indicates that, to actively identify objects, pressure sensors should be distributed along the first two thirds of the foil.

We have observed in Section 3.2.1 that the size and distance of an object can be identified by looking at the pressure spread and amplitude. However, the pressure signal needs to be looked at in more details to be able to identify the shape of an object. The typical magnitude of the pressure gradient, for the case considered, is 1 kPa.m^{-1} (see Figure 3-23). If we consider that 5 Pa is the smallest pressure difference that can be resolved, then a spacing of 5 mm gives a virtually infinite resolution.

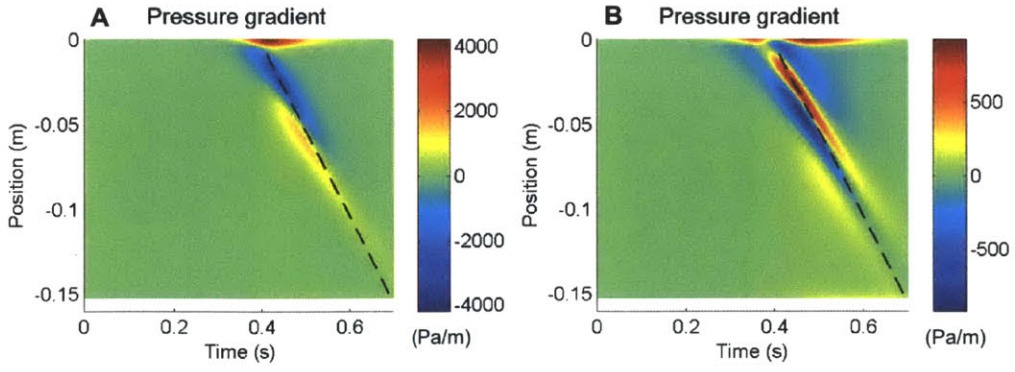

Figure 3-23: Pressure gradient signatures: (A) for a cylinder of $r = 0.5T$ and distance $d = 0.3T$ and (B) is the difference with a cylinder 1.5 times bigger and further away. A positive pressure gradient corresponds to an increase in pressure from the front of the foil to its tail.

Chapter 4

Experimental object identification

4.1 Experimental set-up

4.1.1 Instrumented hydrofoil and testing tank

Experiments have been conducted in the SMART (Singapore-MIT Alliance for Research and Technology) Centre testing tank in Singapore to test the method developed to identify objects in the flow using pressure sensors. The tank has dimensions $3.6 \times 1.2 \times 1.2$ meters. As shown in Figure 4-1A, the moving body used to generate flow motions and sense pressure is a NACA 0018 foil (chord $c = 15$ cm and span $s = 60$ cm) cast with internal 3.18 cm PVC tubing to transmit pressure from taps at the foil's mid span to the top. The foil is dragged past a static cylinder using an x-y gantry system supplied by Parker Engineering and controlled using Parker motor controllers and proprietary motion control software. Honeywell 19C015PG4K pressure sensors are mounted on top of the foil, and measurements are collected at a sampling rate of 500 Hz via a NI USB-6289 DAQ. The location of the sensor ports is shown in Figure 4-1B.

4.1.2 Flow visualization

Particle image velocimetry (PIV) is used to visualize the flow structures associated with measured pressure signals. PIV relies on the imaging of particles suspended

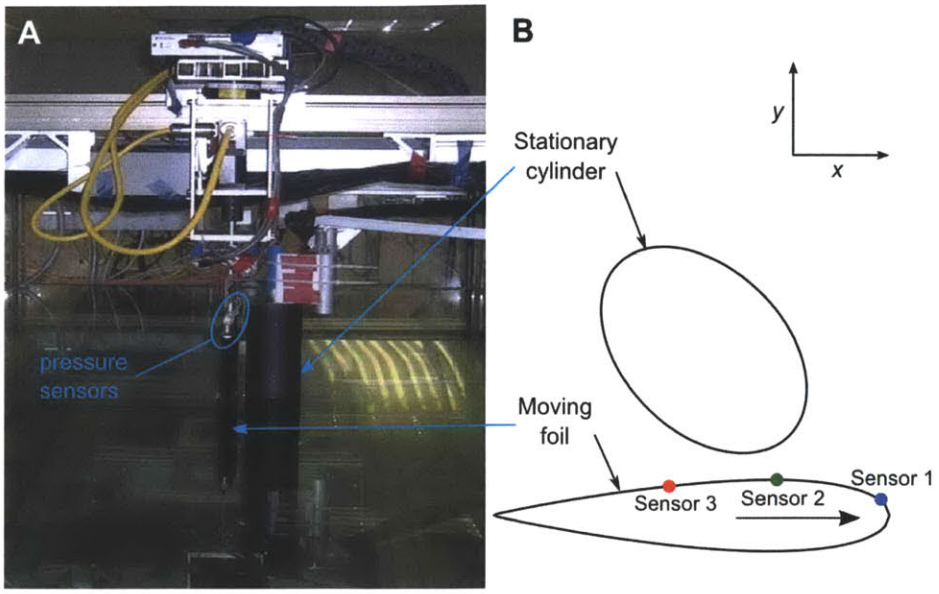

Figure 4-1: Experimental set-up. (A) picture of the experimental set-up (the foil is moving towards the photographer). (B) schematic of the cross-section of the experiment.

in the flow field using a high speed digital camera, and illuminated using a thin high-intensity laser sheet, as can be seen in Figure 4-2. PIV images represent a two-dimensional picture of the fluid flow. Post-processing is done on the images using correlation to create a vector field that can be used for visualization or calculation of flow characteristics. Imaging is accomplished using a Phantom V10 high-speed camera placed below the tank, using a 35 mm lens. The camera is capable of taking full resolution images of four megapixels at a frequency of 500 frames per second. For these experiments, frame rates are limited to 300 and 200 Hz and exposure times are between 1 and 3 milliseconds.

4.1.3 Experimental parameters

The foil is dragged at velocity $V = 0.5$ m/s past a static cylinder of elliptical cross section oriented at various angles. At its closest point, the foil is 5 to 10 mm away from the cylinder. The shape parameters (as defined in Eq. 2.2) of the elliptical cylinder are: $R = 3.81$ cm, $|\mu| = 0.2$. The major radius is oriented at $\pi/4$, $\pi/2$ or $3\pi/4$, which corresponds to $\alpha \in \{\pi/2,\ \pi,\ 3\pi/2\}$. The results from seven runs are

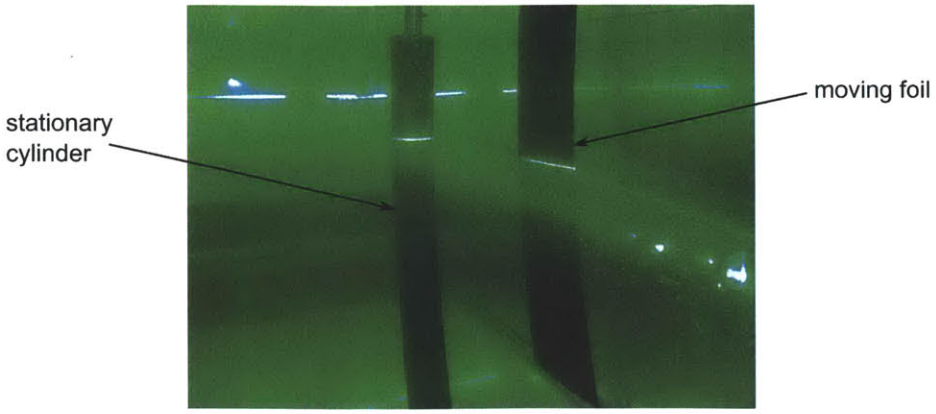

Figure 4-2: Flow visualization

discussed in the following paragraphs. The parameters for each run are summarized in Table 4.1 (where the axis of symmetry of the foil defines $y = 0$).

Table 4.1: Cylinder parameters

Run #	y/c	r/c	μ
1	0.43	0.25	-0.2
2	0.43	0.25	-0.2
3	0.43	0.25	-0.2
4	0.43	0.25	-0.2
5	0.43	0.25	$0.2i$
6	0.45	0.25	$0.2i$
7	0.43	0.25	$-0.2i$

4.2 Pressure measurements analysis

The length of the tank allows the foil to reach a steady state before passing the cylinder. As discussed in Section 3.1, the steady state is subtracted to the pressure measurements in all the analysis that follows. The mean slope of the pressure is also subtracted to the measurements to account for changes in hydrostatic pressure along the length of the tank.

4.2.1 Noise characteristics

Typical pressure traces (the pressure traces of Run 1) are shown in Figure 4-3A. Three distinct time periods are identified: before $t = 0$ s (before passing the cylinder), from $t = 0$ s to $t = 0.4$ s (while passing the cylinder) and after $t = 0.4$ s (after passing the cylinder). Before $t = 0$ s, the signal is dominated by noise. Figure 4-3B shows the corresponding power spectrum. The noise is clearly not white but the spectrum is rather messy, without any strong dominant component (the strongest component is around 30 Hz). Between $t = 0$ s and $t = 0.4$ s, the signal is dominated by the interaction between the foil and the cylinder: a clear pressure peak is measured by sensor 1, while sensors 2 and 3 measure a strong pressure drop. This time period will be discussed in more details in the next section. The last period, like the first one, is dominated by noise, but its characteristics are different. The noise of the last period is dominated by a low frequency (2 Hz) component, as confirmed by the power spectrum Figure 4-3C.

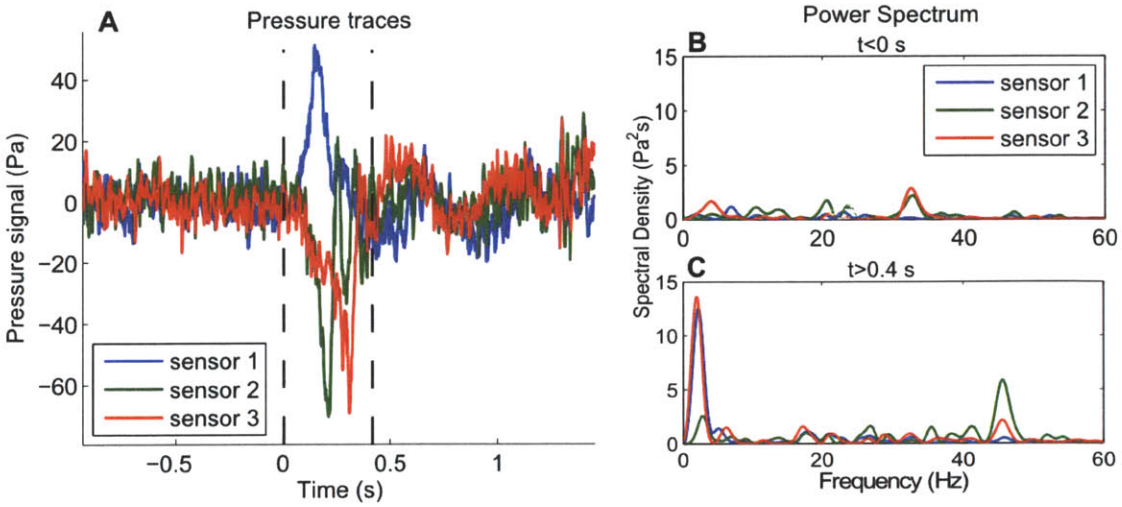

Figure 4-3: Pressure traces and power spectra

The main sources of noise are electrical noise from the motor and mechanical vibrations of the foil. The high frequency components (like the 30 Hz component) are most likely electrical noise, while low frequency components (like the 2 Hz component) are most likely due to mechanical oscillations of the foil. Other potential sources of

noise are electrical noise from other sources and background noise of the fluid flow. To take the noise and its variability into account, the measurement-noise covariance $\mathbf{R}^{\mathbf{e}}$ used in the UKF is calculated for each run based on the pressure measured 0.5 to 0.3 s before the characteristic drop of pressure at the second sensor (the matrices can be found in Appendix B).

4.2.2 Comparison between measured and simulated pressure

A close-up of the pressure measured by the sensors when passing the cylinder for Run 1 is plotted in Figure 4-4A in solid lines (the plots for all runs can be found in Appendix C). It is compared to the pressure predicted by the potential flow model (dashed lines). Here again, the time period can be split into two periods: from $t = 0$ s to $t = 0.2$ s, the measurements are noisy, but they match the predictions; for $t > 0.2$ s, predictions and measurements do not match any more. A vertical black dashed line indicates the time until which measurements and predictions match. As will be discussed in Section 5.4, the flow on the foil separates and this is why the potential flow model stops being valid. Only pressure measurements before the black dashed line are used to locate and identify the cylinder.

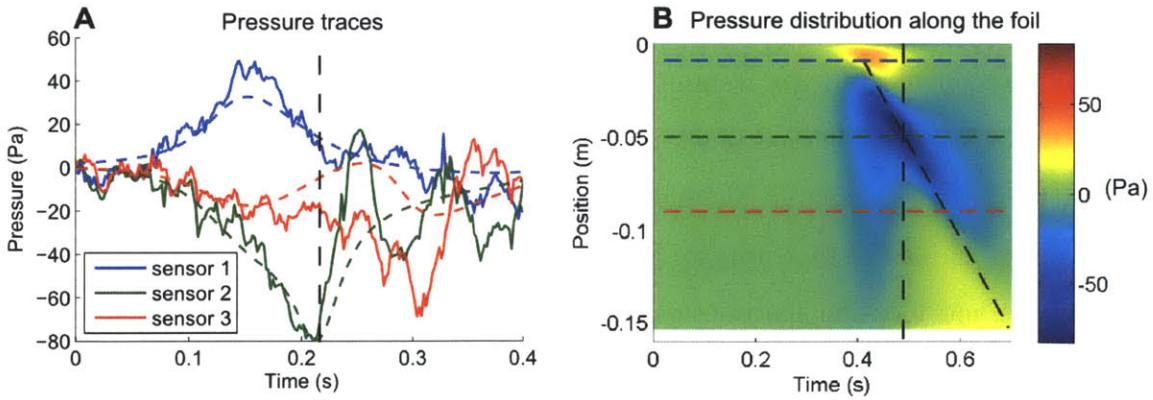

Figure 4-4: Theoretical and measured pressure on a foil passing a cylinder.

The theoretical spatio-temporal pressure distribution along the foil is also plotted in Figure 4-4B, showing the sensor locations (horizontal dashed lines), the position of the cylinder center as respect to the foil (oblique dashed line), and the time at which the model stops being valid (vertical dashed line). The figure shows that the first

sensor is located where the pressure peak is largest, while the second one, located at maximum width, lies where the pressure drop is strongest. It can also be observed that the flow roughly starts separating when the maximum width of the foil passes the cylinder.

4.3 Object identification using pressure measurements

4.3.1 Process noise

In addition to noise, several sources of error affect the process of identifying a cylinder based on pressure measurements. In the measurements themselves, an error of a few pascal in the subtraction of the steady and hydrostatic pressure is very likely. The pressure sensors might also have a slight drift. Modeling is the other main source of error. Modeling errors can be geometric (errors in the shape of the foil, location of the sensors, finite expansion for the shape of the cylinder, ...) or hydrodynamic (mostly viscous effects). To account for all these errors, an artificial process noise is added to the state-space representation of the problem. Since this noise is artificial, it cannot be directly measured but has to be empirically estimated. The process-noise covariance is chosen of the simplest form: diagonal with two degrees of freedom—one for the size and location parameters (x/c, y/c and R/c) and the second one for the shape parameters (μ_x and μ_y). The generic process-noise covariance is therefore:

$$\mathbf{R^e} = \begin{bmatrix} a & 0 & 0 & 0 & 0 \\ 0 & a & 0 & 0 & 0 \\ 0 & 0 & a & 0 & 0 \\ 0 & 0 & 0 & b & 0 \\ 0 & 0 & 0 & 0 & b \end{bmatrix} \tag{4.1}$$

a and b are empirically chosen such as to optimize the performance of the filter. The values chosen for the present experiments are:

$$a = 4.4 \times 10^{-6}$$
$$b = 2.5 \times 10^{-5}$$

4.3.2 Strategy and initialization

Due to the amount of correlated noise and errors inherent to the experiments, all attempts to fully identify the cylinder (location and geometry) in one pass have been unsuccessful. However, fish have been observed to pass several times in front of new objects ([33]), and it seems reasonable to assume that they first locate the objects and estimate their size before refining their shape estimate. A similar approach is used here: the first pass is used to get a first estimate of the position (x and y) and size (R) of the cylinder. A second pass (using the same data) refines the first guess and estimates the shape parameters (μ_x and μ_y).

For all experiments, the UKF starts as the pressure stops being statistically zero and is initialized with 100% error. The covariance matrix is empirically initialized to:

$$\mathbf{P}_{\mathbf{x}_0} = \begin{bmatrix} 0.4 & 0 & 0 \\ 0 & 0.4 & 0 \\ 0 & 0 & 0.4 \end{bmatrix} \tag{4.2}$$

After the first pass, the final location and size estimates are used to initialize the UKF for the second pass, and the shape parameters are initialized to zero (a circle). The covariance matrix of the second pass is initialized as a block diagonal matrix. The first block is the final covariance matrix of the first pass augmented by 4×10^{-3} on the diagonal (to account for the fact that the best estimate under circular assumption might not be the same as under elliptical assumption) and the second block is $\left(\begin{smallmatrix} 0.04 & 0 \\ 0 & 0.04 \end{smallmatrix}\right)$. The UKF starts slightly later for the second pass than for the first pass so as to emphasize the data that have the lowest noise/signal ratio.

4.3.3 An example of object identification

The process of cylinder size and location estimation as described above is shown in Figure 4-5 for Run 6. The evolution of the three parameters is plotted in solid lines. They all stay above their theoretical value (dashed lines) during most of the run, but end up converging to their theoretical value. Configurations corresponding to four times indicated by letters a to d are also sketched. The dashed blue ellipse shows the actual position and shape of the cylinder while the red circle shows the UKF estimate of the position and size of the cylinder at the corresponding time.

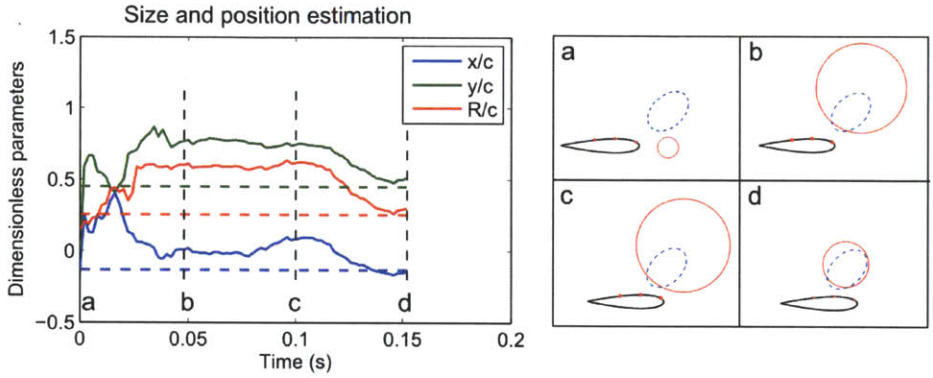

Figure 4-5: Experimental object localization

Figure 4-6 shows the evolution of all parameters during the second pass. The value of the location and size parameters, identified during the first pass, do not significantly change during the second pass. The shape parameters immediately jump to their actual value and then slightly oscillate around this value.

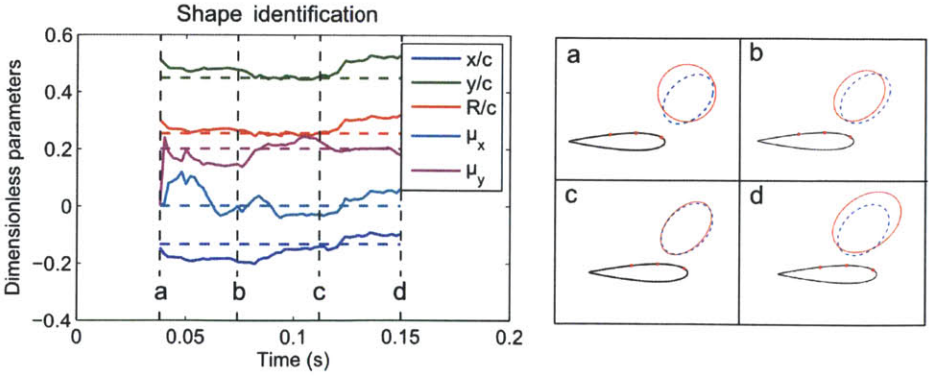

Figure 4-6: Experimental object identification

Figure 4-7 shows the measured (solid lines), filtered by UKF (dashed lines) and predicted by theory (dotted lines) pressure for the first (Figure 4-7A) and second pass (Figure 4-7B). As can be seen, the measurements are very noisy, especially at sensor 3, but the filtered pressure is very close to the predicted pressure, especially during the second run. It appears clearly that as the filtered pressure gets closer to the predicted pressure, the estimated shape gets closer to the actual shape of the cylinder. This run is the perfect example of the first pass being used to get a rough estimate of the size and location of the cylinder, and the second pass building on the estimates of the first one to get a more precise estimate of the object shape.

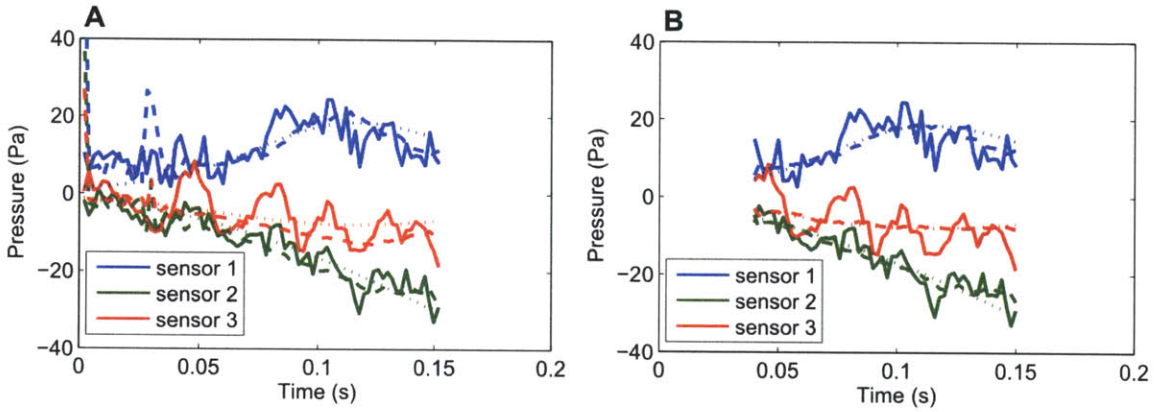

Figure 4-7: Measured (solid lines), filtered by UKF (dashed lines) and predicted by theory (dotted lines) pressure for the first (A) and second (B) pass.

4.3.4 Performance of experimental object detection and identification

The plots showing the evolution of the estimated parameters as well as the measured, filtered and predicted pressure traces for all runs can be found in Appendix D. It can be seen that all object localizations are quite accurate. It is interesting to notice that the estimated circle best fits the part of the ellipse that is closest to the foil. Similarly, even when the global shape of the ellipse is not very accurately identified (like in Run 4), the estimated ellipse fits very well the bottom part of the cylinder. Run 5 and 7 are also interesting. For these runs, despite the fact that the size is not very well

estimated, the shape estimate is surprisingly accurate. The object size and shape are encoded separately and, to some extent, they can be estimated independently.

We will now look more globally at the performance of experimental object identification and compare it to the performance predicted by our analysis in 3.4.1. The results of experimental object identification are summarized in Table 4.2. For each run, Table 4.2 displays:

- $\sigma = \sqrt{\| \mathbf{R^c} \|_2}$
- $\tilde{y} = y/T$, the actual vertical position of the cylinder center
- $\tilde{r} = r/T$, the actual mean radius of the cylinder
- μ, the actual shape parameter of the ellipse
- $\tilde{d} = d/T = \tilde{y} - \tilde{r}|1 - \mu| - 0.5$, the minimum distance between the foil and the cylinder
- $\Delta\tilde{y}/\tilde{y}$, the error percentage in final estimate of the vertical position of the cylinder center
- $\Delta\tilde{r}/\tilde{r}$, the error percentage in final estimate of radius of the cylinder
- $\Delta\tilde{d}/\tilde{d}$, the error percentage in final estimate of the minimum distance between the foil and the cylinder

Using the analysis developed in Section 3.4.1, with $\Delta p_0 = 10$ Pa, we expect distance and radius errors on the order of $0.4\tilde{d}$, which is very close to observed errors.

Finally, it is interesting to notice that the distance to the cylinder is the parameter that is best estimated, which stands even more clearly if absolute errors are considered instead of percentages. This indicates that the distance to the cylinder might be a more relevant parameter than the object center location. We also observed that the portion of the ellipse that is closest to the foil is usually best estimated. These two observations suggest that a local surface parameterization might be more appropriate to the use of pressure sensors than our global shape parameterization. Moreover,

Table 4.2: Results of experimental object identification

Run #	σ	$\tilde{y}$	$\tilde{r}$	μ	$\tilde{d}$	$\Delta\tilde{y}/\tilde{y}$	$\Delta\tilde{r}/\tilde{r}$	$\Delta\tilde{d}/\tilde{d}$	$\lvert\Delta\mu\rvert$
1	6	2.4	1.4	-0.2	0.2	0.2	0.2	0.1	0.3
2	8	2.4	1.4	-0.2	0.2	0.2	0.1	0.1	0.3
3	8	2.4	1.4	-0.2	0.2	0.003	0.2	0.1	0.2
4	9	2.4	1.4	-0.2	0.2	0.2	0.1	0.1	0.1
5	7	2.4	1.4	$0.2i$	0.5	0.3	0.3	0.4	0.1
6	7	2.5	1.4	$0.2i$	0.6	0.2	0.3	0.2	0.1
7	8	2.4	1.4	$-0.2i$	0.5	0.3	0.5	0.1	0.1

in the perspective of underwater vehicle navigation, a local characterization that could apply to any obstacle would also be more appropriate than a global shape identification.

Chapter 5

Discussion and further simulations

5.1 Sensing range

Hydrodynamic imaging is known to be a short-range sense ([36]), and in the experiments discussed in the previous chapter, the foil passes less than 0.1 body length from the object. How far away can an object be detected (depending on its size), and is there a way to increase this distance?

The first half of the question has been investigated in Section 3.4.1 based on the amplitude of the pressure signal. We will now look at the actual performance of the algorithm using simulated pressure data. The pressure is simulated using the algorithm described in Section 2.3, and a white Gaussian noise of variance 20 Pa^2 is added to simulate noise of magnitude comparable to experimentally observed noise (see Appendix B). The other parameters used in the simulations are set to the values identified for the experiments (Section 4.3.1 and 4.3.2) and the strategy described in Section 4.3.2 is used to identify the object. The cylinder used in the simulations has shape parameters $r = T$, $\mu_x = -0.2$ and $\mu_y = 0.1$ and the speed of the foil is set to $V = 0.5$ m/s.

Using these parameters and strategy, it is found that the detection range is about $d = T$. A localization and identification process is shown in Figure 5-1A&B for such a distance. At that distance, it takes a while before the foil notices the presence of the object, but once it detects it ($t \simeq 0.1$ s), the position and size parameters con-

vergence is very fast. Figure 5-1C&D show the corresponding simulated (solid lines) and filtered by UKF (dashed lines) pressure traces.

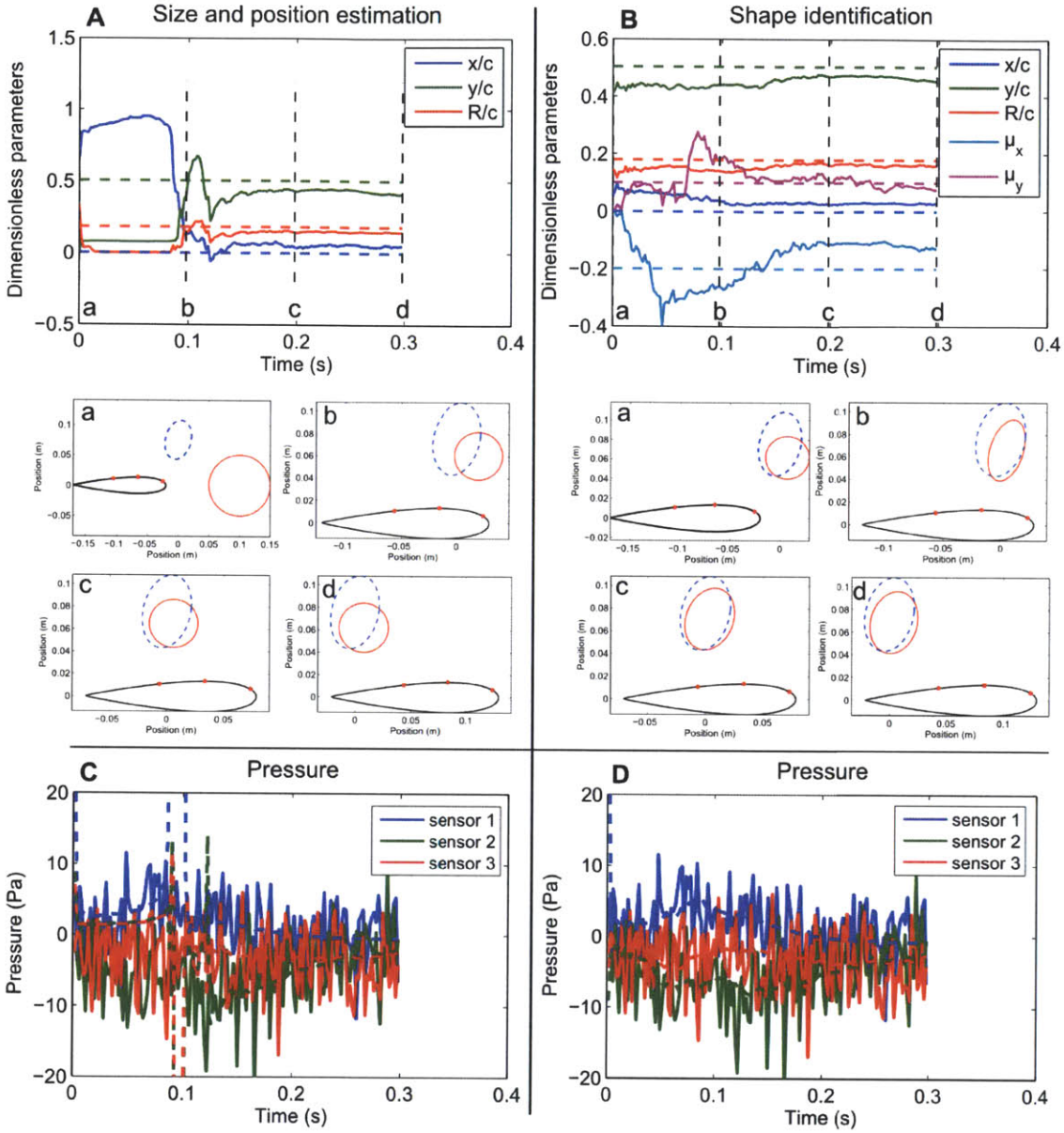

Figure 5-1: Identification of an ellipse located at maximum sensing distance.

The pressure signal amplitude at that distance is around 8 Pa, i.e. between once and twice the standard deviation of the noise. Table 5.1 summarizes the object identification performance in this simulation. It displays the (final) estimates and their respective error, as well as the corresponding Δp_0 based on the analysis of Section 3.4.1. The values found for Δp_0 are about one order of magnitude smaller than the

noise standard deviation. These results show that our UKF is very good at filtering white Gaussian noise. In the presence of white Gaussian noise, our algorithm can achieve estimates much more accurate than would be expected from the value of the standard deviation. However, the distance at which it can detect objects is still dictated by the noise standard deviation. It seems that the main limitation of the algorithm is its sensing range.

Table 5.1: Object identification performance using simulated data

Parameter	$\tilde{r}$	$\tilde{y}$	$\tilde{d}$	μ
Value	1	2.8	1	$-0.2+0.1i$
Error	0.1	0.2	0.05	0.07
Δp_0	2	X	1	0.5

In all the cases considered so far, the flow is generated by the moving foil. However, as discussed in Section 3.1, the presence of an outside flow can considerably increase the amplitude of the pressure signal, thus allowing objects to be detected further away. The same simulation as described above has been run with the addition of an outside flow of velocity $U = 0.1$ m/s oriented against the motion of the foil. It is found that the object can be detected as far as $d = 2.5T$ away from the foil. This is a considerable improvement (as compared to $d = T$ in static water), for the addition of a relatively slow outside flow. The convergence of the location and shape parameters at that distance is shown in Figure 5-2A&B. The corresponding measured and filtered pressure (respectively solid and dashed lines) are shown in Figures 5-2C&D. Like in the absence of outside flow, the amplitude of the pressure signal is comprised between once and twice the standard deviation of the noise.

In reality, the presence of outside flow might increase the ambient noise, which is not taken into account here, but it clearly has the potential to increase the detection range.

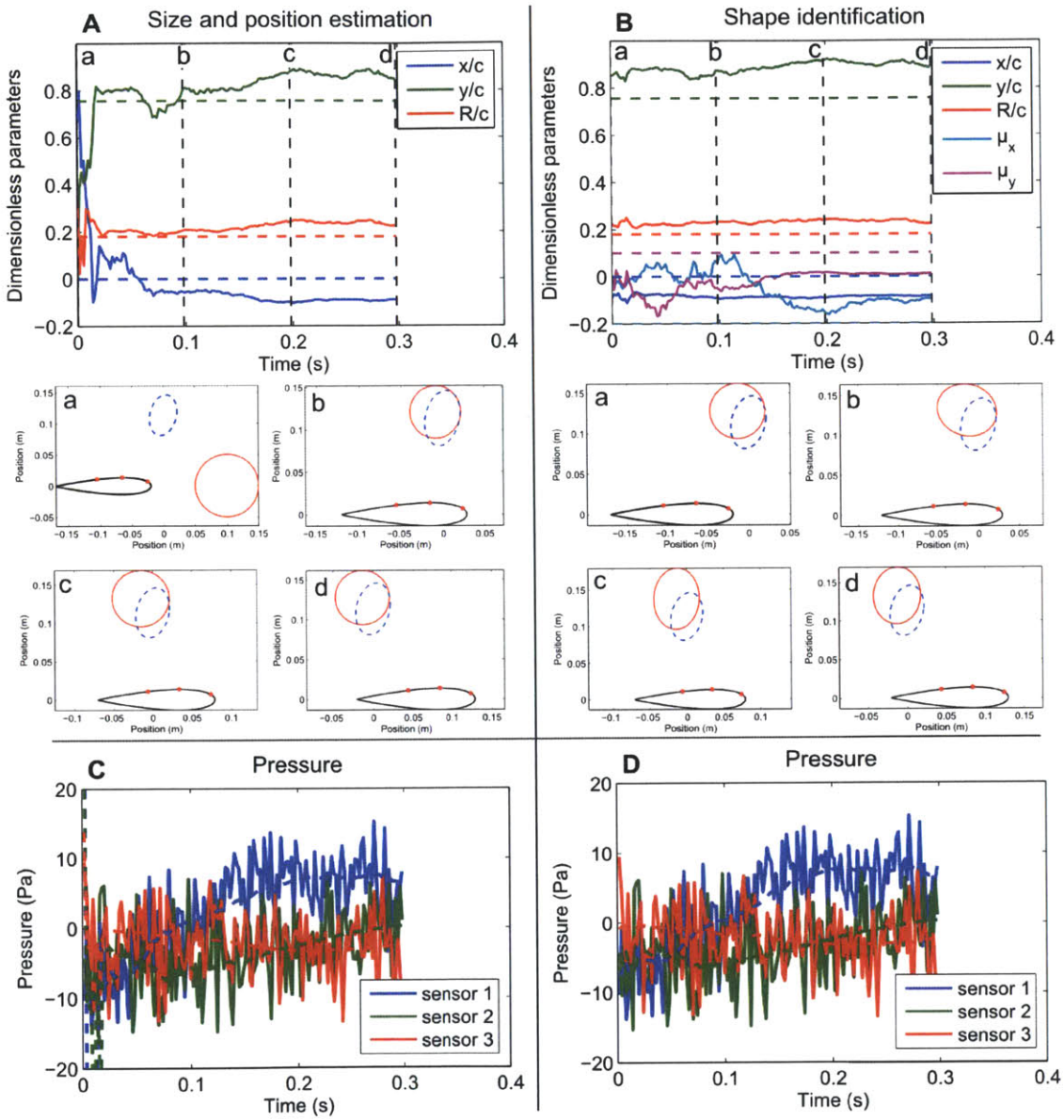

Figure 5-2: Identification of an ellipse located at maximum sensing distance with outside flow.

5.2 Impact of sensor density on object identification

Another limitation of the algorithm performance using experimental measurements is the very limited number of pressure sensors used. Due to the available sensor size, only three pressure sensors have been used in the experiments described in Chapter 4. With three sensors, an error or drift of a few pascals on any sensor can seriously impair the performance of object detection and identification.

To illustrate this phenomenon, the same simulation as the one described in Section 5.1 (without external flow) has been run, simulating a drifting sensor. A linear drift reaching 10 Pa at $t = 0.3$ s has been added to sensor 2 to simulate a drifting sensor (so it is a drift of 33 Pa/s). The drift does not significantly impair the ability to detect the presence of the object, but it strongly affects the global performance of object localization and identification. As can be seen in Figure 5-3A, when the object is detected (shortly before $t = 0.1$ s), the estimates quickly jump to values close to their actual value, but then drift away (unlike in Figure 5-1A). The second pass (Figure 5-3B) does not improve the size and location estimate and the final estimated shape is very different from the actual shape. Figures 5-3C&D show the corresponding pressure traces.

Having more pressure sensors would make the algorithm performance less sensitive to the presence of a faulty sensor. The simulations with and without the faulty sensor have been run with a denser array of pressure sensors (20 sensors equally distributed on the front two third on both sides of the foil). As can be seen in Figure 5-4A, increasing the sensor density does not increase the distance at which objects can be detected, but it significantly increases the convergence speed of the parameters. Figure 5-4 shows the results of object detection and identification using the denser array of pressure sensors.

When one of the sensors is faulty, the advantage of having a denser array of pressure sensors is more significant. Figure 5-5 shows the results of object detection and identification with an array of 20 pressure sensors, with the one located at maximum width on the side of the object having a linear drift. As expected, the drift of one

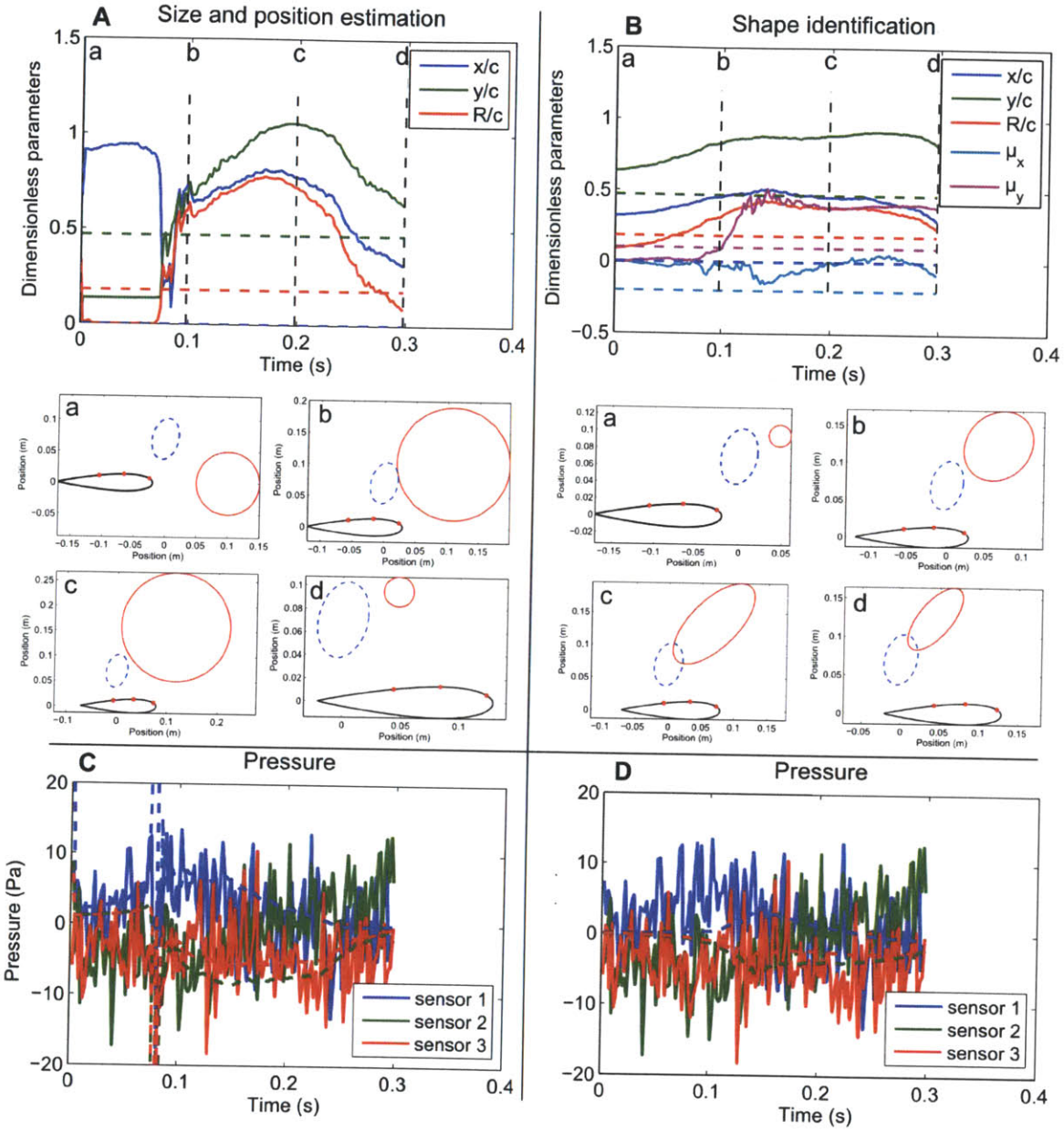

Figure 5-3: Identification of an ellipse located at maximum sensing distance, with a drifting sensor

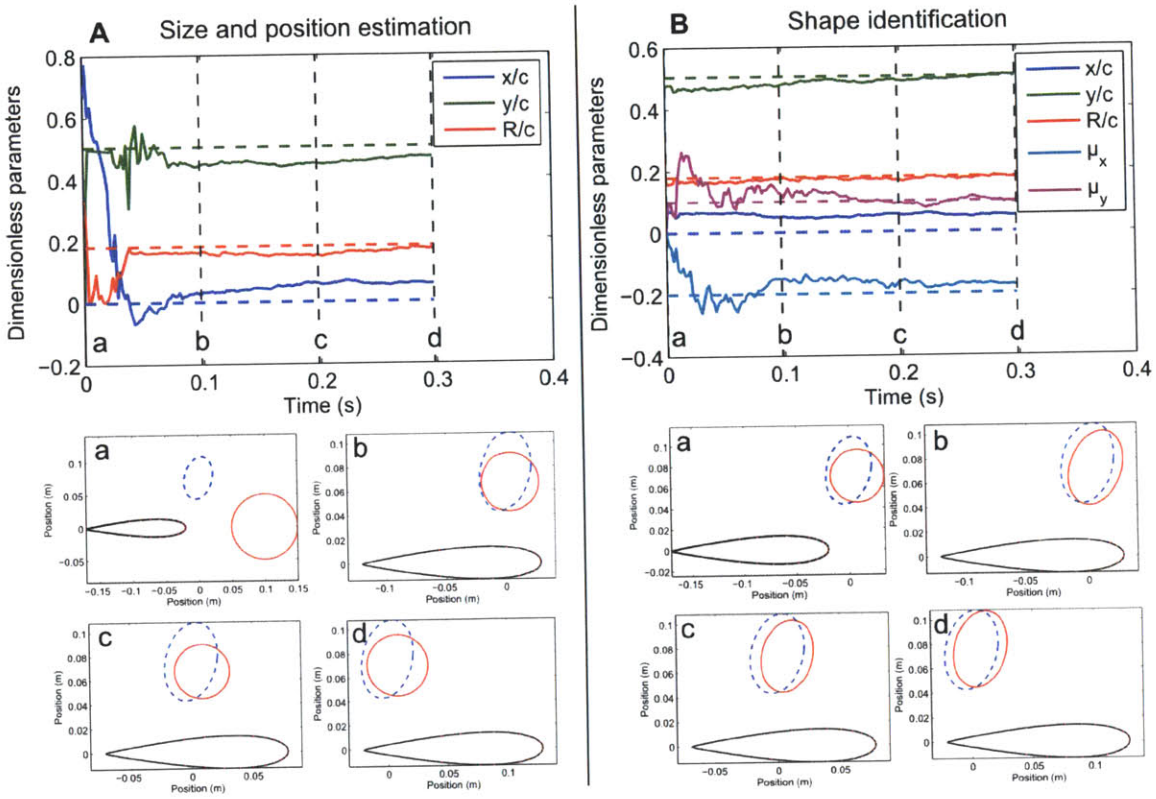

Figure 5-4: Identification of an ellipse located at maximum sensing distance, with a denser array of pressure sensors

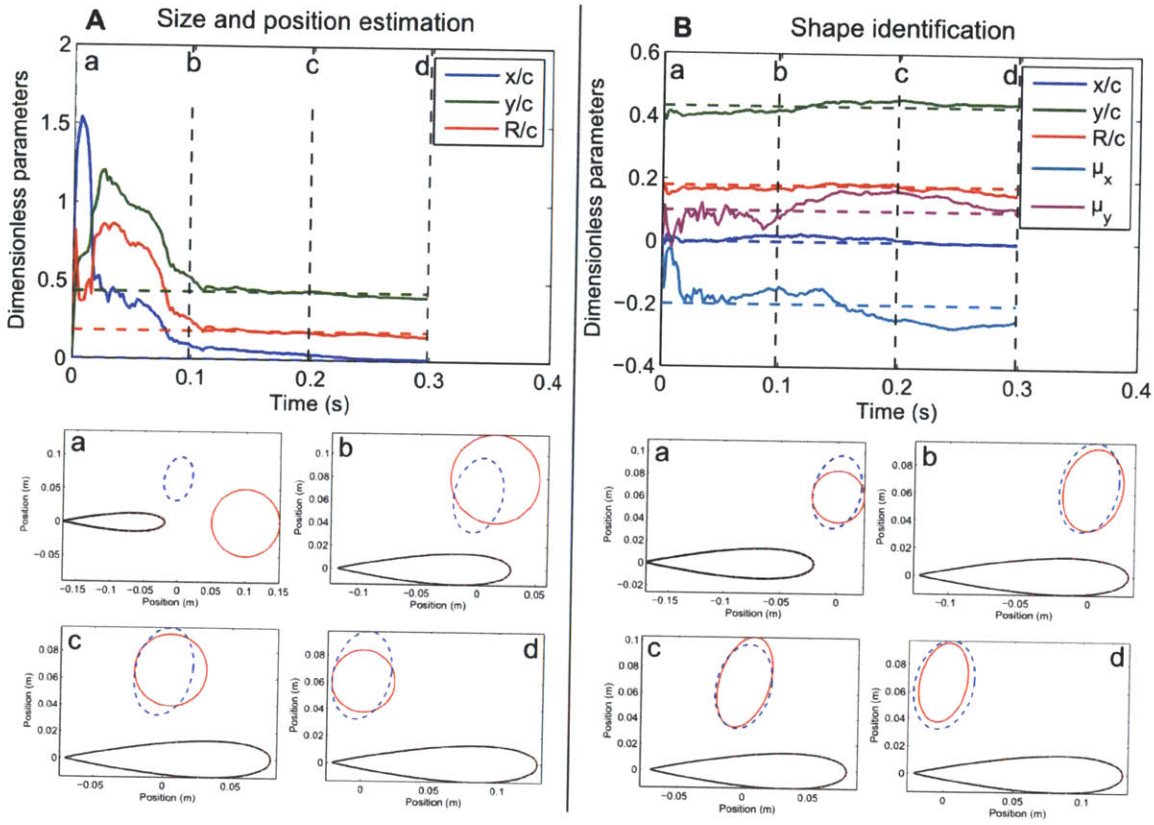

Figure 5-5: Identification of an ellipse located at maximum sensing distance, with a drifting sensor in a denser array of pressure sensors

sensor goes unnoticed in the presence of a dense array of pressure sensors.

More interestingly, a dense array of pressure sensors is also more robust to a given probability of failure of the pressure sensors. For example, consider sensors that have a probability 1/3 of drifting. Assume the slope of the drifting sensors is given by a normal distribution of mean 0 and standard deviation 33.33 Pa/s. Figure 5-3 illustrates this case with 3 sensors (except that the drift is not randomly chosen) and Figure 5-6 illustrates it with 20 sensors, one every three sensors drifting. Comparing Figures 5-3 and 5-6 shows that increasing the number of sensors improves the convergence of the object identification algorithm and the accuracy of the final estimate.

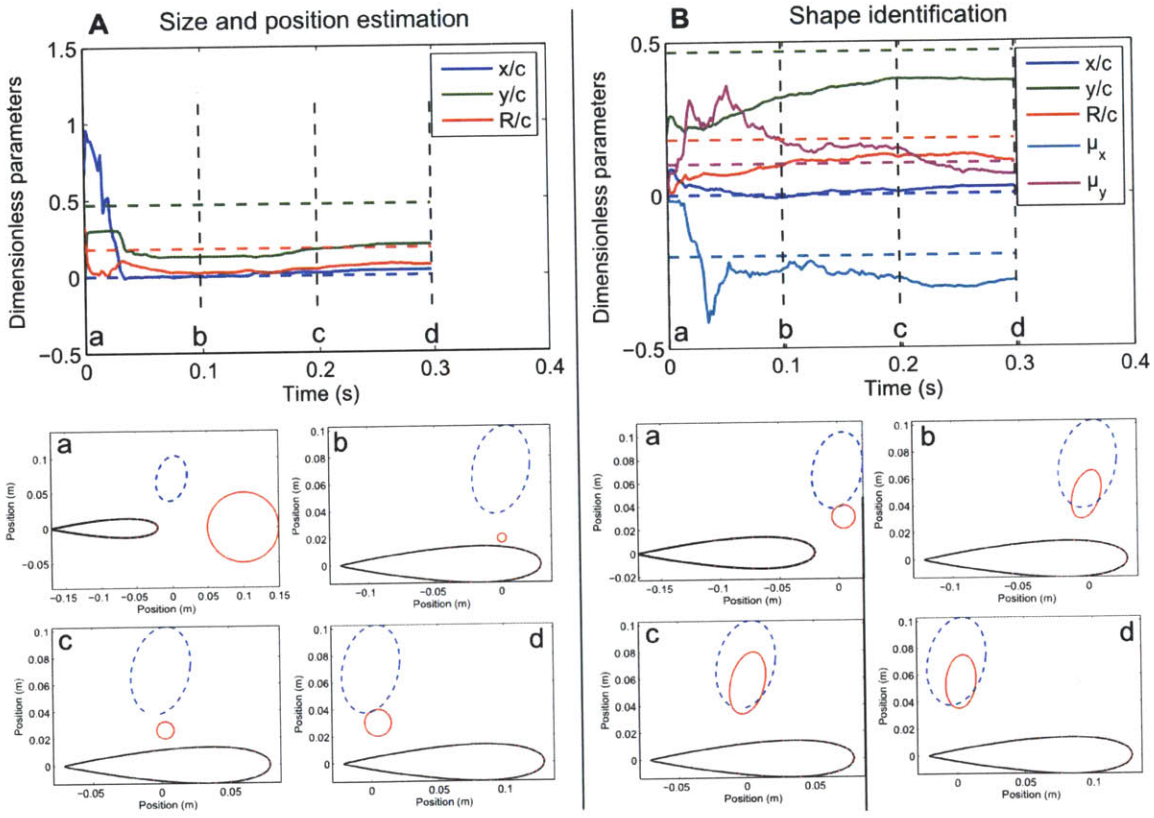

Figure 5-6: Identification of an ellipse located at maximum sensing distance, with 1/3 of the pressure sensors drifting

A dense array of pressure sensors is therefore more robust to a probability of some sensors being defective, but there is also another reason why you might want to use a dense array of pressure sensors. One way to estimate the appropriate sensor density is to simply look at the pressure gradient along the foil passing an object, as done in

Section 3.4.2. An alternative approach is to examine the effect of sensor density on object identification performance.

It has been observed in Section 3.1, that in the active sensing scheme, sampling frequency and sensor density are not equivalent, due to the fact that the pressure signal along the foil does not simply translate in time. Therefore, there might be an optimal sensor density below which the lack of spatial density cannot be compensated by a higher sampling frequency. The optimal density might very well depend on the size and distance of the cylinder, but by way of example, the case of the foil passing at $d = 0.3T$ from a cylinder with geometry parameters $R = 1.5$ cm and $\mu = 0.2i$ is investigated here. White Gaussian noise of standard deviation 2 Pa is added to the simulated pressure measurements. Between 10 and 70 pressure measurement points are evenly distributed along the front two thirds of the foil (as illustrated in Figure 5-7C) and the sampling rate (f) is chosen as the ratio $f = 20000/(\text{number of sensors})$ (such that the average frequency is 500 Hz). The final error is calculated as $E = \frac{1}{5}\left(\frac{\Delta R}{R} + \frac{\Delta x}{R} + \frac{\Delta y}{R} + \Delta\mu_x + \Delta\mu_y\right)$, where $\Delta(\cdot)$ is the difference between the final estimate an the actual value of parameter $(\cdot)$. For each simulation, the convergence time (time elapsed before $E < 0.2$) and the final error is calculated. Each case is simulated twelve times and the time of convergence and final error mean and standard deviation are plotted (Figure 5-7A&B). Both convergence time and final error plots suggest that, at least for the configuration considered here, when the sensor spacing is greater than 5 mm, the performance of the object identification decreases. Amazingly, the optimal spacing suggested by these observations scales with the actual spacing of lateral line canal neuromasts in the trunk canal of blind Mexican cave fish that can be estimated from Figure 1-1A (roughly 1 mm for a 6 cm long fish).

5.3 Pressure sensors or pressure gradient sensors?

The work presented in this thesis is based on pressure measurements. However, canal neuromasts of fish are known to respond to pressure gradients ([7]). Would there be

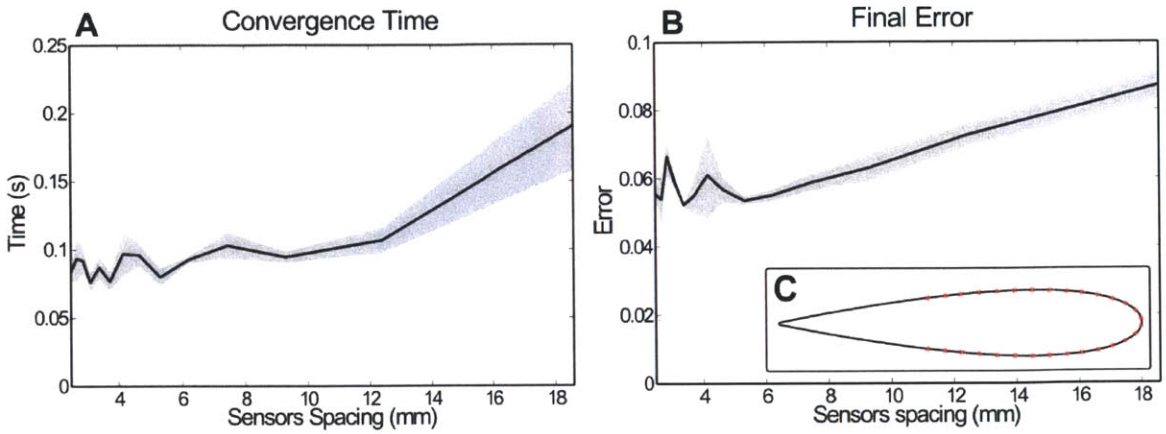

Figure 5-7: Convergence time (A) and final error (B) of the object identification as a function of sensor spacing. (C) shows the sensor locations for a spacing of 6 mm.

any advantage in using pressure gradient sensors instead of pressure sensors? As we shall see, probably...

When moving in open water, a fish creates a pressure field that it can recognize as being its own. In the case of a simple forward motion, this pressure field is characterized by a high pressure at the front, and low pressure along the main part of the body (Figure 3-4A). When gliding past an object, the pressure change induced by the presence of the object can be quite small compared to the ambient pressure field, which is why, in this study, the steady pressure field has been subtracted to every pressure trace. However, as can be seen in Figure 5-8A, the ambient pressure gradient along the body is pretty small. So measuring the pressure gradient (as fish do) reduces the ratio signal of interest over total pressure (except at the very front of the foil). As was mentioned in the introductory chapter of the thesis, this is one of the advantages of the lateral line canal subsystem over the superficial subsystem.

Moreover, using pressure gradient instead of gradient would annihilate the need to take into account the hydrostatic pressure and subtract the steady pressure. Since both have been identified as potential sources of errors, getting rid of them should improve the performance of the algorithm.

Figure 3-4A also suggests distinct uses of the head and trunk canals. As investigated by Windsor [37], when approaching a wall head-on, the increase in pressure gradient is confined to the head. Figure 3-4A shows that, when gliding past an object,

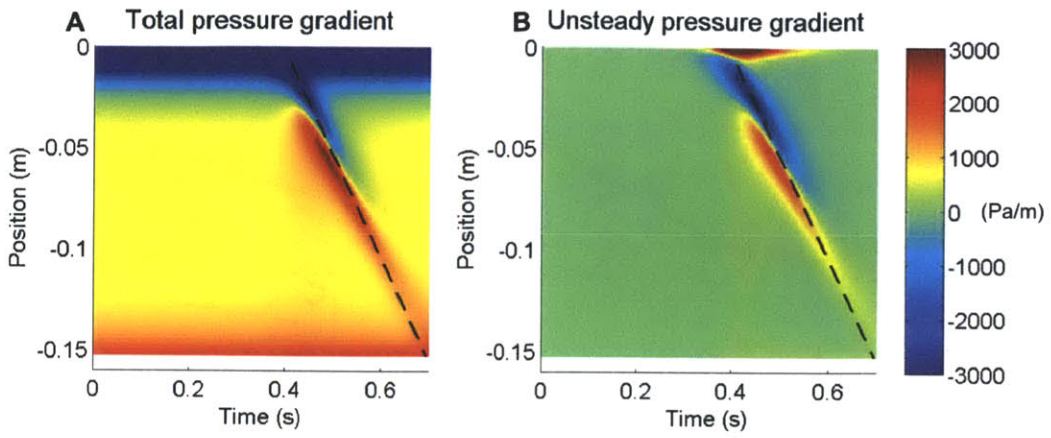

Figure 5-8: Pressure gradient signature

no noticeable change in pressure gradient happens along the head. Therefore, head canal neuromasts are probably mostly used for obstacle avoidance while the trunk ones serve for object identification.

5.4 Limits of the potential flow model

The results from Section 4.3 demonstrate that object localization and recognition are possible with experimental pressure measurements. However, only the pressure measured before the maximum width of the foil passes the cylinder are compatible with our model. Indeed, as has been observed in Section 4.2.2, the potential flow model stops being valid after this point. Flow visualization has been used to investigate the transition that causes the potential flow model to stop being valid (the set-up is described in Section 4.1).

Figure 5-9 compares the velocity field predicted by the inviscid model to the experimental velocity field measured using Particle image velocimetry. As can be seen, both flows are quasi-identical everywhere, except in a small region materialized by green and orange ellipses. To get finer details of the flow characteristics in the small region of interest, an individual particle has been followed, and its pathline is marked in green in Figure 5-10. It appears very clearly in the frame sequence that between $t = 0$ s and $t = 0.1$ s the particle is in a laminar flow, but between $t = 0.1$ s and

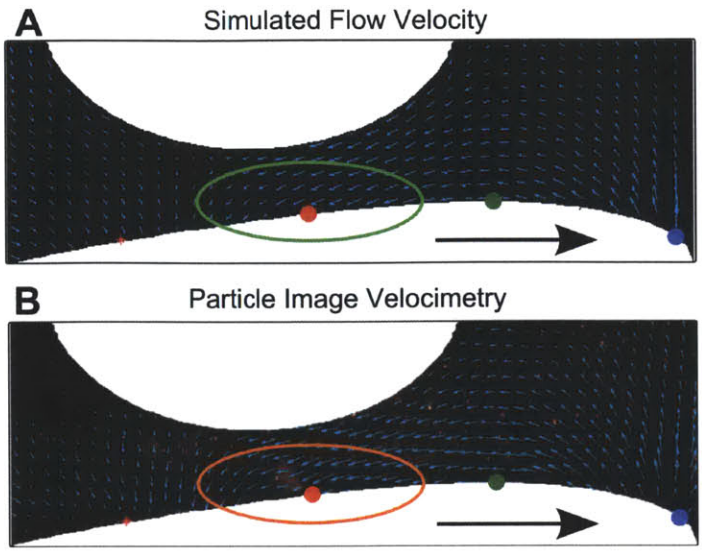

Figure 5-9: Comparison between experimental and simulated velocity field

$t = 0.2$ s, the flow separates, as the particle starts swirling. Separation affects the entire pressure field around the foil.

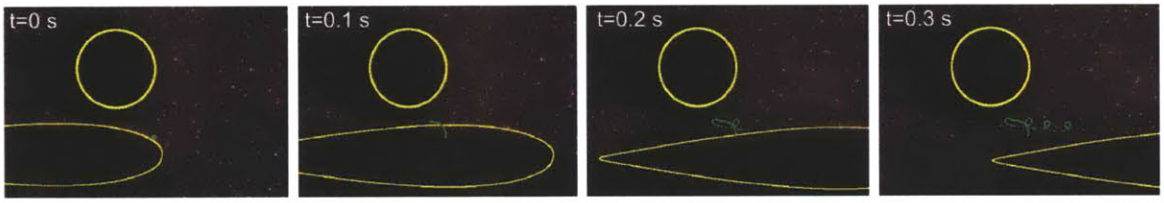

Figure 5-10: Flow separation: a pathline

Figure 5-11 shows the pressure gradient distribution along the foil as it passes the cylinder for the configuration of Runs 1 to 4. The pressure sensor locations are represented by horizontal dashed lines, an oblique line marks the position of the cylinder and a vertical line marks the approximate time when the potential flow model stops being valid. This line also coincides with the onset of a strong adverse pressure gradient (orange patch in the middle of the figure), which theoretically explains why the flow separates.

Viscous effects were already known to strongly affect the signal measured by surface neuromasts as well as the dynamics of the flow in the canals ([35]). However, in the cases previously studied (vibrating sphere), viscous effects did not affect the pressure gradient measured by canal neuromasts ([29]). We show here that in the case

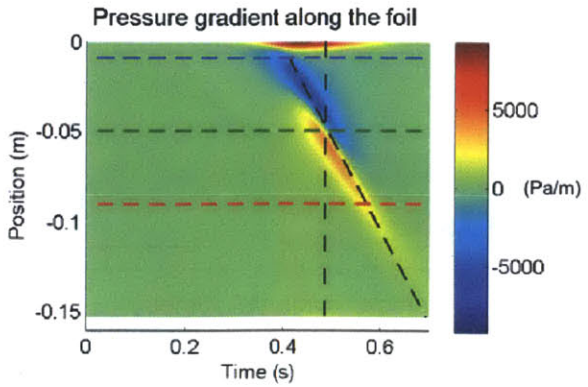

Figure 5-11: Unsteady pressure gradient along thee foil

of a fish gliding past an object, viscous effects strongly influence the signal measured by canal neuromasts.

Chapter 6

Conclusions

The blind Mexican cave fish, able to dart in the dark and identify the shape of static objects in static water by gliding past them, has been used as an inspiration for a novel object identification algorithm based on pressure sensors. A two-dimensional potential flow approach based on a source panels method has been used to characterize the pressure distribution on a vehicle passing a static object in stationary flow. A shape parameterization inspired from conformal mapping was applied to independently encode the position, size and shape of the object. Finally, the unscented Kalman filter has been adapted to take into account the fact that two bodies cannot physically intersect.

Experiments have been run in a tank, using an instrumented foil moving past a cylinder, to test the method developed. The algorithm has proved to be very successful at locating the cylinder, and mostly successful at identifying it, despite a strongly correlated noise. It has been observed that since the location and size are encoded separately, the shape of the cylinder can be identified even when the size and location estimates are slightly offset.

Based on simulations using a NACA 0018 foil to model the fish, the distance at which an object can be detected (depending on its size) has been estimated. It has been found that for the amount of noise experienced in the laboratory, the sensing range is about the width of the foil. However, simulations have shown that the sensing range can be significantly increased in the presence of an outside flow.

The experiments performed used three commercial pressure sensors and it has been shown that increasing the number of pressure sensors should make object detection and identification more efficient and more robust to sensor failures. Estimates based on typical pressure gradient values and object identification performances, independently suggested that a spacing of 5 mm between pressure sensors was optimal. These estimates justify the need in micro mechanical pressure sensors for efficient object identification.

In this study, the steady pressure has been subtracted from every measured and simulated pressure to make the pressure generated by the cylinder more noticeable. This need can however be eliminated by measuring pressure gradient, as fish actually do. We have also observed that while the front 10% of the fish (or foil) is key to obstacle avoidance, measurements along the following 50% are essential to object identification.

Finally, we have shown that the potential flow model gives accurate predictions of the pressure field, until the flow separates.

Chapter 7

Recommendations for future work

On the experimental side, running experiments described in Chapter 3 with a denser array of pressure sensors (ideally a dense array of micro pressure sensors, when those become available), would allow a better comparison between the pressure field predicted by our potential flow model and the measured pressure.

Simulating the interactions between the moving foil and the stationary object in viscous flow would also help identify the impact of viscosity on the pressure measured along the foil. A learning algorithm could then be used to develop an efficient (on-line) algorithm that uses both potential flow and viscous features of the flow to identify objects.

The unscented Kalman filter has been observed to be more efficient at object identification than at object detection. In the case of an underwater vehicle navigating in an unknown environment, it would be advantageous to use an efficient detection algorithm and limit the use of the unscented Kalman filter to object identification.

Finally, investigating object identification has brought insight into parameters that affect the pressure along a body exploring its environment. We have observed that the distance of the object is a more relevant parameter than its center position. We have also observed that the pressure along the foil is much more sensitive to the nearby portion of the object than to its global shape. Moreover, when navigating underwater, knowing the shape and position of the closest boundaries and obstacles is probably more useful than knowing the actual shape of relatively small objects.

Therefore, a more local shape or boundary parameterization should be considered in the future.

Appendix A

Alternative definition of sensitivity

In this Appendix you will find the same figures as in Section 3.3 with the sensitivity defined as the integral over the length of the foil and over time of $|\mathrm{d}p/\mathrm{d}x|$.

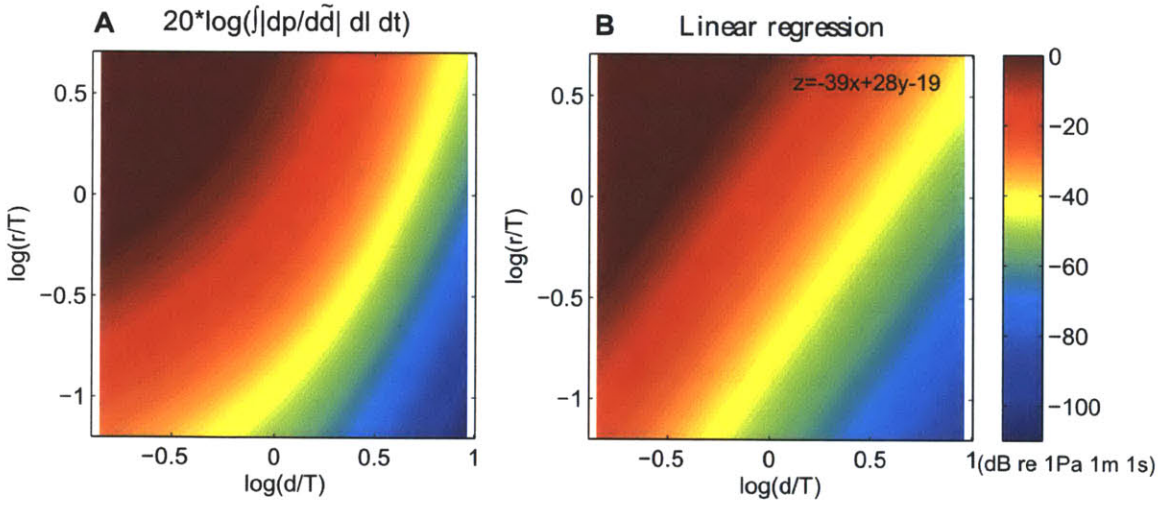

Figure A-1: Sensitivity to distance

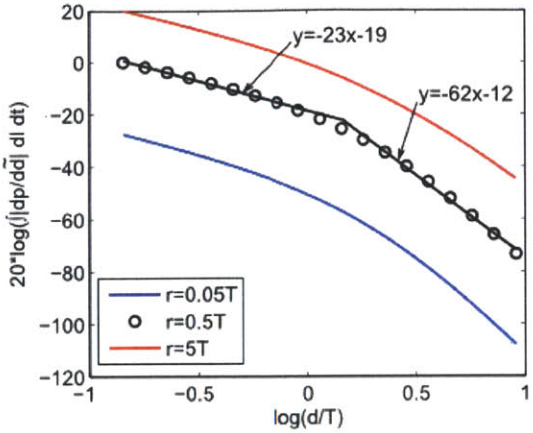

Figure A-2: Sensitivity to distance for fixed sizes

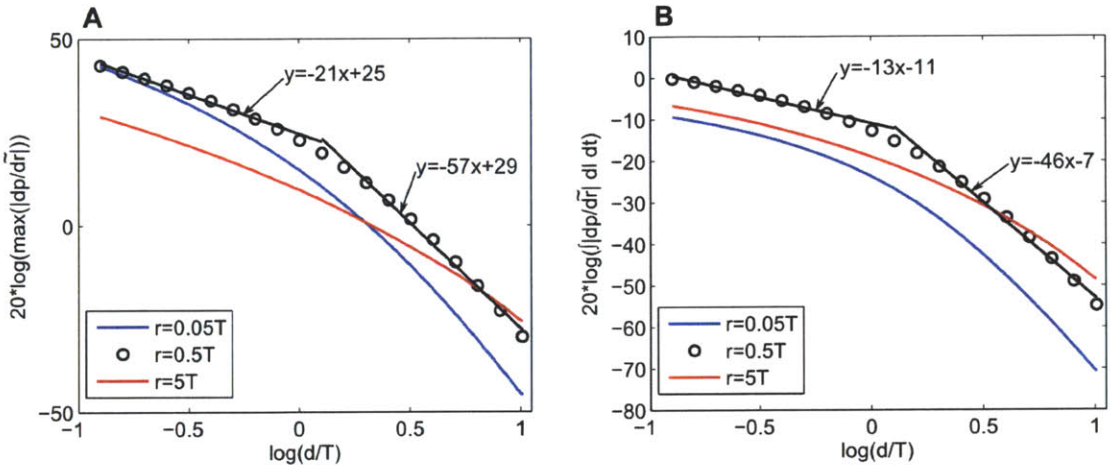

Figure A-3: Sensitivity to size

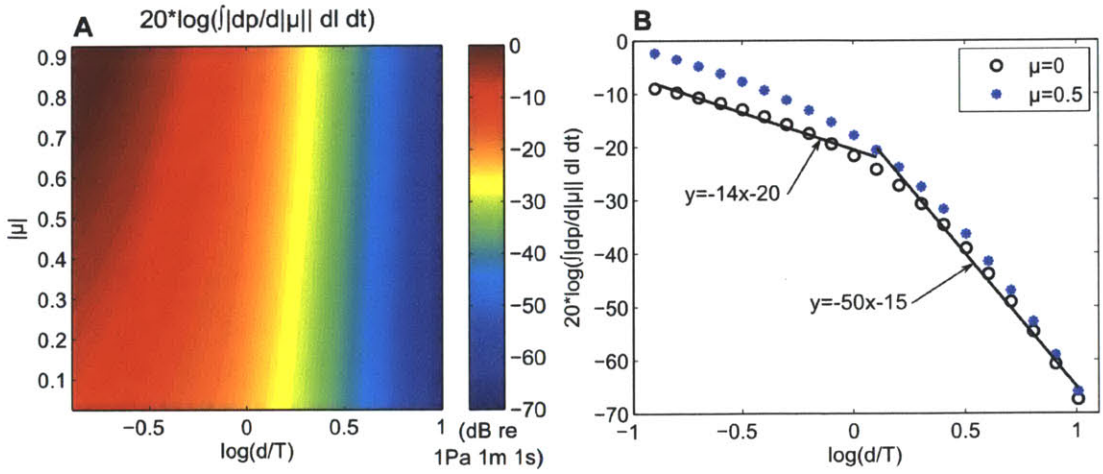

Figure A-4: Sensitivity to eccentricity for a horizontal ellipse

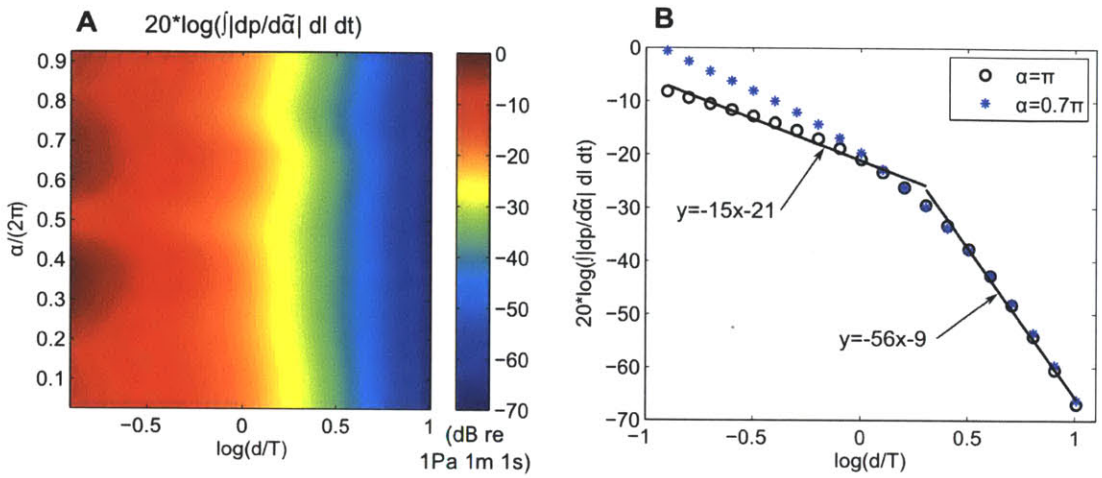

Figure A-5: Sensitivity to orientation

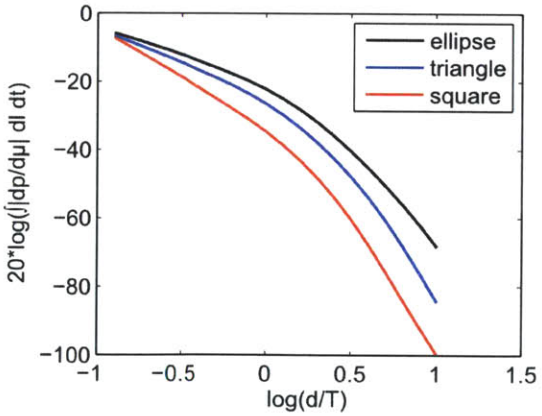

Figure A-6: Sensitivity to shape

Appendix B

Measurement-covariance matrices

Measurement-covariance matrices (in Pa^2) for experiments (Chapter 4) and simulations (Chapter 5) are gathered in this appendix.

Run 1

$$\mathbf{R^c} = \begin{bmatrix} 13 & 3 & 3 \\ 3 & 32 & 12 \\ 3 & 12 & 16 \end{bmatrix} \tag{B.1}$$

Run 2

$$\mathbf{R^c} = \begin{bmatrix} 21 & 7 & 6 \\ 7 & 42 & 14 \\ 6 & 14 & 27 \end{bmatrix} \tag{B.2}$$

Run 3

$$\mathbf{R^c} = \begin{bmatrix} 27 & 4 & 5 \\ 4 & 45 & 21 \\ 5 & 21 & 29 \end{bmatrix} \tag{B.3}$$

Run 4

$$\mathbf{R^c} = \begin{bmatrix} 28 & 9 & 7 \\ 8 & 60 & 24 \\ 7 & 24 & 22 \end{bmatrix} \tag{B.4}$$

Run 5

$$\mathbf{R^c} = \begin{bmatrix} 29 & 9 & 9 \\ 9 & 14 & 11 \\ 9 & 11 & 22 \end{bmatrix} \tag{B.5}$$

Run 6

$$\mathbf{R^c} = \begin{bmatrix} 22 & 10 & 13 \\ 10 & 14 & 16 \\ 13 & 16 & 35 \end{bmatrix} \tag{B.6}$$

Run 7

$$\mathbf{R^c} = \begin{bmatrix} 26 & 14 & 18 \\ 14 & 15 & 18 \\ 18 & 18 & 36 \end{bmatrix} \tag{B.7}$$

Simulations

$$\mathbf{R^c} = \begin{bmatrix} 20 & 0 & 0 \\ 0 & 20 & 0 \\ 0 & 0 & 20 \end{bmatrix} \tag{B.8}$$

Appendix C

Pressure measurements figures

In this appendix, the pressure traces from the experiments (solid lines) and the pressure traces predicted from the potential flow model (dashed lines) are displayed.

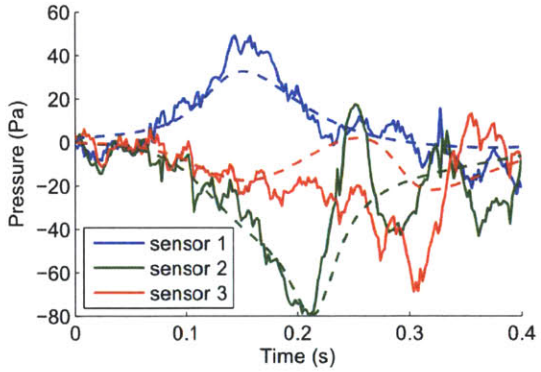

Figure C-1: Pressure measurements, Run 1

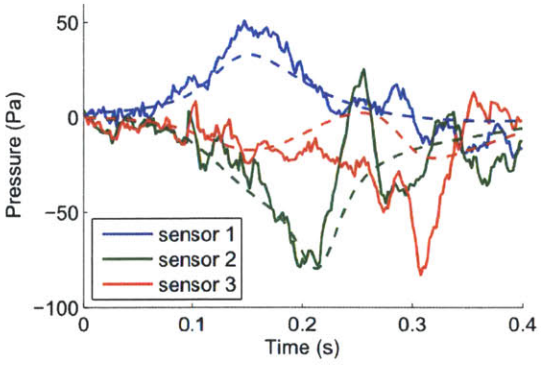

Figure C-2: Pressure measurements, Run 2

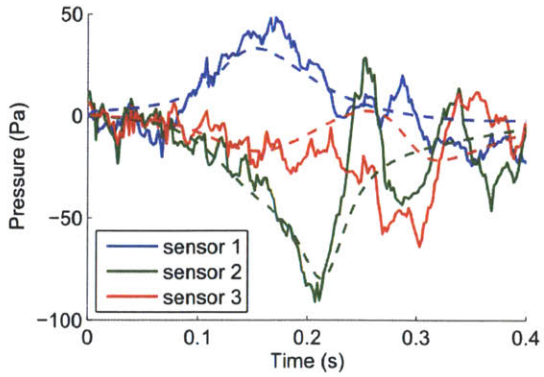

Figure C-3: Pressure measurements, Run 3

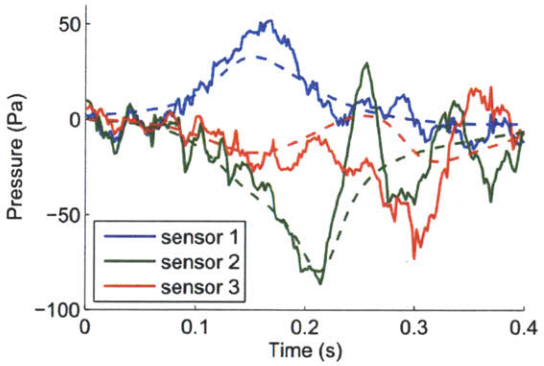

Figure C-4: Pressure measurements, Run 4

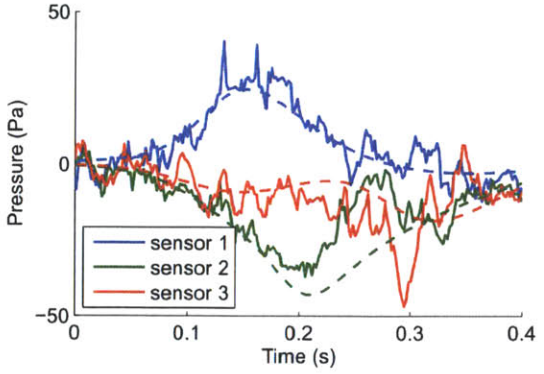

Figure C-5: Pressure measurements, Run 5

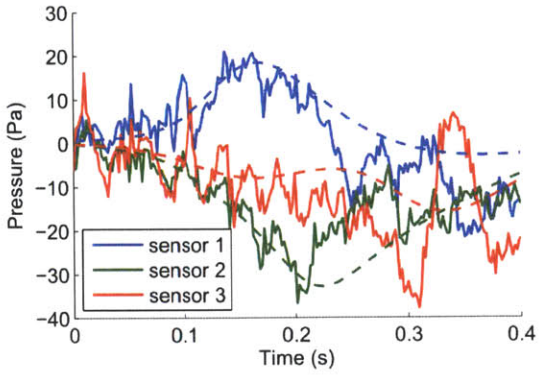

Figure C-6: Pressure measurements, Run 6

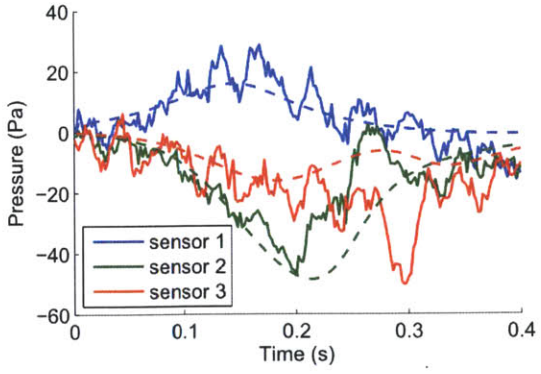

Figure C-7: Pressure measurements, Run 7

Appendix D

Experimental object identification figures

This appendix shows the the convergence of the estimated parameters for experimental object localization (on the left) and identification (on the right). It also compares the shape of the estimated object (in red) to the actual object (dotted blue ellipse) for several times. It finally shows as the measured (solid lines), filtered by UKF (dashed lines) and theoretical (dotted lines) pressure traces.

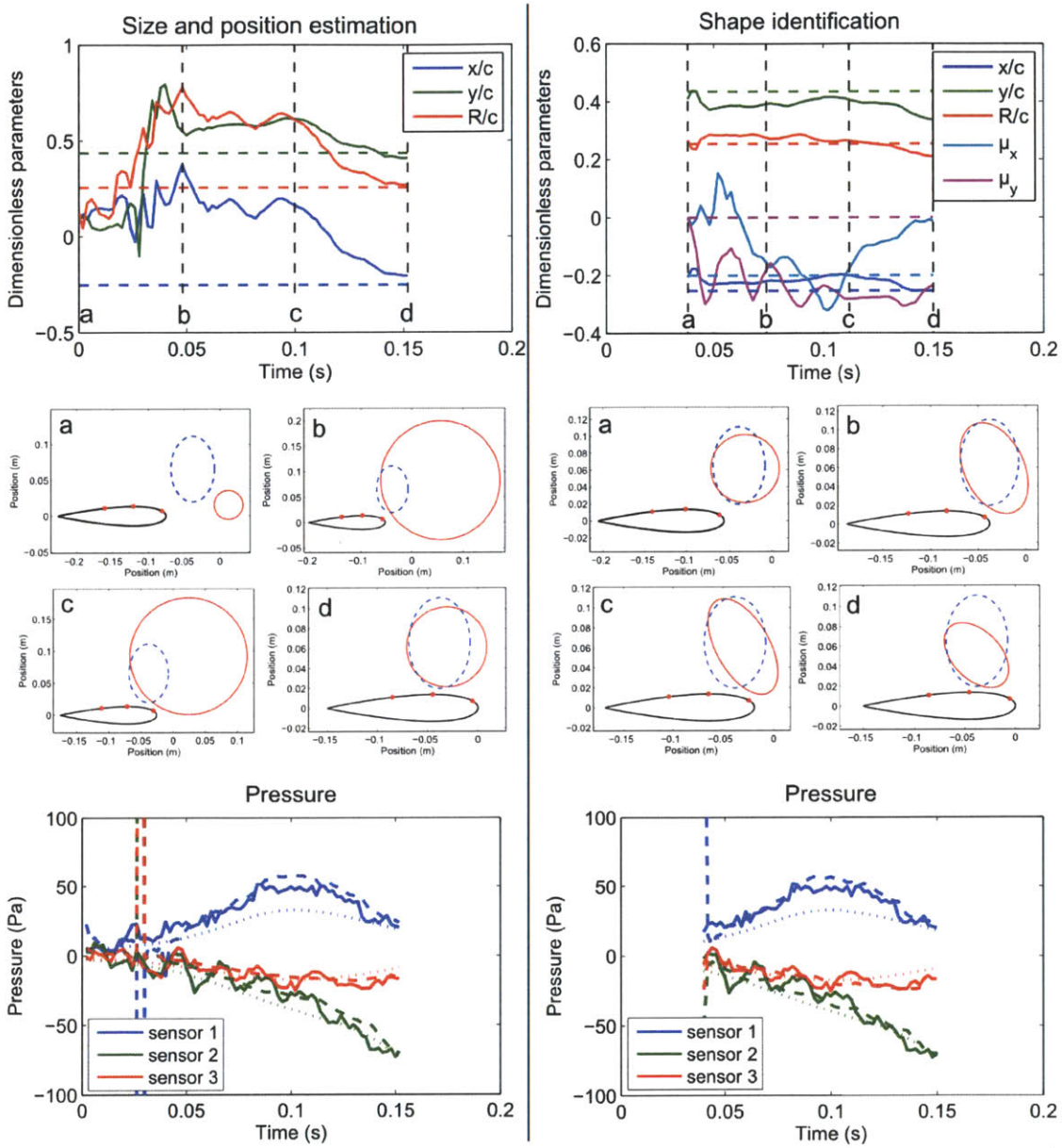

Figure D-1: Object identification, Run 1

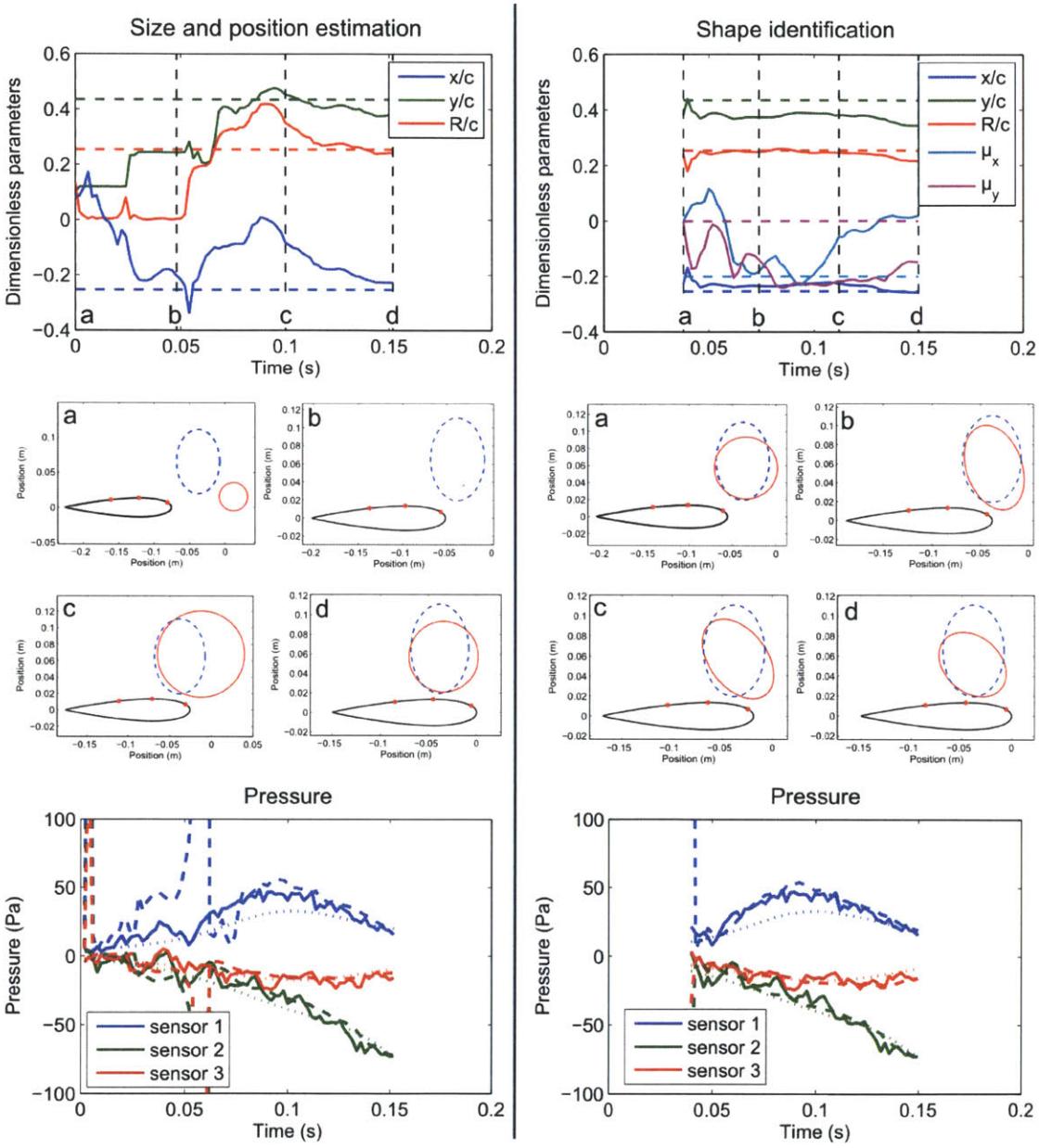

Figure D-2: Object identification, Run 2

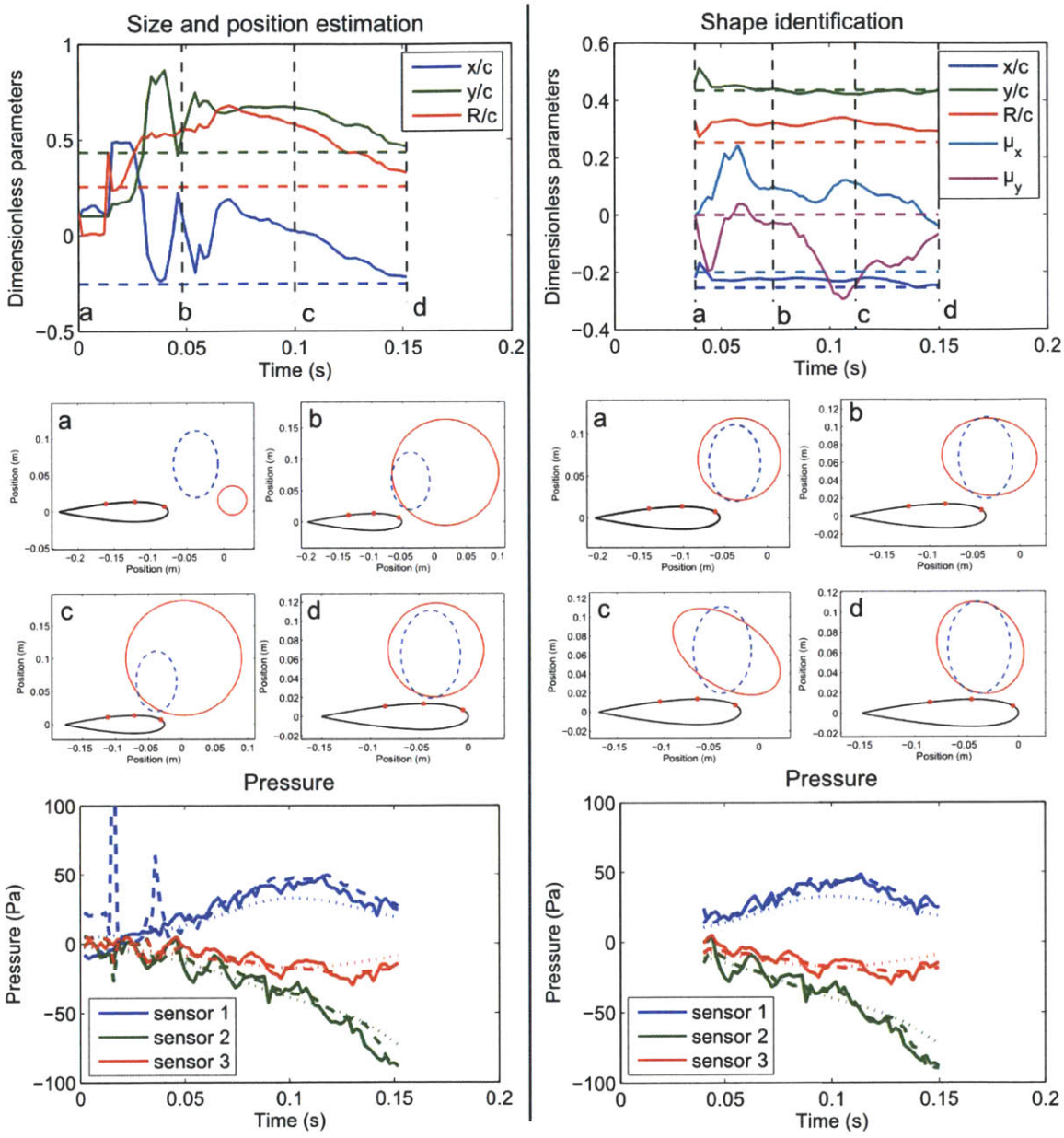

Figure D-3: Object identification, Run 3

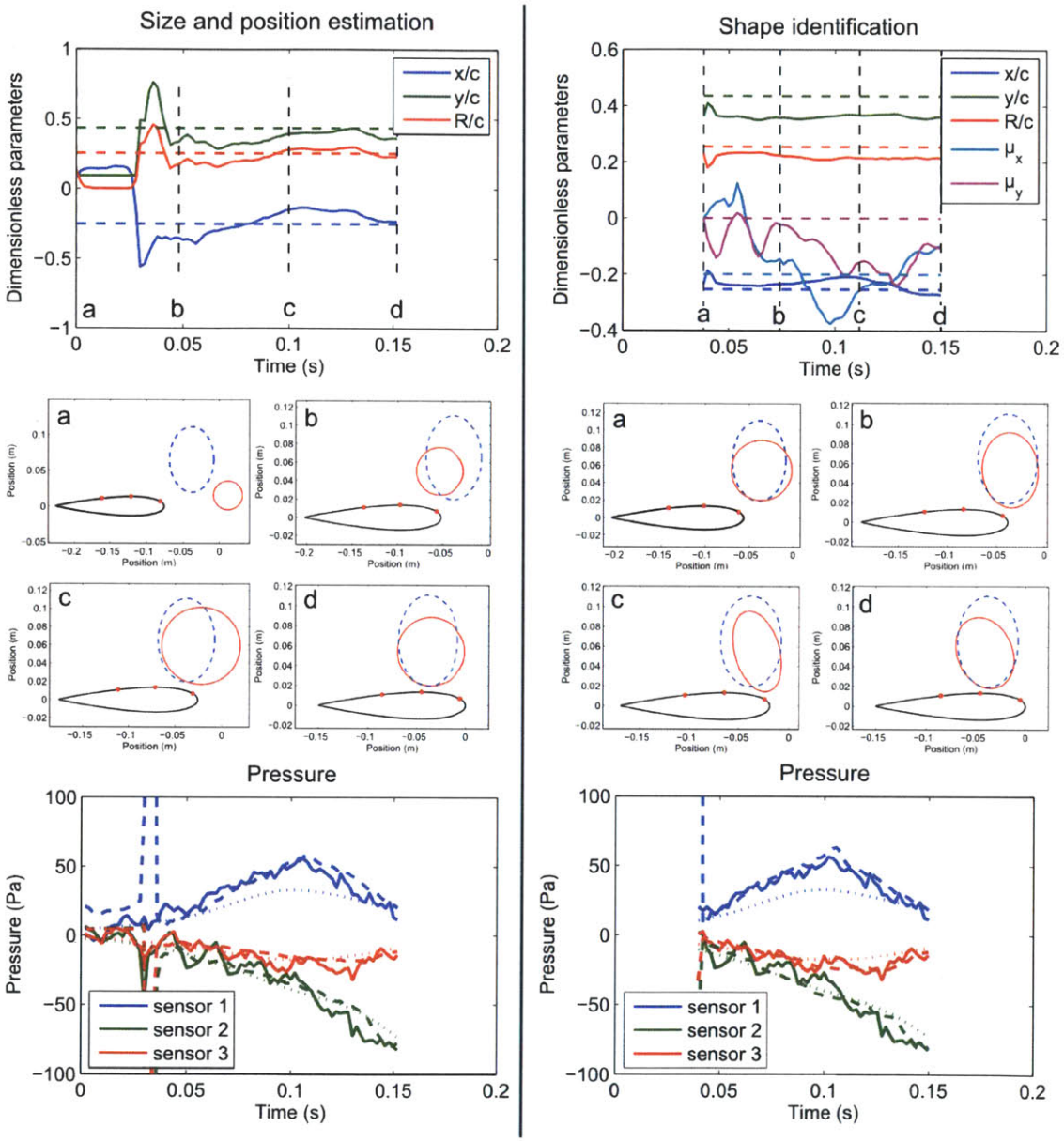

Figure D-4: Object identification, Run 4

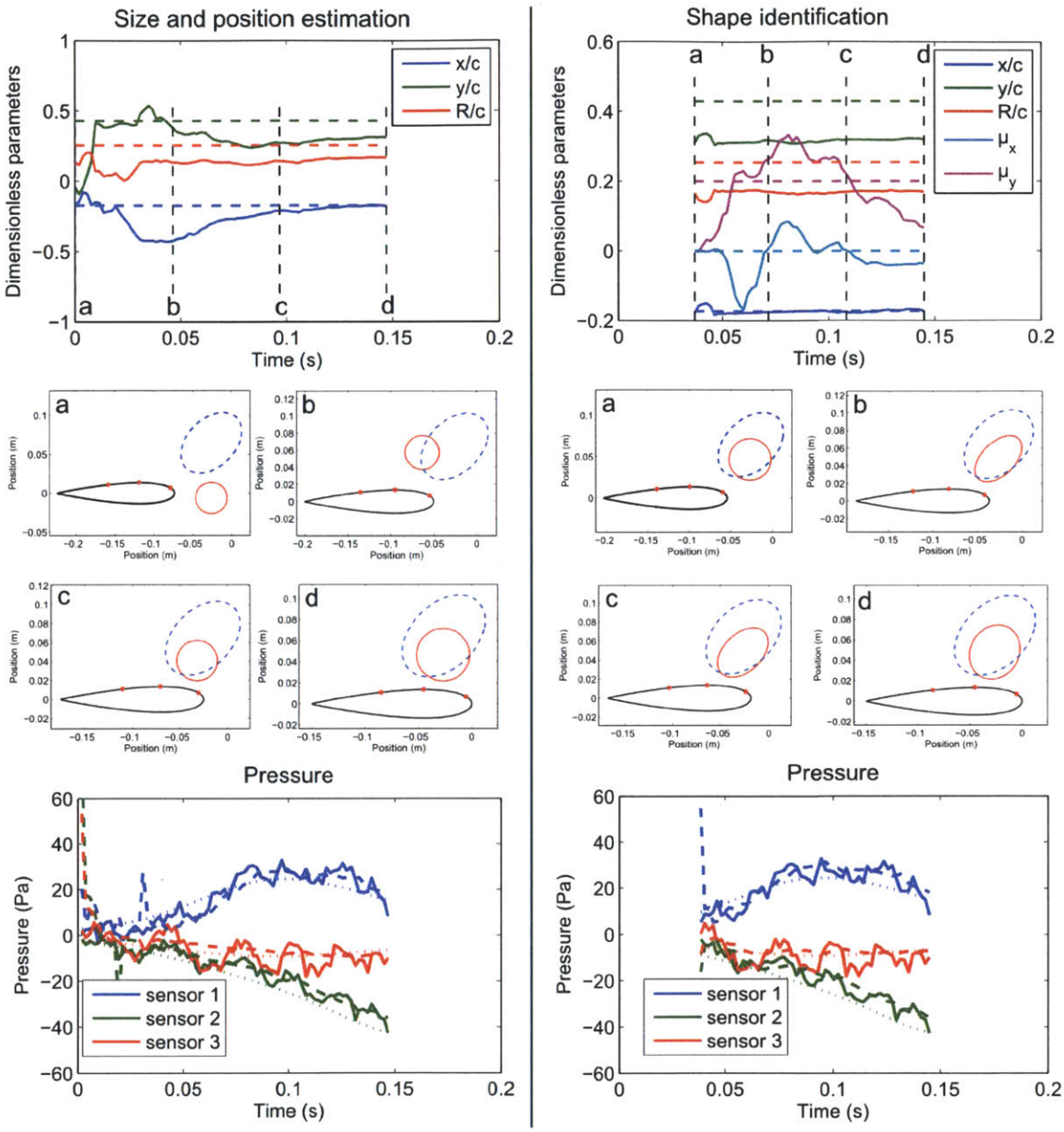

Figure D-5: Object identification, Run 5

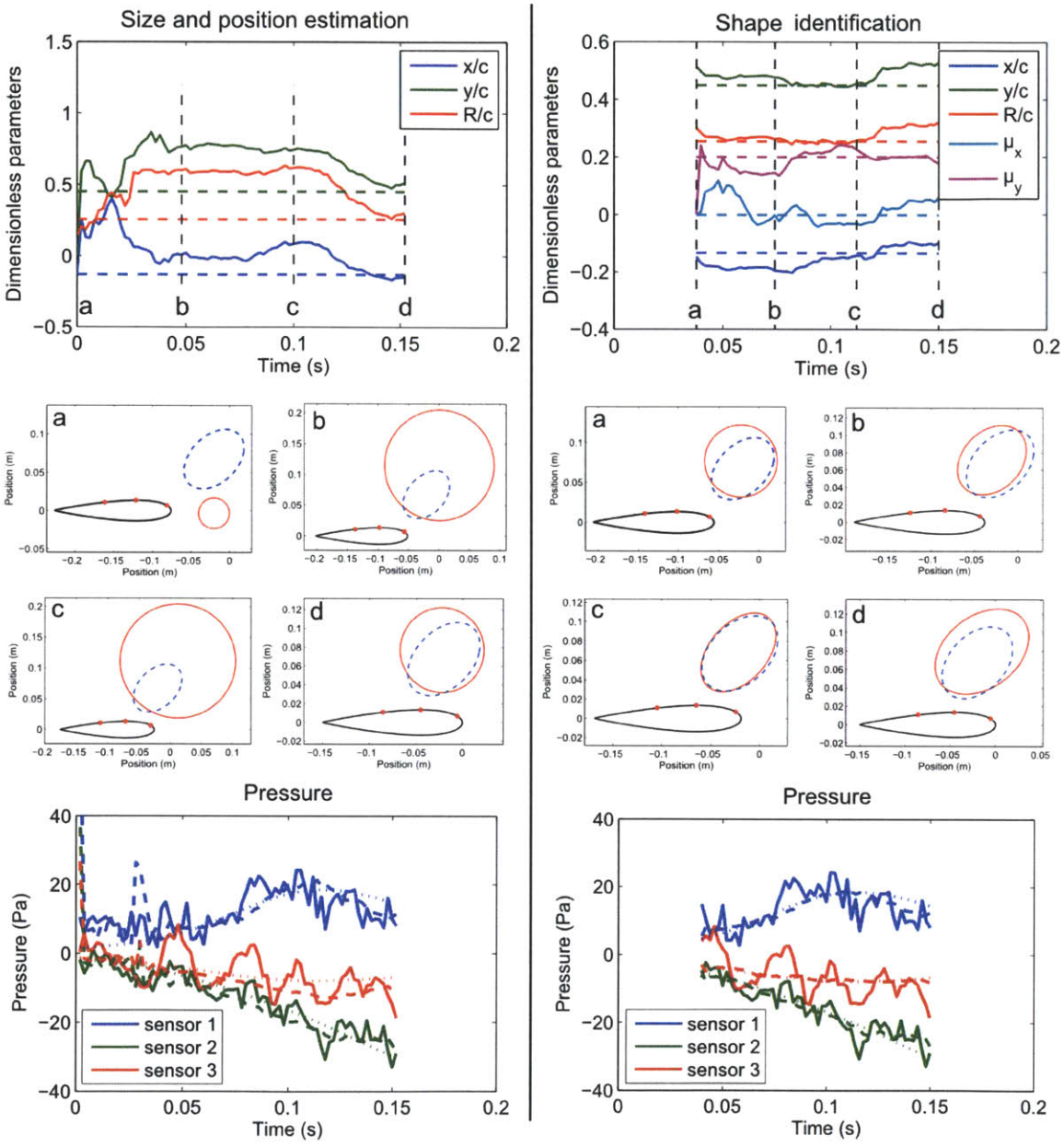

Figure D-6: Object identification, Run 6

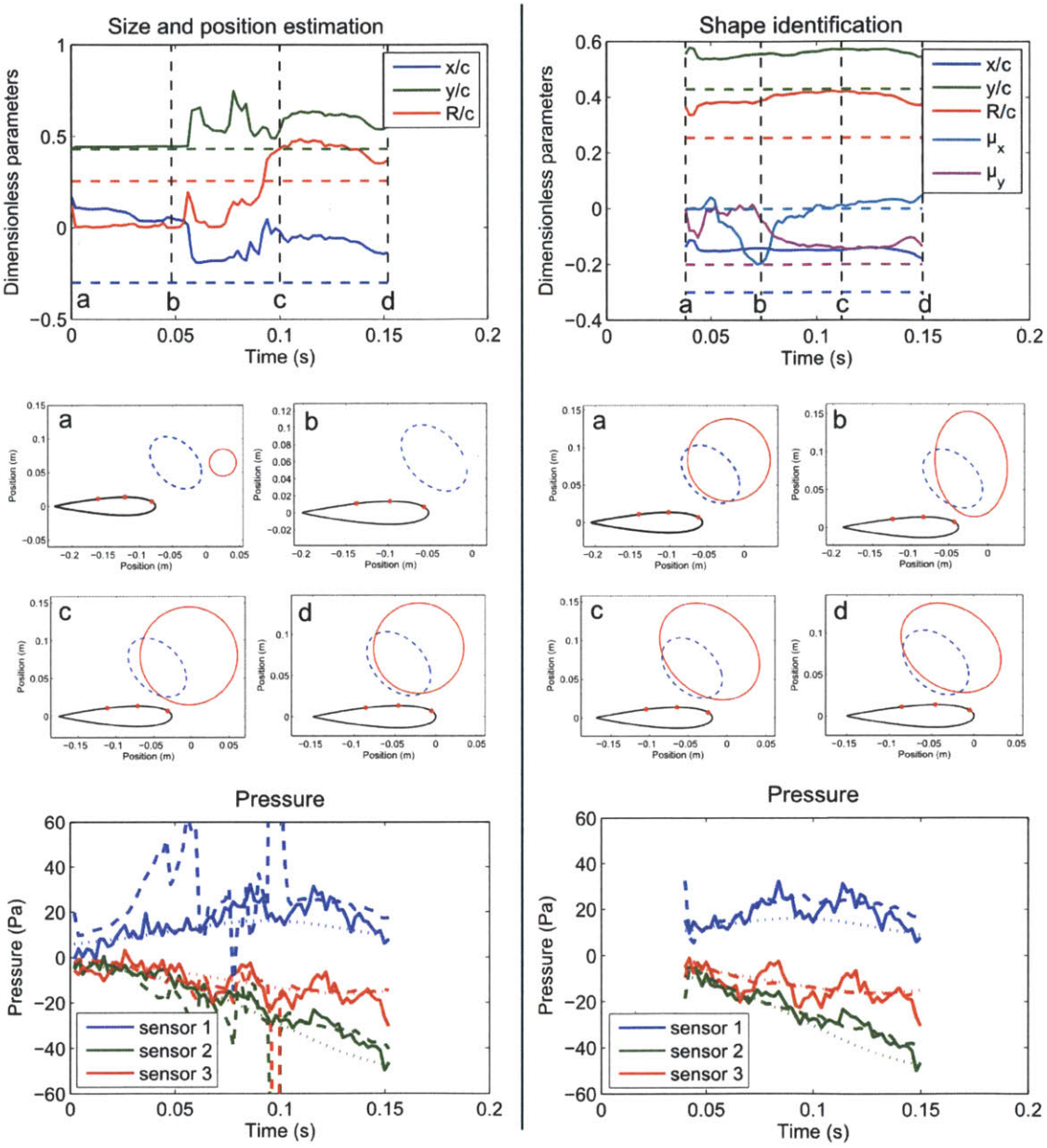

Figure D-7: Object identification, Run 7

Bibliography

[1] C. Barbier and J. A. Humphrey. Drag force acting on a neuromast in the fish lateral line trunk canal. i. numerical modelling of external–internal flow coupling. *Journal of The Royal Society Interface*, 6(36):627–640, 2009.

[2] R. Bouffanais, G. D. Weymouth, and D. K. P. Yue. Hydrodynamic object recognition using pressure sensing. *Proceedings of the Royal Society A: Mathematical, Physical and Engineering Sciences*, 467(2125):19–38, 2010.

[3] B. P. Chagnaud, H. Bleckmann, and M. H. Hofmann. Kármán vortex street detection by the lateral line. *Journal of Comparative Physiology A: Sensory, Neural, and Behavioral Physiology*, 193(7):753–763, 2007.

[4] J. Chen, J. Engel, N. Chen, S. Pandya, S. Coombs, and C. Liu. Artificial lateral line and hydrodynamic object tracking. In *Micro Electro Mechanical Systems, 2006. MEMS 2006 Istanbul. 19th IEEE International Conference on*, pages 694–697, 2006.

[5] S. Coombs and C. B. Braun. Information processing by the lateral line system. In S. P. Collin and N.J. Marshall, editors, *Sensory Processing in Aquatic Environments*, pages 122–138. Springer, New York, 1st edition, 2003.

[6] S. Coombs, C. B. Braun, and B. Donovan. The orienting response of lake michigan mottled sculpin is mediated by canal neuromasts. *Journal of Experimental Biology*, 204(2):337–348, 2001.

[7] S. Coombs, M. Hastings, and J. Finneran. Modeling and measuring lateral line excitation patterns to changing dipole source locations. *Journal of Comparative Physiology A*, 178(3), 1996.

[8] S. Coombs and J. C. Montgomery. The enigmatic lateral line system. In Richard R Fay and Arthur N Popper, editors, *Comparative hearing: fish and amphibians*, Springer Handbook of Auditory Research, pages 319–362. Springer, New York, 1999.

[9] T. Burt de Perera. Spatial parameters encoded in the spatial map of the blind mexican cave fish, astyanax fasciatus. *Animal Behaviour*, 68(2):291–295, 2004.

[10] E. J. Denton and J. Gray. Mechanical factors in the excitation of clupeid lateral lines. *Proceedings of the Royal Society of London. Series B, Biological Sciences*, 218(1210):1–26, 1983.

[11] J. Engelmann, W. Hanke, and H. Bleckmann. Lateral line reception in still- and running water. *Journal of Comparative Physiology A: Sensory, Neural, and Behavioral Physiology*, 188(7):513–526, 2002.

[12] Z. Fan, J. Chen, J. Zou, D. Bullen, C. Liu, and F. Delcomyn. Design and fabrication of artificial lateral line flow sensors. *Journal of Micromechanics and Microengineering*, 12(5):655–661, 2002.

[13] J. M. Franosch, H. Hagedorn, J. Goulet, J. Engelmann, and J. L. van Hemmen. Wake tracking and the detection of vortex rings by the canal lateral line of fish. *Physical Review Letters*, 103(7), 2009.

[14] J. Geer. Uniform asymptotic solutions for potential flow about a slender body of revolution. *Journal of Fluid Mechanics*, 67(04):817–827, 1975.

[15] J. Goulet, J. Engelmann, B. P. Chagnaud, J. M. Franosch, M. D. Suttner, and J. L. van Hemmen. Object localization through the lateral line system of fish: theory and experiment. *Journal of Comparative Physiology A: Sensory, Neural, and Behavioral Physiology*, 194(1):1–17, 2007.

[16] E. S. Hassan. Mathematical analysis of the stimulus for the lateral line organ. *Biological Cybernetics*, 52(1):23–36, 1985.

[17] El-S. Hassan. Hydrodynamic imaging of the surroundings by the lateral line of the blind cave fish anoptichthys jordani. In S. Coombs, P. Görner, and Heinrich Münz, editors, *The Mechanosensory lateral line: neurobiology and evolution*, pages 217–227. Springer-Verlag, New York, 1989.

[18] El-S. Hassan. Mathematical description of the stimuli to the lateral line system of fish derived from a three-dimensional flow field analysis. I. the cases of moving in open water and of gliding towards a plane surface. *Biological Cybernetics*, 66(5):443–452, 1992.

[19] El-S. Hassan. Mathematical description of the stimuli to the lateral line system of fish derived from a three-dimensional flow field analysis. II. the case of gliding alongside or above a plane surface. *Biological Cybernetics*, 66(5):453–461, 1992.

[20] J. Hess. Calculation of potential flow about arbitrary bodies. *Progress in Aerospace Sciences*, 8:1–138, 1967.

[21] J. Janssen. Use of the lateral line and tactile senses in feeding in four antarctic nototheniid fishes. *Environmental Biology of Fishes*, 47(1):51–64, 1996.

[22] S. J Julier. The scaled unscented transformation. In *American Control Conference, 2002. Proceedings of the 2002*, volume 6, page 4555–4559, 2002.

[23] S. J. Julier and J. K. Uhlmann. Unscented filtering and nonlinear estimation. *Proceedings of the IEEE*, 92(3):401–422, 2004.

[24] Simon J Julier and Jeffrey K Uhlmann. A new extension of the kalman filter to nonlinear systems. In *AeroSense: 11th Int. Symp. Aerospace/Defense Sensing, Simulation and Controls*, volume 3068, pages 182—193, 1997.

[25] Horace Lamb. *Hydrodynamics.* Dover Pubns, 6th edition, 1993.

[26] M. E. McConney, N. Chen, D. Lu, H. A. Hu, S. Coombs, C. Liu, and V. V. Tsukruk. Biologically inspired design of hydrogel-capped hair sensors for enhanced underwater flow detection. *Soft Matter*, 5(2):292, 2009.

[27] J. C. Montgomery, C. F. Baker, and A. G. Carton. The lateral line can mediate rheotaxis in fish. *Nature*, 389(6654):960–963, 1997.

[28] J. C. Montgomery, S. Coombs, and C. F. Baker. The mechanosensory lateral line system of the hypogean form of astyanax fasciatus. *Environmental Biology of Fishes*, 62(1):87–96, 2001.

[29] M. A. Rapo, H. Jiang, M. A. Grosenbaugh, and S. Coombs. Using computational fluid dynamics to calculate the stimulus to the lateral line of a fish in still water. *Journal of Experimental Biology*, 212(10):1494–1505, 2009.

[30] W. J Richardson. *Marine Mammals and Noise.* Academic Press, 1998.

[31] A. B. Sichert, R. Bamler, and J. L. van Hemmen. Hydrodynamic object recognition: When multipoles count. *Physical Review Letters*, 102(5), 2009.

[32] A. B. Sichert and J. L. van Hemmen. How stimulus shape affects lateral-line perception: analytical approach to analyze natural stimuli characteristics. *Biological Cybernetics*, 102(3):177–180, 2010.

[33] C. von Campenhausen, I. Riess, and R. Weissert. Detection of stationary objects by the blind cave FishAnoptichthys jordani (Characidae). *Journal of Comparative Physiology A: Sensory, Neural, and Behavioral Physiology*, 143(3):369–374, 1981.

[34] J. F. Webb. Mechanosensory lateral line: Functional morphology and neuroanatomy. In Gary Kent Ostrander, editor, *The Laboratory Fish.* Academic Press, San Diego, 2000.

[35] S. P. Windsor and M. J. McHenry. The influence of viscous hydrodynamics on the fish lateral-line system. *Integrative and Comparative Biology*, 2009.

[36] S. P. Windsor, D. Tan, and J. C. Montgomery. Swimming kinematics and hydrodynamic imaging in the blind mexican cave fish (Astyanax fasciatus). *Journal of Experimental Biology*, 211(18):2950–2959, 2008.

[37] Shane P. Windsor, Stuart E. Norris, Stuart M. Cameron, Gordon D. Mallinson, and John C. Montgomery. The flow fields involved in hydrodynamic imaging by blind mexican cave fish (Astyanax fasciatus). part II: gliding parallel to a wall. *J Exp Biol*, 213(22):3832–3842, 2010.

[38] Y. Yang, J. Chen, J. Engel, S. Pandya, N. Chen, C. Tucker, S. Coombs, D. L. Jones, and C. Liu. Distant touch hydrodynamic imaging with an artificial lateral line. *Proceedings of the National Academy of Sciences*, 103(50):18891–18895, 2006.

[39] Y. Yang, N. Nguyen, N. Chen, M. Lockwood, C. Tucker, H. Hu, H. Bleckmann, C. Liu, and D. L Jones. Artificial lateral line with biomimetic neuromasts to emulate fish sensing. *Bioinspiration & Biomimetics*, 5(1):016001, 2010.